

AN ENHANCED VERTICAL GROUND HEAT EXCHANGER MODEL FOR
WHOLE BUILDING ENERGY SIMULATION

By

MATT SANDY MITCHELL

Bachelor of Science in Mechanical Engineering
Brigham Young University—Idaho
Rexburg, ID
2010

Master of Science in Mechanical Engineering
Oklahoma State University
Stillwater, OK
2014

Submitted to the Faculty of the
Graduate College of
Oklahoma State University
in partial fulfillment of
the requirements for
the Degree of
DOCTOR OF PHILOSOPHY
July, 2019

AN ENHANCED VERTICAL GROUND HEAT EXCHANGER MODEL FOR
WHOLE BUILDING ENERGY SIMULATION

Dissertation Approved:

Dr. Jeffrey D. Spitler

Dissertation Adviser

Dr. Christian K. Bach

Dr. Richard A. Beier

Dr. Daniel E. Fisher

Dr. Signhild E. A. Gehlin

Dr. Alan V. Noell

ACKNOWLEDGMENTS

Many people have contributed to this work in some way. Either by providing professional advice and guidance, or through personal encouragement and support. And I consider myself fortunate to have so many good people in my life. It is truly more than I deserve.

First and foremost, my dear wife, Shelley, who has been with me through it all. Through the ups and downs she has encouraged and empathized, laughed and cried, assisted and supported. I am blessed and so thankful so share this life with her. This work is as much yours as it mine.

My children, Lily, Levi and Max, who bring me joy each day. Your bright smiles give me hope for a better tomorrow, and I am so grateful to have you in my life.

My parents, Sandy and Linda Mitchell, who gave me such a good start in this life. I owe so much of what I have to the experiences and skills you gave me.

My adviser, Dr. Jeffrey Spitler, who has guided and instructed me during this project. Your guidance and advice in work and life have been invaluable, and I am lucky to consider you as a colleague and friend.

My informal adviser, Dr. Daniel Fisher, who has been a source of support and guidance. You have guided and buoyed me up during hard times, and you will be an everlasting example to me.

My labmates and friends at OSU, who are nearly too numerous to mention. The exception is Dr. Edwin Lee, who has supported and advised me during my work and

Acknowledgments reflect the views of the author and are not endorsed by committee members or Oklahoma State University.

has become a close personal friend. Your advice and friendship has given me more than I could ever repay.

My committee members: Dr. Christian Bach, Dr. Richard Beier, Dr. Daniel Fisher, Dr. Signhild Gehlin, and Dr. Alan Noell, who have selflessly sacrificed your time and efforts to provide thoughtful advice during this work.

Acknowledgments reflect the views of the author and are not endorsed by committee members or Oklahoma State University.

Name: MATT SANDY MITCHELL

Date of Degree: JULY, 2019

Title of Study: AN ENHANCED VERTICAL GROUND HEAT EXCHANGER
MODEL FOR WHOLE BUILDING ENERGY SIMULATION

Major Field: MECHANICAL ENGINEERING

Abstract: The U.S. Energy Information Agency estimates that buildings consume more than 40% of all energy used in the United States. This includes considering energy used for transportation and heavy industry. As a result, many people across the world have invested significant time and resources developing tools for predicting building performance so energy usage and costs can be optimized. One of these tools are whole building energy simulation (WBES) programs which model building geometry, building construction, and usage to estimate performance. WBES are used by 10's of thousands of architects, designers, and engineers throughout the world each day. Yet, despite this, WBES models for ground heat exchangers (GHE) suffer from a number of limitations. Often, these models rely on third-party tools to generate required data needed for simulation. They also are limited in the ability to model a significant number of common GHE configurations. This limits the abilities of designers to specify and accurately compare ground source heat pump systems to other common building conditioning systems.

This study focuses on developing GHE models for use in WBES, which adds an important emphasis to minimize simulation time. In addition, the study seeks to eliminate the need for external tools to improve the accuracy of the simulation methods. This is done in three distinct parts.

Load aggregation methods are characterized, a large parametric study is performed, and the results are summarized. The work performed makes recommendations for optimal load aggregation methods and parameters to minimize simulation time and maximize simulation accuracy.

An enhanced ground heat exchanger model is developed and validated. The enhanced model allows users to simulate GHE at short and long simulation time steps. The model is validated against experimental data from a multi-flow rate thermal response test. A simplified dynamic borehole heat exchanger model is also developed and validated.

A method for simulating the interference between thermally interacting GHE is developed and validated. A case study is presented demonstrating the method usage.

TABLE OF CONTENTS

| Chapter | Page |
|---|---------------|
| I INTRODUCTION | 1 |
| 1.1 Overview | 1 |
| 1.2 GHE Modeling Background | 5 |
| 1.2.1 Analytical Models | 5 |
| 1.2.1.1 Infinite Line Source | 6 |
| 1.2.1.2 Infinite Cylinder Source | 8 |
| 1.2.2 Response Factor Models | 10 |
| 1.2.3 Thermal Resistance-Capacity Models | 16 |
| 1.2.4 Numerical Models | 21 |
| 1.2.5 Borehole Thermal Resistance Models | 22 |
| 1.2.6 Load Aggregation Methods | 25 |
| 1.2.7 Response Factor Generation Models | 28 |
| 1.2.7.1 Superposition Borehole Model | 28 |
| 1.2.7.2 Line- and Cylinder-Source Models | 29 |
| 1.2.7.3 Finite Line-Source Models | 30 |
| 1.2.7.4 Numerical Methods | 32 |
| 1.2.7.5 Other Methods for Response Factor Generation . . | 33 |
| 1.3 Discussion | 34 |
| 1.3.1 Simulation Time | 35 |
| 1.3.2 Non-uniform GHE Array Arrangements | 38 |
| 1.3.3 Non-uniform GHE Depths | 39 |
| 1.3.4 Non-Uniform GHE Inlet Conditions | 39 |
| 1.3.5 Non-Uniform GHE Boundary Conditions | 41 |
| 1.3.6 Modifying an Existing GHE System | 42 |
| 1.3.7 Small Simulation Time Steps | 44 |
| 1.4 Objectives | 45 |
| 1.5 Outline | 45 |
| II CHARACTERIZATION, TESTING AND OPTIMIZATION OF LOAD AGGREGATION METHODS FOR GROUND HEAT EX- CHANGER RESPONSE-FACTOR MODELS | 47 |
| 2.1 Introduction | 48 |
| 2.2 Literature Review | 53 |
| 2.2.1 Static Methods | 53 |
| 2.2.2 Dynamic Method | 59 |
| 2.2.3 Other Methods | 64 |

| | | |
|-------|--|----|
| 2.3 | Methodology | 64 |
| 2.3.1 | Static Method | 67 |
| 2.3.2 | Dynamic Method | 67 |
| 2.4 | Results | 70 |
| 2.4.1 | General Parametric Study Results Analysis | 70 |
| 2.4.2 | Detailed Dynamic Parametric Study Analysis | 72 |
| 2.4.3 | Final Configuration Selection | 79 |
| 2.5 | Conclusions and Recommendations | 85 |

III AN ENHANCED VERTICAL GROUND HEAT EXCHANGER MODEL FOR WHOLE BUILDING ENERGY SIMULATION . 87

| | | |
|---------|--|-----|
| 3.1 | Introduction | 87 |
| 3.2 | Literature Review | 89 |
| 3.3 | Methodology | 89 |
| 3.3.1 | Enhanced Response Factor Model | 89 |
| 3.3.2 | Model Reformulation for WBES Usage | 95 |
| 3.3.3 | Dynamic Borehole Model | 98 |
| 3.3.3.1 | Simple Borehole TRCM | 98 |
| 3.3.3.2 | Dynamic Pipe Model | 101 |
| 3.3.3.3 | Dynamic Borehole Model Validation | 104 |
| 3.3.4 | Exiting-Fluid-Temperature Response Factor Generation | 111 |
| 3.3.5 | Borehole-Wall-Temperature Response Factor Generation | 118 |
| 3.4 | Validation | 120 |
| 3.4.1 | High-flow MFRTRT | 120 |
| 3.4.2 | Low-Flow MFRTRT | 127 |
| 3.5 | Conclusions and Recommendations | 128 |

IV CROSS-g-FUNCTION RESPONSE FACTORS FOR THE SIMULATION OF INTERFERENCE BETWEEN GROUND HEAT EXCHANGERS . 130

| | | |
|-------|---|-----|
| 4.1 | Introduction | 130 |
| 4.2 | Definition | 132 |
| 4.3 | Methodology for Calculating Cross-g-functions | 134 |
| 4.4 | Validation | 137 |
| 4.5 | Application Methods | 144 |
| 4.5.1 | Borehole | 145 |
| 4.5.2 | Building Loads | 146 |
| 4.5.3 | Heat Pump Model | 146 |
| 4.5.4 | Pumping | 149 |
| 4.5.5 | Ground Heat Exchanger Model | 150 |
| 4.6 | Case Study | 150 |
| 4.7 | Conclusions and Recommendations | 159 |

| | | |
|----------|---|------------|
| V | CONCLUSIONS | 161 |
| 5.1 | Summary | 161 |
| 5.2 | Conclusions | 162 |
| 5.3 | Future Work | 163 |
| 5.3.1 | Load Aggregation | 163 |
| 5.3.2 | Enhanced GHE Model | 164 |
| 5.3.3 | Cross-g-functions | 164 |
| | REFERENCES | 165 |
| | APPENDIX A HISTORICAL RESPONSE FACTOR MODEL | 182 |
| 1.1 | Derivation | 182 |
| 1.2 | Extension of Historical Model for Improved Mean Fluid Temperature | 184 |

LIST OF TABLES

| Table | | Page |
|-------|--|------|
| 1.1 | Data from EnergyPlus example simulations | 36 |
| 2.1 | Idealized aggregation example. | 50 |
| 2.2 | Static method aggregation example | 54 |
| 2.3 | Yavuzturk and Spitler (1999) method parameters | 56 |
| 2.4 | Liu (2005) method simulation case descriptions | 57 |
| 2.5 | Bernier et al. (2004) original aggregation parameters | 57 |
| 2.6 | Bernier et al. (2004) minimum number of bins, $N_{b,i}$ | 58 |
| 2.7 | Bernier et al. (2004) bin durations (hr) | 58 |
| 2.8 | Dynamic aggregation example | 61 |
| 2.9 | Dynamic method as proposed by Claesson and Javed (2012) | 63 |
| 2.10 | Static method parametric study simulation case durations, in hours | 68 |
| 2.11 | Static method parametric study minimum number of bins | 69 |
| 2.12 | Balanced load cases RMSE [$^{\circ}\text{C}$] $\times 10^3$ statistics | 71 |
| 2.13 | Balanced load cases simulation time fraction $\times 10^3$ statistics | 71 |
| 2.14 | Imbalanced load cases RMSE [$^{\circ}\text{C}$] $\times 10^3$ statistics | 71 |
| 2.15 | Balanced load, 1-year Pareto data | 74 |
| 2.16 | Balanced load, 5-year Pareto data | 74 |
| 2.17 | Balanced load, 10-year Pareto data | 75 |
| 2.18 | Imbalanced load, 1-year Pareto data | 75 |
| 2.19 | Imbalanced load, 5-year Pareto data | 76 |
| 2.20 | Imbalanced load, 10-year Pareto data | 76 |

| | | |
|------|--|-----|
| 2.21 | Heat pump performance data | 79 |
| 2.22 | Pareto data for dynamic configurations with RMSE less than 0.1°C | 81 |
| 2.23 | 10×10 GHE and single BH RMSE [$^{\circ}\text{C}$] results | 83 |
| 2.24 | 10×10 GHE and single BH MBE [$^{\circ}\text{C}$] results | 83 |
| 3.1 | Dynamic borehole model Pareto data | 107 |
| 3.2 | Data from g_b calculations taken at $t = 24$ h | 116 |
| 3.3 | RMSE/MBE for High-Flow MFRTRT | 124 |
| 3.4 | RMSE/MBE for Low-Flow MFRTRT | 128 |
| 4.1 | Calculations for the effect of GHE E on GHE D | 143 |
| 4.2 | Calculations for the effect of GHE D on GHE E | 144 |
| 4.3 | Borehole configuration parameters | 145 |
| 4.4 | Capacity and COP heat pump polynomial coefficients | 149 |

LIST OF FIGURES

| Figure | Page |
|--|------|
| 1.1 Common energy-related phrase usage frequencies | 2 |
| 1.2 Heat pulse steps | 11 |
| 1.3 Temperature response to heat pulses | 11 |
| 1.4 Example g-functions for a 3×2 rectangular GHE array | 13 |
| 1.5 Non-physical results from EnergyPlus response factor model | 14 |
| 1.6 g-functions example for single borehole | 15 |
| 1.7 RC-network geometrical representation. | 17 |
| 1.8 Finite line source geometrical representation | 31 |
| 1.9 Example EnergyPlus simulation times for different building types . . . | 36 |
| 2.1 Load Profiles | 66 |
| 2.2 Balanced load, 10-year parametric simulation results | 70 |
| 2.3 Balanced load, 10-year dynamic method simulation cases with Pareto front | 73 |
| 2.4 Dynamic method balanced load, 10-year cases colored by expansion rate | 77 |
| 2.5 Dynamic method balanced load, 10-year cases with selected expansion rates and results colored by the number of bins in the first level. . . . | 78 |
| 2.6 Mean STF and RMSE for dynamic configurations with RMSE less than 0.1°C | 81 |
| 2.7 Extended duration loading-unloading test results | 84 |
| 3.1 Single U-tube borehole. | 91 |
| 3.2 Dynamic model borehole schematic | 98 |

| | | |
|------|--|-----|
| 3.3 | Simple TRCM | 99 |
| 3.4 | Dynamic pipe model response for $Re \approx 5000$ | 103 |
| 3.5 | Dynamic pipe model response for $Re \approx 50,000$ | 103 |
| 3.6 | Grout fraction effects on dynamic borehole model | 105 |
| 3.7 | Iteration count effects on dynamic borehole model | 106 |
| 3.8 | Segment count effects on dynamic borehole model | 106 |
| 3.9 | Time step effects on dynamic borehole model | 107 |
| 3.10 | Pareto values for variations in dynamic borehole model input parameters | 108 |
| 3.11 | Dynamic borehole model compared to first 2 hours of high-flow MFRTRT | 109 |
| 3.12 | Dynamic borehole model compared to high-flow MFRTRT | 109 |
| 3.13 | Dynamic borehole model compared to first 2 hours of low-flow MFRTRT | 110 |
| 3.14 | Dynamic borehole model compared to 3 days of low-flow MFRTRT | 111 |
| 3.15 | R_b vs. time for a constant flow rate, variable heat input rate | 113 |
| 3.16 | R_b vs. time for a constant heat rate, variable circulating fluid flow rate | 113 |
| 3.17 | Dynamic borehole model temperature response for 2 hours | 114 |
| 3.18 | Dynamic borehole model temperature response for 24 hours | 115 |
| 3.19 | g_b vs. $\ln(t/t_s)$ | 115 |
| 3.20 | g_b vs. flow rate with points colored by R_b , taken at $t = 24$ h | 117 |
| 3.21 | q_f vs. q_b for data used to generate g_b data | 118 |
| 3.22 | g vs. $\ln(t/t_s)$ | 119 |
| 3.23 | Short time step g-functions vs. $\ln(t/t_s)$ for various flow rates | 120 |
| 3.24 | Enhanced model results for high-flow MFRTRT. First 2 hours. 60 s time step. | 121 |
| 3.25 | Enhanced model results for high-flow MFRTRT. First flow rate change. 60 s time step. | 122 |
| 3.26 | Enhanced model results for high-flow MFRTRT. Fourth flow rate change. 60 s time step. | 123 |

| | | |
|------|---|-----|
| 3.27 | Enhanced model results for high-flow MFRTRT. Full data set. 60 s time step. | 124 |
| 3.28 | Enhanced model results for high-flow MFRTRT. Full data set. 1 hr time step. | 125 |
| 3.29 | Enhanced model heat transfer results for high-flow MFRTRT. Full data set. 60 s time step. | 126 |
| 3.30 | Enhanced model heat transfer results for high-flow MFRTRT. Full data set. 1 hr time step. | 126 |
| 3.31 | Enhanced model temperature results for low-flow MFRTRT. Full data set. 1 hr time step. | 127 |
| 3.32 | Enhanced model heat transfer results for low-flow MFRTRT. Full data set. 1 hr time step. | 128 |
| 4.1 | Fields, A , B , and C used for validation purposes | 139 |
| 4.2 | GHE A and B self- and cross-g-functions validated against the pyg-function library. | 139 |
| 4.3 | Self- and cross-g-functions for GHE A and B , and self-g-functions for GHE C | 140 |
| 4.4 | Single borehole GHE D and 2×2 L-shaped borehole GHE E | 141 |
| 4.5 | GHE D self- and cross-g-functions | 142 |
| 4.6 | GHE E self- and cross-g-functions | 143 |
| 4.7 | Space heating load profile and outdoor air temperature | 146 |
| 4.8 | Domestic hot water loads | 147 |
| 4.9 | Heat pump schematic, recreated after Gehlin and Spitler (2014b) | 148 |
| 4.10 | Neighborhood arrangement | 150 |
| 4.11 | g-function values | 152 |
| 4.12 | Temperatures and loads from February 1–2, year 1 | 153 |

| | | |
|------|---|-----|
| 4.13 | Temperatures and loads from July 1–2, year 1 | 153 |
| 4.14 | Hourly, monthly, and annual self-system heat pump inlet temperature | 154 |
| 4.15 | Annual self-system heat pump inlet temperature with cross-system effects | 154 |
| 4.16 | Annual average COP. Includes electric resistance heating. | 156 |
| 4.17 | Annual heat pump energy usage | 156 |
| 4.18 | Annual heat pump energy extracted from the soil | 157 |
| 4.19 | Annual resistance heating energy usage | 158 |
| 4.20 | Annual heat pump and immersion heater electrical energy usage . . . | 158 |
| 4.21 | Annual heat pump and immersion heater electrical energy usage for cross-system effects starting at 5 years | 159 |

ABBREVIATIONS

| | |
|---------|---|
| BH | Borehole |
| BTES | Borehole Thermal Energy System |
| COP | Coefficient of Performance |
| EFT | Entering Fluid Temperature |
| ExFT | Exiting Fluid Temperature |
| FFT | Fast Fourier Transform |
| FLS | Finite Line Source |
| GB | Gigabyte |
| GHE | Ground Heat Exchanger |
| GSHP | Ground Source Heat Pump |
| HDPE | High Density Polyethylene |
| HP | Heat Pump |
| HVAC | Heating, Ventilating and Air-conditioning |
| ICS | Infinite Cylinder Source |
| ILS | Infinite Line Source |
| MBE | Mean Bias Error |
| MFRTTRT | Multi-Flow Rate Thermal Response Test |
| MFT | Mean Fluid Temperature |
| MLAA | Multi-load Aggregation Algorithm |
| NSGA | Non-dominated Sorting Genetic Algorithm |
| RC | Resistance-Capacitance |
| RMSE | Root-Mean Squared Error |

| | |
|--------|--------------------------------------|
| SBM | Superposition Borehole Model |
| STS | Short Time Step |
| TMY | Typical Meteorological Year |
| TRCM | Thermal Resistance-Capacitance Model |
| TRNSYS | Transient System Simulation Tool |
| TRT | Thermal Response Test |
| UGT | Undisturbed Ground Temperature |
| WBES | Whole Building Energy Simulation |

NOMENCLATURE

| VARIABLES | UNITS | DESCRIPTION |
|-----------------|----------------------|---|
| B | m | Borehole-to-Borehole Spacing |
| c | - | Constant |
| c_p | J/(kg K) | Specific Heat |
| C | J/(m ³ K) | Heat Capacity |
| d | m | Diameter |
| D | m | Borehole Depth Below Ground Surface |
| e | J/m | Normalized Energy |
| \dot{e}_{gen} | W/m ³ | Internal Energy Generation |
| E | J | Energy |
| E_1 | - | Exponential Integral |
| f | - | Fraction |
| Fo | - | Fourier Number |
| g | - | g-function, Borehole Wall Temperature |
| g_b | - | g-function, Exiting Fluid Temperature |
| G | - | Analytical Cylinder Source Solution |
| h | - | Time Step |
| H | m | Borehole Length |
| i | - | Arbitrary Index |
| j | - | Arbitrary Index |
| J_0 | - | Bessel Function of the First Kind, Zeroth Order |
| J_1 | - | Bessel Function of the First Kind, First Order |

| | | |
|-----------|----------------|--|
| k | W/(m K) | Thermal Conductivity |
| L | m | Length |
| \dot{m} | kg/s | Mass Flow Rate |
| n | - | Counter |
| N_b | - | Number of Aggregation Bins |
| Nu | - | Nusselt Number |
| q | W/m | Normalized Heat Transfer Rate |
| Q | W | Heat Transfer Rate |
| r | m | Radius |
| r_e | - | Expansion Rate |
| R | K/(W/m) | Thermal Resistance |
| s | m | Shank-spacing |
| t | s | Time |
| t_b | s | Aggregated Bin Time Duration |
| t_s | s | Characteristic Time |
| T | °C | Temperature |
| T_b | °C | Temperature, Borehole Wall |
| T_f | °C | Temperature, Mean Fluid Averaged Over Bore- hole Length |
| $T_{f,l}$ | °C | Temperature, Mean Fluid, Local |
| T_{in} | °C | Temperature, Inlet |
| T_{out} | °C | Temperature, Outlet |
| T_0 | °C | Temperature, Initial |
| u | - | Point Location |
| V | m ³ | Volume |
| x | - | Arbitrary Variable |
| \hat{y} | - | Predicted Value |

| | | |
|-------|---|--|
| y | - | Observed Value |
| Y_0 | - | Bessel Function of the Second Kind, Zeroth Order |
| Y_1 | - | Bessel Function of the Second Kind, First Order |
| z | m | Height |

| GREEK SYMBOLS | UNITS | DESCRIPTION |
|---------------|-------|-------------|
|---------------|-------|-------------|

| | | |
|----------|-------------------|---------------------------------------|
| α | m ² /s | Thermal Diffusivity |
| γ | - | Euler-Mascheroni Constant - 0.5772... |
| ϕ | - | Angular Direction |
| ρ | kg/m ³ | Density |

SUPERSCRIPTS

| | |
|--------|-----------------|
| $()^*$ | Effective Value |
| $()'$ | Mirror Point |

SUBSCRIPTS

| | |
|--------|-----------------|
| a | Internal |
| b | Borehole |
| c | Concrete |
| $cond$ | Conduction |
| $conv$ | Convection |
| f | Fluid |
| g | Grout |
| p | Pipe |
| s | Soil |
| t | Total |
| 12 | Direct-Coupling |

CHAPTER I

INTRODUCTION

1.1 Overview

In today's society, an ever increasing percentage of the general population are concerned with energy generation and usage. This so called "green" movement is spurred on by not only by the community of climate scientists, but has become a symbol of pop culture in the sense that it is not only prudent, but "cool" to source and use energy wisely. This can be seen in from Figure 1.1 where the frequency of some relevant energy-usage related phrases are plotted from 1960 to 2008. All of the phrases, with the exception of fossil fuels consistently trend upward during the period. The data represented in the figure is anecdotal, but helps illustrate the sentiment which exists at the time in which this study is performed regarding energy.

Regardless of the political and social issues surrounding climate change, energy and resource utilization, etc., it should be an undeniable fact that modern society's dependence on fossil fuels—which are inherently finite—should be reason enough for us to seek to minimize energy usage while also accounting for and balancing life-cycle costs.

One such technology is the ground-source heat pump (GSHP) system for building space conditioning. GSHP systems use the solar energy which has been stored in the ground as a means of heating and cooling buildings. When compared to conventional and even the most state of the art heating and cooling systems (Spitler et al., 2017), GSHP technology may be one of the most energy efficient methods for building space

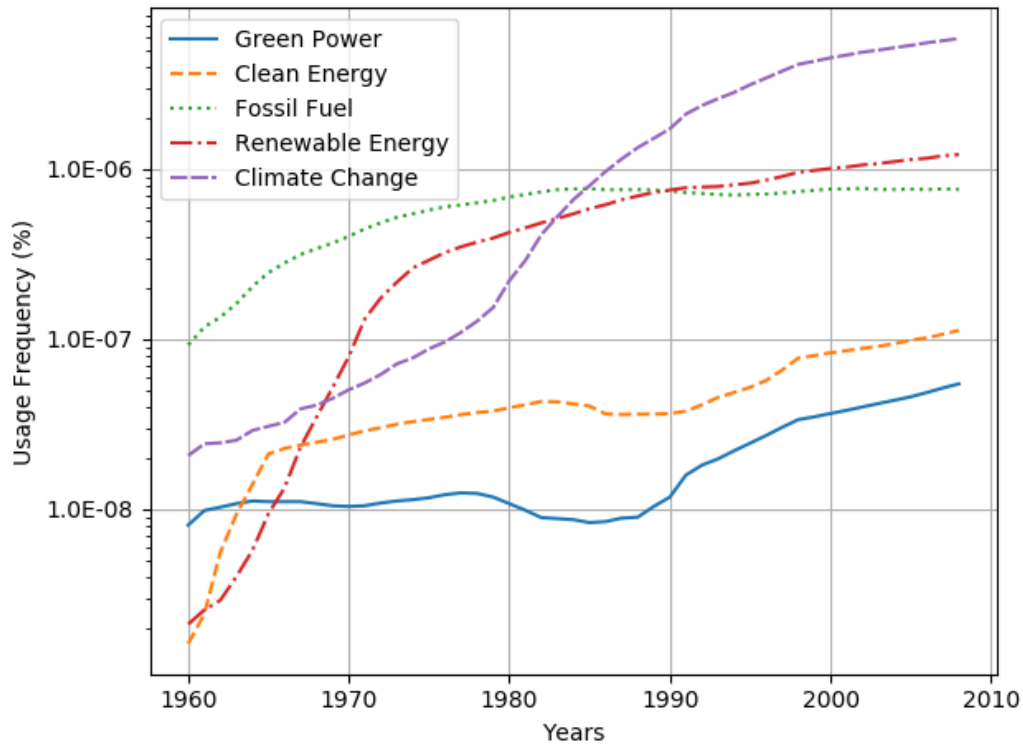


Figure 1.1: Common energy-related phrase usage frequencies (Google, 2018)

conditioning. This is partly due to the stability of the soil temperature when compared to the air temperature; however, from a thermodynamics perspective this is also related to the space conditioning equipment’s coefficient of performance (COP) which favors smaller temperature differences between the high and low side heat reservoirs. This is seen in the limiting case of the Carnot Cycle.

GSHP systems are primarily composed of three pieces of equipment: a heat pump, a ground heat exchanger which exchanges energy with the soil, and a circulation pump to move fluid between heat pump and heat exchanger. The heat pump will allow water (or some other circulation fluid) to circulate on the ground (source) side, and water or air to circulate on the building (load) side. GSHP systems may be either open-loop or closed-loop systems. Open-loop systems are systems which take water from a surface water body (e.g. pond, lake, river), standing column well (Rees et al., 2004), or even from a potable water well, and use that water for direct cooling or on the source

side of a heat pump for heating or cooling (Mitchell and Spitler, 2013). In open-loop systems, once the water has passed through the heat pump it is returned to its source or disposed of in another fashion. Closed-loop systems use a ground heat exchanger (GHE)^{1 2} that is typically constructed from high-density polyethylene (HDPE) pipes which are embedded in the soil. Once constructed, the circulation fluid in GHE will remain in the GHE. Several variations of GHE exist, including: vertical, horizontal, inclined, and slinky. These are briefly described here.

- *Vertical GHE* are installed using a process similar to the method used to install water wells. A rotary or hammer drilling platform which is mounted to a tractor or truck is moved into place at the borehole location. The borehole is then created by drilling down to the GHE design depth. Occasionally, the upper portion of the borehole is cased with pipe to stabilize the surface soil and to help prevent surface water infiltration into the ground water. This is common in water-filled (non-grouted) GHE, but often omitted in grouted GHE. For grouted GHE the U-tube pipe along with a tremie pipe are then forced down the borehole to the bottom. The grout, which fills the space between the borehole wall and the U-tube, is then pumped down the tremie pipe as it is simultaneously retracted until the borehole is filled with grout and the U-tube installed. For non-grouted GHE, the space between the U-tube and borehole wall are allowed to fill with water from the local water table.
- *Horizontal GHE* are typically installed by digging a trench with a backhoe, excavator, trencher, or other heavy equipment. The pipe is then placed in the trench and the trench is backfilled with the original soil. Occasionally, horizontal drilling machines are used to install horizontal GHE in a fashion similar to vertical GHE.

¹a.k.a. boreholes, borehole heat exchanger(s), or borehole arrays

²May also be referred to as “geothermal” heat exchangers, though the term is often used loosely. This is partly due to the fact that it is shared with geothermal power generation technologies which generate electricity from geothermal temperature gradients.

- *Inclined GHE* are a hybrid between horizontal and vertical GHE. At a site where the surface area may be limited but no underground impediments are found, it may be possible to drill GHE at different inclinations and orientations to maximize the average distance between boreholes while maintaining a small surface footprint.
- *Slinky™ GHE* are made from a single tube which has been fabricated into a flat coil with the loops overlapping each other. The GHE are installed in the same way other horizontal GHE are installed.

Though the materials and methods involved in constructing GHE are relatively simple, the physics and mathematics required to model them is often complicated to fully understand and difficult to implement in a practical manner. GHE operate over a large span of spatial and temporal scales. As a result, the models also must account for the effects which occur within each respective scale which adds further complications.

Aside from the “theoretical” problems involved with the physics, mathematics, numerical solution schemes, etc., the “real world” problems also add to the difficulty of the problem. Properties for soil, grout, pipe, circulating fluid, etc., vary continuously with changes in temperature, pressure, water content, etc. GHE are often installed by people who opt for added profitably through time and material savings, rather than seeking to enhancing the physical capabilities of the system, or install it exactly as specified by the designer. As an example, if a problem occurs during installation, (e.g. the lower portion of a borehole collapses before U-tube and grout installation) the installer will likely try to use what can be saved of the existing work and adjust the rest of the design to compensate. As a result, it is not uncommon for borehole field designs to be adjusted in-situ during the installation process to compensate for whatever difficulties arise.

This work primarily focuses on developing improvements to models for vertical

ground heat exchangers which allows them to be simulated in the context of a whole building energy simulation (WBES³). Specifically, the models seek to add functionality that push model capabilities towards physical realities which occur in actuality, and away from the theoretical assumptions which have been treated as acceptable simplifications up until this point. These modeling capability improvements will result in more accurate GHE simulation methods.

1.2 GHE Modeling Background

A number of different GHE modeling methodologies have been developed over the years. As is typical for methods and technologies which evolve with time, these models have evolved from simple, closed-form analytical expressions to methods which are mathematically complex and which simulate specific, nuanced physical behavior. These models will be reviewed and described in this section.

1.2.1 Analytical Models

Analytical models for GHE form the backbone of GHE simulation and validation. Historically, they have been used extensively to model systems containing an individual borehole to complex borehole arrays. Analytical models also serve the purpose of providing an “exact” solution which can be used to validate more complicated models. Li et al. (2016) and Spitler and Bernier (2016) have reviewed a number of these analytical solutions. The most common ones are discussed here.

Historically, GHE modeling has been handled by analyzing the region inside of the borehole separately from the region outside of the borehole. Ignoring for a moment the U-tube, grout, and circulating fluid, the GHE may be thought of as a line or cylinder conducting heat into the ground, which is assumed to be a semi-infinite medium with

³This may also be referred to in the literature as “building energy simulation,” or “building energy modeling,” however, in this context, the author wishes to emphasize that the building envelope, not just the system, is included in the simulation.

uniform temperature and isotropic properties. The generalized transient conduction equation in cylindrical coordinates is given in Equation 1.1.

$$\frac{1}{r} \frac{\partial}{\partial r} \left(kr \frac{\partial T}{\partial r} \right) + \frac{1}{r^2} \frac{\partial}{\partial \phi} \left(k \frac{\partial T}{\partial \phi} \right) + \frac{\partial}{\partial z} \left(k \frac{\partial T}{\partial z} \right) + \dot{e}_{gen} = \rho c_p \frac{\partial T}{\partial t} \quad (1.1)$$

Ignoring axial and angular effects, internal heat generation, and assuming constant properties, we get Equation 1.2.

$$\frac{1}{r} \frac{\partial}{\partial r} \left(r \frac{\partial T}{\partial r} \right) = \frac{1}{\alpha} \frac{\partial T}{\partial t} \quad (1.2)$$

Line and cylinder source models are based on pure conduction solutions of Equation 1.2.

1.2.1.1 Infinite Line Source

The infinite line source (ILS) model is a pure conduction solution for an infinite line which conducts heat continuously at a constant rate beginning from time, $t = 0$. The ground surface is not modeled, therefore the model assumes the ground to be a continuous, infinite medium. The ILS solution is generally credited as being developed by Lord Kelvin (Thomson, 1884). However, Spitler and Gehlin (2015) point out that the method was originally developed based on Fourier's point source solution, and as such, there is some ambiguity regarding who is given credit for the method. After detailed derivation, Carslaw and Jaeger (1959) (Chapter X, Eq. (6)) give a simplified form of the line source solution in Equation 1.3.

$$T = T_0 + \frac{q}{4\pi k_s} \left(\ln \left(\frac{4\alpha_s t}{r^2} \right) - \gamma \right) \quad (1.3)$$

Hellström (1991) states that Equation 1.3 gives a maximum error in the temperature rise of 2% when $t > 5r_b^2/\alpha_s$ which is generally considered to be the lower limit for which this model and subsequent line and cylinder source models are applicable.

For reference, when $\alpha_s = 1 \times 10^{-6} \text{ m/s}^2$ and $r_b = 0.05 \text{ m}$, (which are common values) $t = 12\,000 \text{ s}$, or about 3.3 h.

Some authors (Ingersoll and Plass, 1948; Ingersoll et al., 1951) have suggested applications for the ILS models (e.g. underground buried electrical cables, or horizontal underground piping); however Mogensen (1983) applied several approximations to the method which have since become common in GHE modeling. These approximations are:

- The line source solution is used to evaluate temperatures at the borehole wall, which assumes that the borehole is filled with soil and the line source is at the center of the borehole.
- Heat transfer within the borehole is assumed to be quasi-steady. As a result an effective borehole resistance can be applied between the borehole wall and the fluid in the U-tube.
- The mean fluid temperature is taken to be the simple average of the inlet and outlet, though methods with additional refinements have also been used.

With these assumptions the borehole mean fluid temperature given a constant heat pulse can be calculated using Equation 1.4.

$$T_f = T_s + \frac{q}{4\pi k_s^*} \cdot E_1\left(\frac{r_b^2}{4\alpha_s t}\right) + q \cdot R_b^* \quad (1.4)$$

Gautschi and Cahill (1964) give a series expansion of the exponential integral as is shown in Equation 1.5.

$$E_1(x) = -\gamma - \ln(x) - \sum_{n=1}^{\infty} \frac{(-1)^n x^n}{n \cdot n!} \quad (1.5)$$

Spitler and Gehlin (2015) also give an approximate form of the line source solution (see Equation 1.6) which is commonly applied to thermal response tests (TRT) to estimate ground thermal properties.

$$T_f = T_s + \frac{q}{4\pi k_s^*} \cdot \left(\ln \left(\frac{4\alpha_s t}{r_b^2} \right) - \gamma \right) + q \cdot R_b^* \quad (1.6)$$

1.2.1.2 Infinite Cylinder Source

The infinite cylinder source (ICS) model is a pure conduction solution for a cylinder which has constant, continuous heat transfer beginning at time, $t = 0$. Spitler and Bernier (2016) outline several forms of the ICS model:

- A form where the inside of the cylinder is empty with all heat flowing outward from the radius of the cylinder (Carslaw and Jaeger (1959), p. 338). This form neglects the thermal mass of the borehole. In order to accurately apply this form, a model of the GHE must be applied in conjunction with this model.
- A form where the inside of the cylinder is a perfect conductor with a specified thermal capacitance (Carslaw and Jaeger (1959), pp. 342–345). Several different forms of this equation are given, but this form accounts for the thermal capacity of the GHE.
- A form which treats composite cylindrical regions with the inside of the cylinder as having different properties than the surrounding soil (Carslaw and Jaeger (1959), p. 347).

Applying the first form, the mean fluid temperature can be calculated by Equation 1.7.

$$T_f = T_s + \frac{q}{k_s^*} \cdot G(Fo) + q \cdot R_b^* \quad (1.7)$$

where Fo is the Fourier Number $= \alpha_s t / r_b^2$. $G(Fo)$, is given in Equation 1.8,

$$G(Fo) = \frac{1}{\pi^2} \int_0^\infty \left(e^{-x^2 Fo} - 1 \right) \frac{J_0(x)Y_1(x) - Y_0(x)J_1(x)}{x^2 (J_1^2(x) + Y_1^2(x))} dx \quad (1.8)$$

J_0 , J_1 , Y_0 , and Y_1 are zeroth- and first-order Bessel functions of the first- and

second-kind. Computation of Equation 1.8 is computationally expensive, therefore Bernier (2001) has provided a curve fit of $G(Fo)$ based on tabular data from Ingersoll et al. (1954). This curve fit is given in Equation 1.9.

$$G(Fo) = 10^b$$

$$b = -0.89129 + 0.36081 \cdot \log_{10}(Fo) \tag{1.9}$$

$$- 0.05508 \cdot \log_{10}^2(Fo) + 3.59617 \times 10^{-3} \cdot \log_{10}^3(Fo)$$

Diao et al. (2004) developed an infinite moving line source model which can account for the effects of ground water flow. Ingersoll et al. (1954) developed an infinite phase-change line source model, which is the only analytical solution that can account for ice formation. Man et al. (2010) developed a infinite solid cylindrical source model. Li and Lai (2012) have developed an infinite helical line source solution.

All of these models have the advantage that they are relatively simple to implement and fast to compute. However, they all have a number of limitations which reduce their accuracy to predict the behavior of a real GHE system. Some of these limitations are given here:

- These models are “infinite” models, therefore ground surface effects are not included. This effect may be small for very deep boreholes but will increase with decreasing borehole depth due to the periodic soil temperature profile near the ground surface. Similarly, the end effects at the bottom of the GHE are not accounted for.
- Variations in soil properties are not included. The thermal properties of soil, just like any other material, tend to vary under different conditions, such as with variations in temperature and moisture content. More commonly, soil properties vary with depth since the earth’s crust is composed of many different layers and soil types which vary greatly with geography.

- These models assume constant, continuous heat transfer from time, $t = 0$, but are only valid when $t > 5r_b^2/\alpha_s$. Therefore, short-term GHE effects cannot be captured with these models.

1.2.2 Response Factor Models

Another set of models that have been used for simulating GHE are response factor models. These so called “response factors” are also commonly referred to as “g-functions.” g-functions are curves which represent the non-dimensional temperature rise of, depending on formulation, the borehole wall, GHE mean fluid temperature, or GHE exiting fluid temperature. The g-functions are also specific to the GHE configuration, which is determined by the geometry of each borehole and the flow-path configuration.

These models take advantage of Duhamel’s theorem (Duhamel, 1828; Özişik, 2002) which allows the time-varying loads to be applied as piece-wise step loads. As a result, this temporal superposition allows for the GHE to be modeled with loads which evolve over time. This is seen in Figure 1.2 where we can see that a series of step pulses of different magnitude and duration can be applied to give the effective total load. The temperature response to the individual heat pulses and the total load are seen in Figure 1.3.

Spatially, the temperature response of two individual boreholes also can be added together to determine the combined response. Simplified conduction models often treat GHE as infinite or finite line or cylinder heat sources conducting into an infinite medium. Carefully applying the principle of superposition along with these simplified models can yield acceptable results.

Professor Johan Claesson began applying the principle of superposition to GHE modeling (Claesson and Dunand, 1983), and later, along with his Ph.D. student Per Eskilson (Eskilson, 1987; Claesson and Eskilson, 1988) developed the response

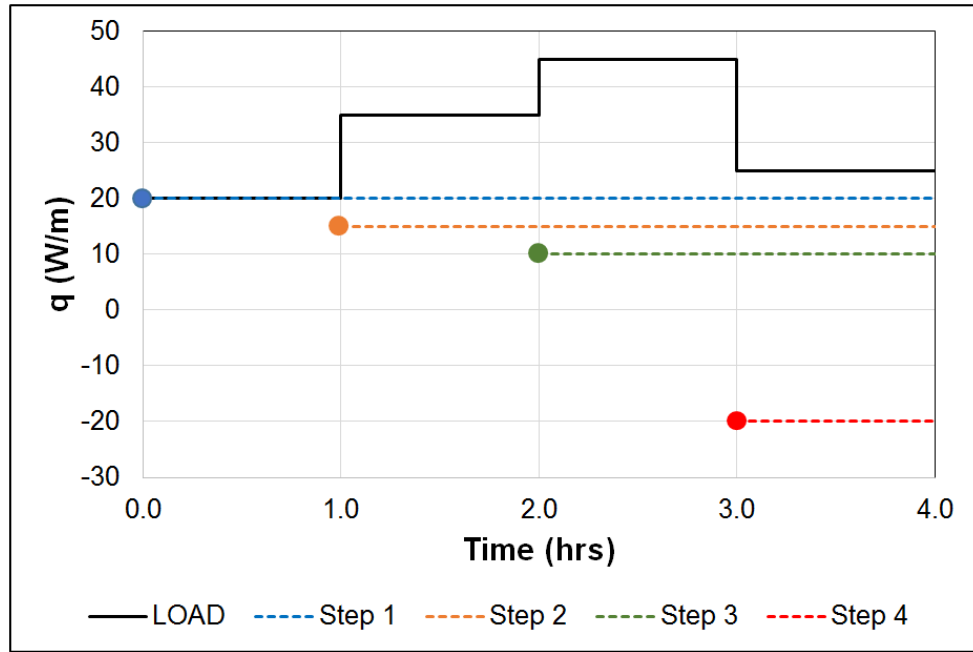


Figure 1.2: Heat pulse steps. Reprinted, by permission, from Spitler and Bernier (2016).

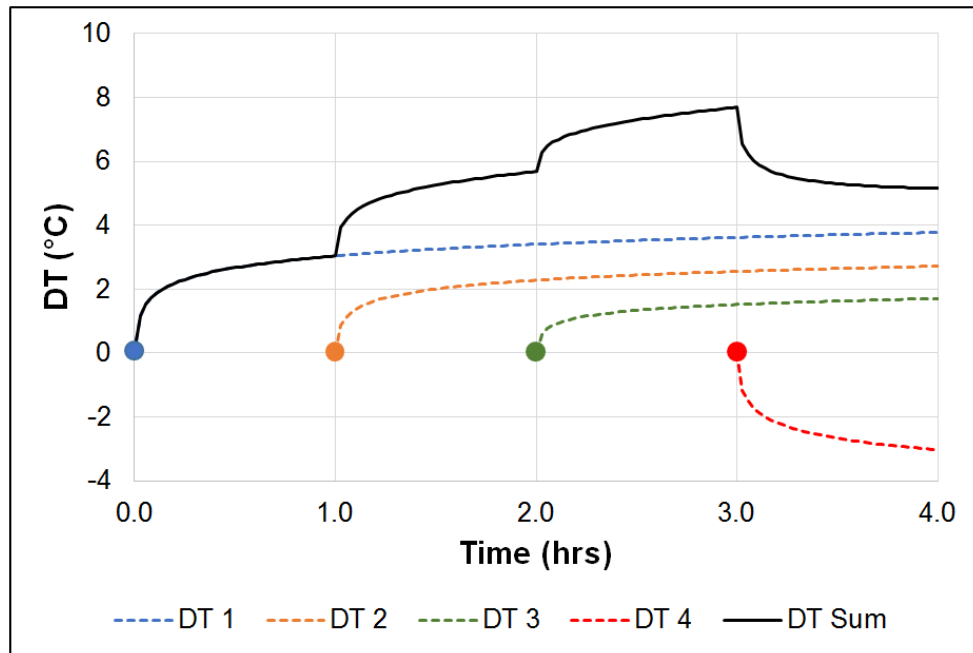


Figure 1.3: Temperature response to heat pulses. Reprinted, by permission, from Spitler and Bernier (2016).

factor models commonly used today. The average borehole wall temperature can be computed for a single, constant heat pulse from Equation 1.10, or for a series of piece-wise heat pulses as shown in Equation 1.11.

$$T_b = T_s + \frac{q}{2\pi k_s^*} \cdot g(t/t_s, r_b/H, B/H, D/H) \quad (1.10)$$

$$T_b = T_s + \sum_{i=1}^n \frac{q_i - q_{i-1}}{2\pi k_s^*} \cdot g\left(\frac{t_n - t_{i-1}}{t_s}, r_b/H, B/H, D/H\right) \quad (1.11)$$

T_b is the average borehole wall temperature, T_s is the undisturbed soil temperature, q is the average heat extraction rate per unit length, k_s^* is the effective soil conductivity, and g is the g-function. The g-functions are non-dimensionalized based on the characteristic time of the borehole field, $t_s = H^2/9\alpha_s$, where H is the borehole length and α_s is the soil thermal diffusivity. D is the depth of the GHE below ground surface and B is the GHE center-to-center spacing.

Example g-functions for a 3×2 rectangular GHE array are given in Figure 1.4. It should be noted that the depth, D may represent the location where the “active” GHE begins. Water filled boreholes, which are common Sweden and other Northern European countries, will have air at the top of the GHE above the water table line. At these locations along the GHE there is effectively no heat transfer with the surrounding soil.

As currently presented, the model is not useful for WBES simulations of GHE. One of the problems we have is that the model is formulated in terms of known heat loads. However, this creates problems for implementation within WBES programs since these values are not expected to be known before hand. If needed, the WBES could assume GHE fluid temperatures to get an estimate of the GHE loads, then feed those loads to GHE design tools such as GLHEPro (Spitler, 2000), which often rely on known GHE loads to compute the GHE fluid temperature. These temperatures

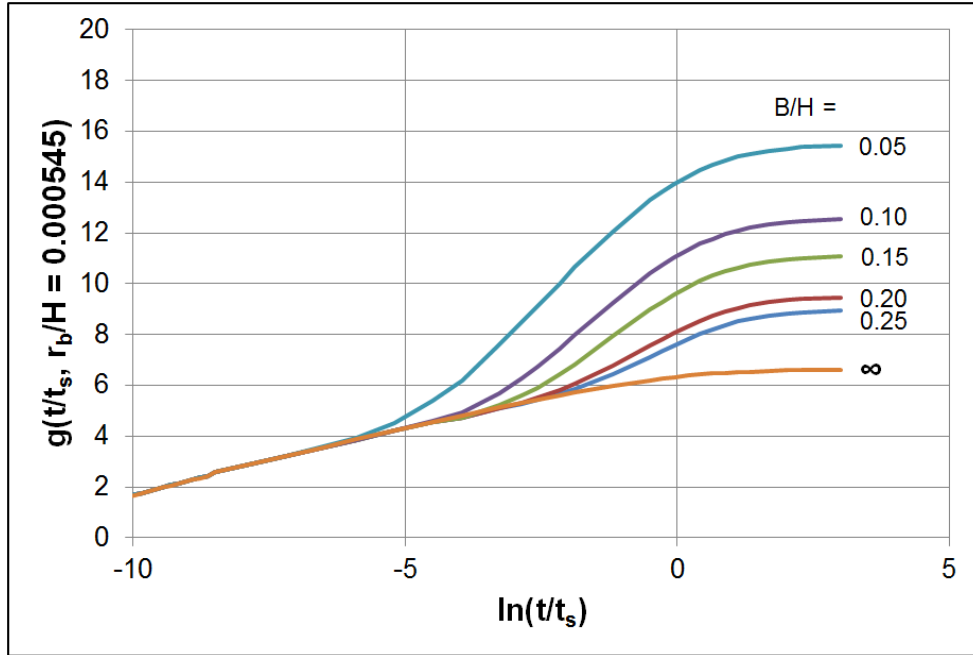


Figure 1.4: Example g-functions for a 3×2 rectangular GHE array

could then be fed back to the WBES, and iterated once again for a more accurate estimate of the GHE's performance and its effect on the system it is connected to. However, this creates a requirement for the simulation user to iterate between the WBES program the GHE design tools. Obviously, this is not preferred.

Another problem with the previous formulation is that the original g-function models assumed that the heat transfer rate, q , used to drive the model be the GHE heat transfer rate from the borehole wall to the surrounding soil, q_b . From the perspective of the WBES program, though, this presents a problem since the circulating fluid is what connects plant-loop components. Therefore, the accuracy of the heat transfer rate of the circulating fluid, q_f , is more important and more appropriate. At long time steps or during steady-state operation, $q_b \approx q_f$; however, at short time steps this is not true.

Yet another problem with the previous formulation is that Claesson and Eskilson only provided g-functions for a handful of GHE configurations. In addition, these available g-functions were only computed down to a non-dimensional time value of

$\ln(t/t_s) = -8.5$, though methods have also been developed for extending these g-functions so simulation of hourly, or even sub-hourly time steps. In real time this represents about 62 h for a GHE with an average length, $H = 100$ m, and soil thermal diffusivity, $\alpha_s = 1 \times 10^{-6}$ m/s², so short time step g-function generation methods will be required.

Finally, the current model performs poorly at short time steps during highly transient loads. This is seen in Figure 1.5, where step pulse loads are applied to the response factor GHE model, which is implemented in EnergyPlus.

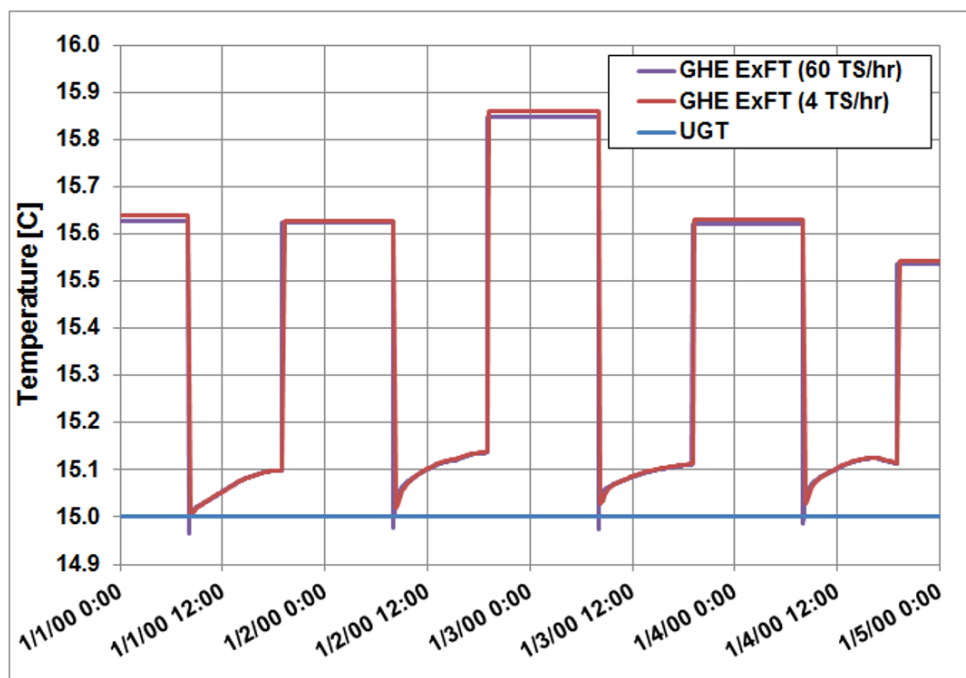


Figure 1.5: Non-physical results from EnergyPlus response factor model

Here, UGT represents the undisturbed ground temperature. The other two data series show the GHE exiting fluid temperature at 60 time steps per hour ($\Delta t = 1$ min) and 4 time steps per hour ($\Delta t = 15$ min). At short time steps during high transient load periods, the exiting fluid temperature prediction is non-physical. This is seen by the temperature dip below the undisturbed ground temperature. However, for the simulation with 4 time steps per hour this non-physical behavior is not present.

The reason for this can partly be understood from the model derivation discussion,

and partly from the data shown in Figure 1.6. Figure 1.6 shows the g-function data for a single borehole GHE, with a borehole radius of $r_b = 0.05$ m and length of $H = 100$ m. The g-function data came from GLHEPro (Spitler, 2000), which uses a library to look up the Eskilson (1987) long time step g-functions, and a radial finite-volume model (Xu and Spitler, 2006) to compute the short time step g-functions. Long time step g-functions are given for values of $\ln(t/t_s) \geq -8.5$ and short time step g-function values are given for values of $\ln(t/t_s) < -8.5$.

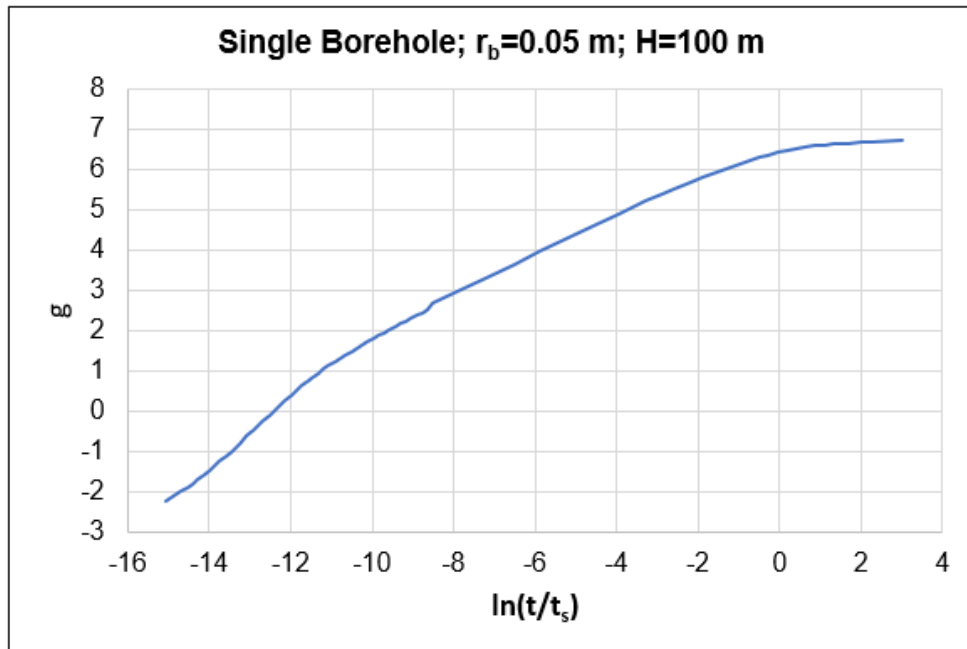


Figure 1.6: g-functions example for single borehole

Remember that horizontal axis represents non-dimensional time as referenced from the present simulation time. Values farther to the left represent the g-functions computed for short time steps; g-function values farther to the right represent times which occurred farther in the past from the present simulation time. Also remember that the g-function values themselves represent the temperature rise of the borehole wall, which has been non-dimensionalized for the soil resistance and heat load.

Keeping this in mind, we see that for this plot of g-function values, the g-function is negative below approximately $\ln(t/t_s) = -13$. The reason for this goes back to

how the short time step g-function models have been derived, which is to assume that $q_b \approx q_f$. The result of this assumption is that the effective borehole wall temperature for short time steps is negative, which is a non-physical value. Brussieux and Bernier (2018) show that this value approaches $-2\pi k_s R_b$, as shown in Equation 1.12. For the data shown in Figure 1.6 where the soil thermal conductivity, $k_s = 2.423 \text{ W}/(\text{m K})$, and the borehole thermal resistance, $R_b = 0.19 \text{ K}/(\text{W}/\text{m})$, short time step g-function values will approach $\ln(t/t_s) = -2.9$.

$$\lim_{t \rightarrow 0} \ln(t/t_s) = -2\pi k_s R_b \quad (1.12)$$

These issues limit the ability of the response factor model to simulate short time step, high transient load situations.

Response factors models are relatively simple to implement, and when combined with load aggregation methods result in relatively low simulation times. However, they too have limitations. Some of which are listed here:

- The g-function approach is relatively simple to implement, but it relies on g-functions which are computed before the simulation, the computation of which is complicated and computationally intensive. These are generally stored in a library; however, interpolation between different data sets within the library can introduce inaccuracies.
- Currently available g-function simulation approaches produce non-physical behavior when simulating step loads at short time steps. These limit the confidence modelers will have in the methods.

1.2.3 Thermal Resistance-Capacity Models

Another approach which has seen some advances as of recently is the thermal resistance-capacitance model (TRCM) network approach which models the GHE internal ge-

ometries with a simplified RC-network, as is seen in Figure 1.7. These models can be formulated to solve for the heat transfer within the borehole by developing a network of temperature nodes that represent the temperature at different locations within the borehole. These temperature nodes are computed by defining an energy balance equation at each node. This energy balance generally also includes a transient term which accounts for the thermal capacitance of the node. This allows the dynamic evolution of the node temperature over time to be determined.

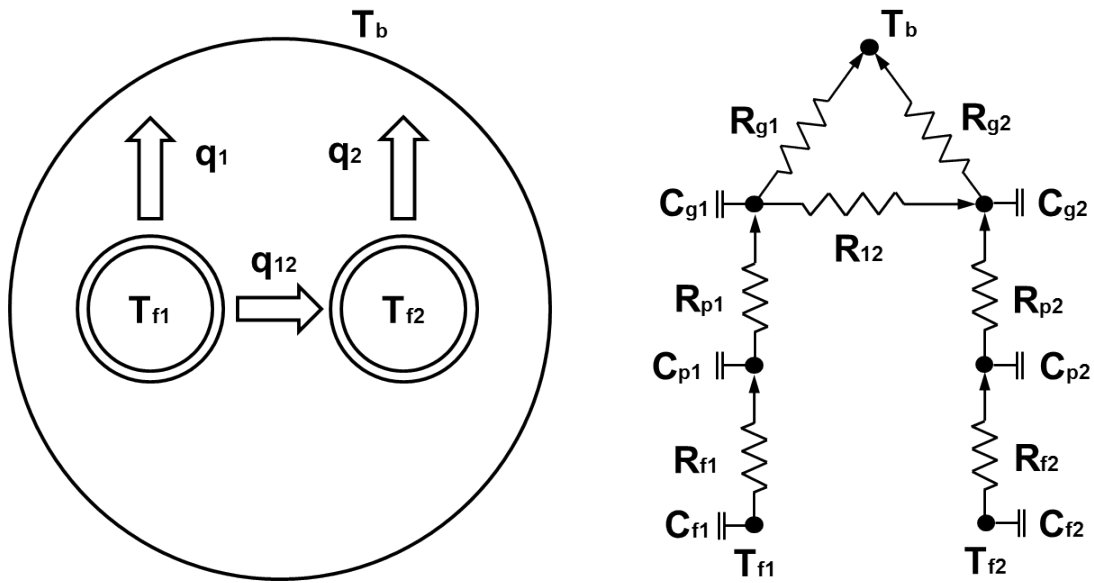


Figure 1.7: RC-network geometrical representation.

The approach has a benefit in that it does not require direct simulation of all of the geometry within the borehole, as would be done with pure numerical models which use finite-element, finite-volume, or finite-difference computations. The result is that the temperature for each node can be solved for by simultaneously solving a set of equations, such as the following example in Equation 1.13, where the left-hand side of the equation represents the transient temperature change with time, and the right-hand side represents the energy flows between this node and its neighboring nodes.

$$\rho c_p \frac{dT_i^{t+\Delta t}}{dt} = \sum_{j=1}^n \frac{T_j^t - T_i^t}{R_{i,j}} \quad (1.13)$$

In this equation, the thermal capacitance of the node is represented by the product of the density, ρ , and the specific heat, c_p , and the resistance between the i and j nodes is given as $R_{i,j}$. Here, t represents the current time, while $t + \Delta t$ represents the time at the next time step.

A number of works have been published which discuss the use of TRCM model: however most of them are not performed in the context of WBES environments. These will be discussed first, then later the TRCM models with potential application within WBES will be discussed.

De Carli et al. (2010) apply a Delta-circuit resistance network model (Eskilson and Claesson, 1988), along with several annular regions to create a 1D radial model of vertical slices of the GHE. The vertical slices are then connected to give a quasi-2D model of the GHE. A numerical model was used to determine the sensitivity of the RC-network model to the number of vertical slices and horizontal annular layers. The model was then compared to numerical model and against experimental data from an office building in Mestre-Venice, Italy. The model only considers a local, steady-state resistance within the borehole, therefore, the model performs poorly under transient conditions. This is not surprising given that the thermal capacitance of the borehole is not accounted for.

Zarella et al. (2011) developed a model based on the work by De Carli et al. (2010). The authors improved on the model by improving the way thermal capacitance was treated within the original model. A 100 m borehole was discretized into 20 vertical slices and 20 annular regions from the axis of the borehole. The model was then compared to results from a TRT and shown to have reasonable agreement.

Bauer et al. (2011) developed TRCM for coaxial, single U-tube, and double U-tube configurations. The models were validated against a finite element numerical simu-

lation and showed good performance when compared to the Delta-circuit resistance model only. The authors state that the TRCM approach is best suited for applications in transient energy simulation programs, such as TRNSYS (Klein et al., 2016) or EnergyPlus (Crawley et al., 2001); however, this assertion appears to be qualified primarily by the needs of WBES for accurate simulation of time-varying loads, and not due to the need for rapid simulation time.

Pasquier and Marcotte (2012) take the TRCM approach further by adding additional capacity elements within the borehole to improve the short-term transient behavior of the models. Pasquier and Marcotte (2014) further extend this model by incorporating the spectral element solution method and by developing a way to interconnect the TRCM's into a quasi-3D model.

Ruiz-Calvo et al. (2015) developed another quasi-3D TRCM which is solved numerically using the Lax and Wendroff (1960) approach. Cazorla-Marín et al. (2017) applied the model and used a TRT to validate the results. The authors state that the model required 20 seconds to solve for the 72 hour TRT test, and 6 seconds to solve for a 24 hour TRT on a modern PC. No information is given as to the state of the programming language, parallelization, etc. Cazorla-Marín et al. (2018) also discusses the effects of ground temperature node location.

Godefroy et al. (2016) developed a TRCM for simulating heat transfer within the borehole. Borehole wall temperature is determined by using the cylinder source solution. The models were implemented in TRNSYS and compared against a 48 hour TRT and 47 days of experimental data from a test house at the Canadian Centre for Housing Technology with simulated occupancy. The authors compared the differences between applying and neglecting borehole thermal capacity, and noted an overestimation of up to 3.6% of heat pump energy consumption when it is neglected. The model and experimental data comparison showed excellent agreement with a GHE outlet temperature RMSE difference of 0.28 °C.

Kerme and Fung (2019) also developed a detailed TRCM which uses a Crank-Nicolson implicit numerical method to solve for all node temperatures. The authors provide parametric data from their model where they discuss the effects of the number of vertical nodes and radial nodes, as well as time step size. The model is stated to provide accurate and stable results at up to 5 m vertical node distances, 0.1 m radial node distances, and 1 h time steps. The authors also studied the effects of flow rate and different circulating fluids.

Ruiz-Calvo et al. (2016) describe what is potentially the most promising application of a TRCM for WBES applications. The authors use the TRCM to compute the heat transfer within the GHE, but then use a response factor model to update the borehole wall boundary temperature. This temperature is updated periodically so that the computations are only performed when needed. The authors simulate the performance of a GHE for 1-month and compare the results to experimental data taken in Spain. The method shows promise regarding its accuracy; however, no information is discussed regarding simulation time required.

The models just described represent stand alone models which were used to simulate GHE for relatively short time periods. WBES simulation often run annual simulations of the entire building and connected systems within a matter of a few seconds. In addition to that, GHE often need to be simulated for multiple decades to determine whether they have been sized appropriately. Therefore, it seems like a direct application of a TRCM model within a WBES environment would increase simulation time significantly, perhaps by several orders of magnitude. This would be considered unacceptable by designers who rely on WBES to perform rapid simulations for parametric analysis and design.

TRCM models are also more complicated to implement due to the complexity of the mathematical methods required. Finally, due to the formulation of the TRCM temperature node equations, as shown in the example in Equation 1.13, small time

steps may be required in order to preserve numerical stability.

The TRCM model presented here show some promise by demonstrating ways of overcoming some of the short comings of previous models. There are, however, a few drawbacks which should be noted.

- Despite being simpler than previous “pure” numerical models, the models apply complex mathematical concepts which will require some expertise in these fields when implementing solutions.
- Computation time will be better than pure numerical models, but are may not be sufficient for implementation within a WBES. The model by Ruiz-Calvo et al. (2015) required 20 seconds to solve for a 72 hour TRT, whereas WBES could likely simulate an annual simulation for a full building in that same time.

1.2.4 Numerical Models

Numerical methods, such as finite element or finite volume methods, have been applied to this problem by a number of different authors. Al-Khoury (2010) developed two pure numerical solutions for modeling GHE. The first solution is based on forming the problem of 1D conduction from a GHE based on a discrete Fourier transform, then using an fast Fourier transform (FFT) algorithm to compute the inverse Fourier transform. The second solution is based on applying spectral elements (Doyle, 1988, 1997). Both solutions are compared to an analytical solution and both compare very well; however, the spectral element method is stated as being more computationally efficient. Shao et al. (2016) apply these methods to develop a code base which is publicly distributed (<https://github.com/ufz/ogs5>).

A number of other pure numerical models have been developed for simulating GHE performance (Al-Khoury et al., 2005; Al-Khoury and Bonnier, 2006; He et al., 2011; Nabi and Al-Khoury, 2012a,b). They are also often use as a validation method for other “simplified” models (e.g. Bauer et al. (2011); Pasquier and Marcotte (2012,

2014)).

Numerical models have the advantage that they are highly customizable and are able to capture many of the effects needed to accurately model GHE systems. Nevertheless, they too have a number of limitations, some of which are listed here:

- The models are complicated to implement. Numerical integration and matrix inversion schemes are also required which can be complicated to implement and costly to compute.
- The models require a computational mesh be generated which fits the GHE geometry. These meshes can be complicated to develop due to the asymmetric nature of the U-tubes in the GHE. GHE also have a large range of length scales that need to be accounted for. Pipe wall thickness is on the order of tens of millimeters, whereas the borehole depth and farfield boundary will likely be on the order of hundreds meters. As a result, it is not likely that a simple Cartesian-type mesh, which could be manually generated, will be sufficient to model the problem.
- Numerical models are generally slow to compute due to their added complexity. This is especially true for models of complete GHE arrays which contain multiple boreholes. As a result they are not practical to use within the context of WBES, with the possible exception of a research-only environment.

1.2.5 Borehole Thermal Resistance Models

For GHE designers, determining the temperature of the borehole wall, which is typically what is solved for by ILS, ICS, and FLS models, is not particularly useful. Rather, they are more interested in the response of the borehole fluid to a given inlet flow rate and temperature. In order to determine the fluid temperature when using the ILS, ICS, FLS, and RC-network models, some models for the borehole thermal resistance need to be applied. Optimizing borehole thermal resistance is also important

given that lower the borehole thermal resistance results in better GHE performance. Javed and Spitler (2016) and Javed and Spitler (2017) have reviewed a significant number of these borehole resistance calculation methods and clarified a number of ambiguities regarding terminology and nomenclature.

Mogensen (1983) introduced the concept of borehole thermal resistance along with the method of using a TRT to estimate it. Depending on the resistance network assumed, a number of different “resistance” values related to the borehole thermal resistance can be determined. However, the two most notable borehole resistance values are the “local” and “effective” borehole resistance values. Note that Equations 1.4, 1.6, and 1.7 are all based on the effective borehole resistance.

The local, steady-state borehole resistance can be calculated as shown in Equation 1.14.

$$R_b = \frac{T_{f,l} - T_b}{q} \quad (1.14)$$

T_b is the borehole wall temperature, $T_{f,l}$ is the local mean fluid temperature of the two U-tube legs at a given depth, and q is the heat dissipated per unit length of the GHE.

The effective, steady-state borehole resistance can be calculated as show in Equation 1.15.

$$R_b^* = \frac{T_f - T_b}{q} \quad (1.15)$$

T_f is the averaged-over-the-depth fluid temperature.

The key difference between the local borehole resistance and the effective borehole resistance is that the local borehole resistance is based on the simple mean fluid temperature, whereas the effective borehole resistance requires an averaged-over-the-depth fluid temperature. Hellström (1991) defined relationships between these two

resistances for the uniform borehole wall temperature and uniform heat flux cases, though neither applies perfectly. Generally a mean value between the two is used.

The difference between the effective borehole resistance, R_b^* , and the local borehole resistance, R_b , is caused by short-circuiting between the two U-tube legs. This thermal short circuiting reduces the heat transfer effectiveness of the borehole, though for most systems the effects are often negligible. Thermal short-circuiting is primarily affected by the flow rate in the system and the depth of the borehole. For very deep boreholes, the residence time of the fluid (i.e. the time it take the fluid to transit the borehole piping) is large, and therefore any thermal interactions between the U-tube legs will cause the averaged-over-the-depth temperature to deviate from the simple mean temperature. The same can be said for boreholes with very low flow rates.

As has been mentioned, there has been a lot of work performed previously by authors seeking the best, most robust method for calculating borehole thermal resistance. By far, the best method to this point is the multipole method, as presented in Hellström (1991). Claesson (2011) and Claesson and Hellström (2011) also offer later works on the subject. The multipole method is a complex algorithm that allows users to analytically calculate thermal resistance values between any number of pipes placed arbitrarily in a borehole. The primary advantage of the method is that, for low-order solutions with symmetrical U-tubes, relatively simple-to-compute sets of closed-form algebraic solutions for calculating borehole resistances can be derived.

The multipole method has been compared to a number of numerical methods with exceptional accuracy (Al-Chalabi, 2013; Go et al., 2014; He, 2012; Lamarche et al., 2010; Liao et al., 2012). A full set of equations for the zeroth- and first-order multipole expressions applied to single U-tube GHE for calculating R_b and R_b^* have been given by Javed and Spitler (2017), and therefore will not be repeated here. It should be noted, however, that the when the first-order and tenth-order multipole expressions are evaluated, the results rarely differ by more than 1%. Therefore the first-order

expressions are generally considered sufficient for the purposes of GHE modeling.

None of the thermal resistance methods, however, are able to account for the transient effects of changing inlet conditions of the GHE. All methods implicitly assume that the heat transfer is uniform along the length of the GHE. However, the borehole resistances, depending on which value is to be determined, are based on either the mean GHE inlet and outlet temperatures or the averaged-over-the-depth fluid temperature. If load or flow rate changes occur, none of these models would be able to account for these transient effects which occur at time scales smaller than the transit time of the GHE.

Beier and Spitler (2016) developed a model which extends the use of 1D radial models which include the thermal storage of the circulating fluid. Weighting factors are applied to the inlet and outlet temperatures which allow computation of more accurate GHE inlet and outlet temperatures after short-term changes have occurred. At periods before the steady-flux period, the model uses an empirical function to determine the weighting factor which is an improvement over steady-flux models which represent the average borehole fluid temperature as the mean of the inlet and outlet temperatures. The model was compared to a quasi-3D model and to experimental TRT data and shown to be in good agreement. Later, Beier et al. (2018) validated the model using a multi-flow rate TRT.

Borehole resistance models, up to this point have had difficulty modeling the variable thermal resistance of the borehole. Some methods have been developed which show promise in correcting this issue, but none have yet been applied to a WBES.

1.2.6 Load Aggregation Methods

Due to the linear properties of the underlying conduction problem, superposition in time and space can be applied. Yavuzturk and Spitler (1999) were the first to

recognize this and apply it temporally when computing and using short-time step g-function solutions. The authors pointed out that the number of computations required when applying Equation 1.11 is proportional to the square of the number of time steps. GHE simulations are often run for several decades of simulation time when performing sizing calculations. This presents a significant computational burden at an hourly or smaller time step.

The authors were able to reduce simulation time significantly—with little loss in accuracy—by aggregating the loads most distant from the current simulation time into simulation blocks with the average load of the original non-aggregated loads. Loads from the current simulation time up until 192 hours in the past were not aggregated and were simulated with the original hourly time step. Loads which occurred before the most recent 192 hours in the past from the current simulation time were aggregated into 730 hour blocks, which roughly correspond to 1 month of time. By applying this scheme, the authors were able to achieve a 90% reduction in simulation time for an annual simulation. For a 20 year simulation, the simulation time was reduced to significantly less than 1% of the non-aggregated simulation time. Murugappan (2002) later extended this model to include sub-hourly time steps within EnergyPlus.

Bernier et al. (2004) developed a similar scheme; however, this time the load aggregation blocks were defined as 12, 48, 168, and 360 hour long blocks. This method also showed significant promise in reducing the simulation time. The method reduced simulation runtime in the TRNSYS program from 20–25 minutes to about 3 minutes.

Liu (2005) develops a “hierarchical” load aggregation scheme using three levels for small, medium, and large load aggregation blocks along with a specific waiting period for each block level. Load aggregation operations are only processed once enough smaller blocks have been accumulated to compose a larger block, and the waiting

period has passed. A small block represents 24 hours, with a 12 hour waiting period; a medium block consists of 5 small blocks with a 3 small block waiting period; a large block consists of 73 medium blocks with a waiting period of 40 medium blocks.

Marcotte and Pasquier (2008) applied a geometrically expanding scheme for load aggregation. Starting from t_0 equals the present time and counting backwards, hours 1–48 are not aggregated and therefore the loads during these periods are simulated directly. From there, the load blocks are constructed as follows: hours 49–50, 51–54, 55–62, 63–78, 79–110, and so forth up the series. The method is claimed to be more accurate than the method presented by Bernier et al. (2004). For a 20-year hourly simulation, the current method will require 65 terms, whereas 969 terms are required for the Yavuzturk and Spitler (1999) method, and 119 for the Liu (2005) method.

Claesson and Javed (2012) developed another load aggregation scheme using different levels of aggregation size, where the number of loads in a block within each level, r_q , is given by Equation 1.16. The authors selected 16 levels for their comparison, but this could be extended as needed. The authors also state that doubling the number of hours aggregated by a block in each level could be changed, and that this value was chosen arbitrarily and is not optimized.

$$\begin{aligned}
 r_q &= 2^{q-1} \\
 q &= 1, \dots, q_{max}
 \end{aligned}
 \tag{1.16}$$

The number of load cells within each level was chosen to be 5. The total number of load blocks is $5 \cdot 16 = 80$. The loads are time-shifted from one block to another, rather than creating static load blocks which are time-shifted as a block. This causes some time-shift dispersion of the loads; however, the authors state that the most dispersion occurs at loads which are farthest in the past history from the present calculations. Therefore, the effects of the time-shift dispersion are not significant.

The authors are careful to preserve the total energy of the load block, but not to preserve the amplitude of each individual load, as this information is lost once the load aggregation block is created. The authors also state that the method results in a $200\times$ faster simulation over the non-aggregated load scheme for a 20 year simulation

1.2.7 Response Factor Generation Models

Response factor models have historically been used for simulating GHE performance within WBES. This is due to their relatively simple implementation and their fast computational speed, both of which are important for WBES simulation users. As a result of this, they are expected to continue to be used in this application in the future.

However, the method relies on the g-functions to be generated before the simulation has been run. In this section, we will review the methods used to generate these g-functions.

1.2.7.1 Superposition Borehole Model

Professor Johan Claesson and his student Per Eskilson (Eskilson, 1987; Eskilson and Claesson, 1988) were the first to apply the principle of superposition to GHE modeling. As a result, they created what is known as the superposition borehole model (SBM) to generate g-functions. The method modeled a single borehole using a 2D radial-axial grid on a coarse numerical mesh. The heat transfer within the borehole was assumed to be treated separately, therefore, the heat transfer rate computed by the model was from the borehole wall to the surrounding soil. Some discussion has been had over the years since the original model was developed regarding what boundary conditions were applied at the borehole wall. Cimmino and Bernier (2014) investigate this issue in detail and conclude that the original SBM applied a uniform borehole wall temperature along the full length of the borehole, and that this

temperature is uniform for all boreholes.

From this model, the temperature field data for all time steps is determined for a single borehole. Then, the temperature field is superimposed depending on the GHE configuration. The average borehole wall temperature is then determined, and presented as the non-dimensional g-functions.

Using this model, the authors published the data for approximately 50 different regular shaped GHE fields, such as GHE arranged in linear, triangular, rectangular, and square configurations. These data have been the historical backbone of response factor GHE simulation models and have been distributed as a library for use in GHE design tools. For GHE configurations which are not contained in the library, different methods have been developed to interpolate between or extrapolate to the required g-function data. Special care must be taken when doing this; however, as pointed out by Malayappan and Spitler (2013) since this interpolation can introduce errors. The non-dimensionalized g-functions for a limited number of different GHE field arrangements were also provided. Although not explicitly stated, the g-function library by Eskilson (1987) is believed to have been derived with uniform borehole wall temperature boundary condition and the top of the borehole beginning at 5 m below ground surface.

Since this model is based on a finite-volume formulation, the computation time is expected to be greater than some of the more recent models which have been developed for generating g-functions.

1.2.7.2 Line- and Cylinder-Source Models

Line- and cylinder-source models may also be used to generate g-functions. The methods are often treated as an “exact” analytical solution which is used for validating other g-function generation methods. These methods will have some limitations, though, which are outlined here.

Due to the geometry of the model, meaning, due to the infinite line- or cylinder-source solution within an infinite medium, the methods will not be valid at certain temporal periods. Since the internal geometry of the borehole is not considered, and due to various assumptions made regarding the thermal capacity of the borehole, ILS and ICS g-functions are not valid until after a certain time period. Often, this time is taken as $t > 5r_b^2/\alpha_s$, which can be several hours. Similarly, due to the infinite nature of the models, they will also not be accurate at predicting periods when the GHE may interact with the ground surface.

1.2.7.3 Finite Line-Source Models

Finite line source (FLS) models, like the ILS and ICS models are relatively easy to compute and allow for the ground surface and GHE end effects to be taken into account. FLS models function by integrating point source solutions over finite line segments which are located a distance D from the ground surface. In order to take into account ground surface effects, a “mirror” image of the line segments are generated and mirrored about the ground surface, as is seen in Figure 1.8. The temperature response of the GHE array is determined by taking the average of the temperature response of each segment on each GHE. The individual temperature response of each segment is calculated based on its interactions with all other segments including, all mirrored segments to account for ground surface effects.

Marcotte and Pasquier (2009) developed a FLS model that assumes a uniform borehole wall heat flux boundary condition which can be used to model any arbitrary configuration of GHE’s, even GHE which are inclined in arbitrary directions. The model was validated against a 3D finite element model discretized into 170,000 finite elements. The general model is given in Equation 1.17 which gives the temperature rise, ΔT , at point i due to point j . The result can then be used to compute the response factor values after summing the total effect over all points and averaging the

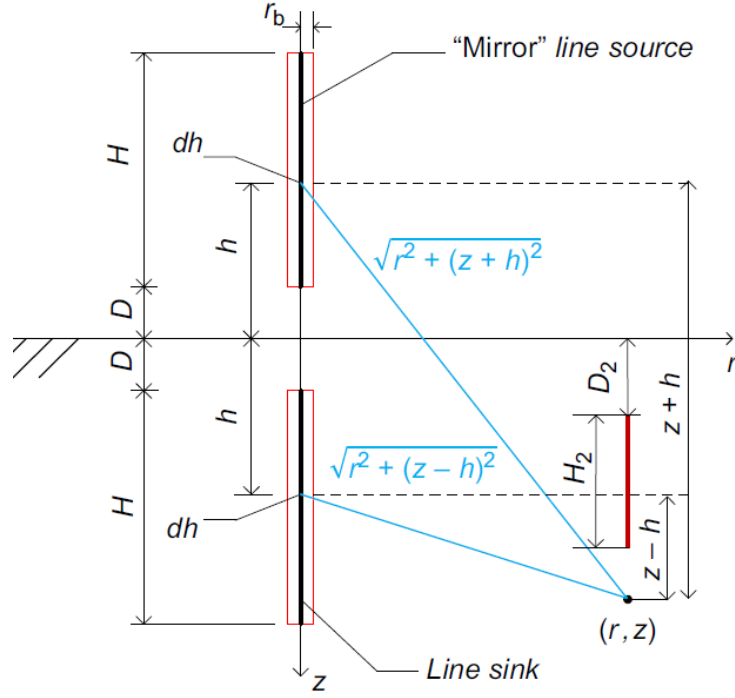


Figure 1.8: Finite line source geometrical representation. Reprinted, by permission, from Spitler and Bernier (2016).

effects.

$$\begin{aligned}
 \Delta T_{j \rightarrow i}(t) = & \frac{q_j}{4\pi k_s H_j} \int_{x_1^i}^{x_2^i} \int_{x_1^j}^{x_2^j} \frac{\operatorname{erfc}(d(x, x')/2\sqrt{\alpha_s t})}{d(x, x')} dx dx' \\
 & - \frac{q_j}{4\pi k_s H_j} \int_{x_1^i}^{x_2^i} \int_{y_1^j}^{y_2^j} \frac{\operatorname{erfc}(d(x, y)/2\sqrt{\alpha_s t})}{d(x, y)} dx dy
 \end{aligned} \tag{1.17}$$

Grundmann (2016) took this model and used it to develop temperature response factors for any GHE array configuration, including inclined GHE. The so called “Free Placement Finite Line Source” model was included in GLHEPro (Spitler, 2000), Version 5. The model has been observed to have sensitivity to the number of line segments that each GHE is discretized into. As implemented by Grundmann (2016), the i -th GHE is discretized into 50 segments and the j -th GHE is discretized into 560 segments, though no reason is given as to why these numbers were chosen.

Lamarche and Beauchamp (2007) and Javed and Claesson (2011) have also developed simplified single integral forms of the line source models, though the model by Lamarche and Beauchamp (2007) is only applicable for when $D = 0$, where D is the borehole depth below the ground surface.

Cimmino and Bernier (2014) developed a semi-analytical method to generate response factors. The authors used a discretized finite line source model, which was then transformed into the Laplace domain and solved using a FFT numerical algorithm. The model is capable of simulating different borehole wall boundary conditions.

Marcotte and Pasquier (2014) developed a line source model (based on Lamarche and Beauchamp (2007) and Claesson and Javed (2011)) for computing response factors with series or parallel GHE arrangements. The model was validated using a 3D numerical simulation.

Cimmino (2018a) later developed a “fast” method for calculating g-functions which takes advantage of symmetry with the borefield to simplify and reduce computations. For a 10×10 borefield using a single processor, the g-functions required nearly 500 seconds to generate using code implemented in Python. The author later extended this model to compute g-functions for GHE with series- or parallel-connected boreholes Cimmino (2018b). The code for this library is published online (Cimmino, 2018c).

1.2.7.4 Numerical Methods

Yavuzturk and Spitler (1999) were the first to develop, so called, short time step g-functions. These g-functions extend the standard long time step g-functions as generated by Eskilson and Claesson (1988) down so hourly, or sub-hourly time step simulations can occur. The model used an angular-radial finite volume model of the borehole, and could simulate any time scale. However, it could not account for varying thermal resistance of the fluid mass.

Xu and Spitler (2006); Xu (2007) develop a simplified radial finite-volume model of the borehole which used an equivalent pipe diameter to simplify the borehole internal geometry. Equivalent thermal masses within the borehole were applied to the simplified geometry. Additionally, the thermal resistances were set using the multipole method (Bennet et al., 1987; Claesson, 2011; Claesson and Hellström, 2011; Javed and Spitler, 2017), which is a highly accurate analytical algorithm for computing the thermal resistance within the borehole. The model works well for determining short time step g-functions, but is not suitable for determining g-functions for thermally interacting GHE.

Brussieux and Bernier (2018) implement another equivalent-radius radial numerical model for the purpose of generating short time step g-functions. The model evaluates the heat transfer between the fluid and the borehole wall using the finite-volume method by Patankar (1991), as was done by Xu and Spitler (2006). However, the heat transfer between the borehole wall and soil was evaluated analytically using the ICS solution.

Acuña et al. (2012) and later Monzó et al. (2013) generate g-functions using commercial multiphysics software. The authors assume a uniform heat flux boundary condition at the borehole wall. In the case of Acuña et al. (2012), the authors use between approximately 100k to 300k elements within the mesh in order to simulate an 8×8 rectangular GHE with radial soil boundary from 40 m to 50 m. No description of the simulation time is given; however, the computational expense for this type of simulation is expected to be high relative to the other g-function generation methods discussed.

1.2.7.5 Other Methods for Response Factor Generation

Several other promising methods have been developed in recent years for the development or approximation of g-functions. Dusseault et al. (2018) describes a block-matrix

formulation which simultaneously represents the thermal effects of all boreholes for all time steps. Then, the method builds on the FLS model proposed by Claesson and Javed (2011). However, instead of numerically integrating the integrand, it is replaced by Chebyshev polynomials and integrated analytically. By combining these two methods, the authors are able to accelerate g-function generation methods. The authors claim to be able to generate g-functions for a GHE containing 50 boreholes for a period of 40 years in under 0.5s. Computations were performed on a simple laptop computer, but computer programming language is not discussed.

Others, including Pasquier et al. (2018) and Dusseault and Pasquier (2018) have utilized artificial neural networks to approximate g-functions, once the network has been trained properly. In the case of the former study, the authors use a TRCM model to generate the training data needed by the ANN; in the later study, the authors utilize the block-matrix formulation to generate the training data.

1.3 Discussion

Previous sections have focused on describing current GHE models, along with their uses and limitations. This section will focus on some of the practical issues which are encountered by GHE designers and installers. These issues are difficult to model properly and are often treated with assumptions or ignored all together. More importantly, it is important to recognize their limitations within the context of a WBES. WBES programs such as EnergyPlus are already complicated programs which model the heat and mass transfer, and energy flows through a building.

Some of the practical limitations of current GHE simulation methods which limit general applicability to real-world situations are listed here:

1.3.1 Simulation Time

In EnergyPlus, the physical building geometry and building material properties are used to generate a building model. From there, the simulations are driven by occupancy and usage schedules for internal equipment and loads, and location specific weather information which provides air temperatures and solar data for simulating the external environment. The simulation methodologies generally consist of simulating the zone with an internal heat balance which models the internal loads and air heat balance, and an external heat balance which models the solar and convective energy transfer through fenestrations and building surfaces. Often the ground energy transfer is treated with heavily idealized assumptions, but recently some methods have been incorporated to treat this more accurately (Lee, 2013; Kruis and Krarti, 2015). The internal and external zone heat balances are coupled together through the building surface conduction models.

Plant and HVAC elements (e.g. pumps, heat pumps, pipes, fans, compressors) are simulated simultaneously within a plant loop solver or an HVAC loop solver. The feedback between the zone heat balance and the plant/HVAC loop solvers is one of the important features of the models which helps allow accurate and realistic simulation of whole buildings.

Since programs such as EnergyPlus are commonly used by designers to perform design iterations and parametric studies, the simulation algorithms need to execute as fast as possible. It is not uncommon for a building such as a hospital to have hundreds of rooms with thousands of surfaces. Each room may be conditioned by its own heat pump, be connected to a variable air volume terminal unit, operate with a variable refrigerant volume unit, or any number of other system combinations. All the while these systems are connected to one or more plant- and air-loop simulations which are all interacting with one another. Currently, EnergyPlus does not (yet) incorporate parallel processing algorithms, so all computations are performed successively on a

single computational process. Some example annual simulations using EnergyPlus, Version 8.8 (EnergyPlus, 2017) are given below in Figure 1.9. Additional data regarding the simulations are given in Table 1.1. All simulations used the Chicago-O’Hare weather data file distributed with EnergyPlus. All simulations were performed on a Windows 7 desktop PC, with an Intel i7-4770 8 core 3.4 GHz processor, with 16 GB RAM.

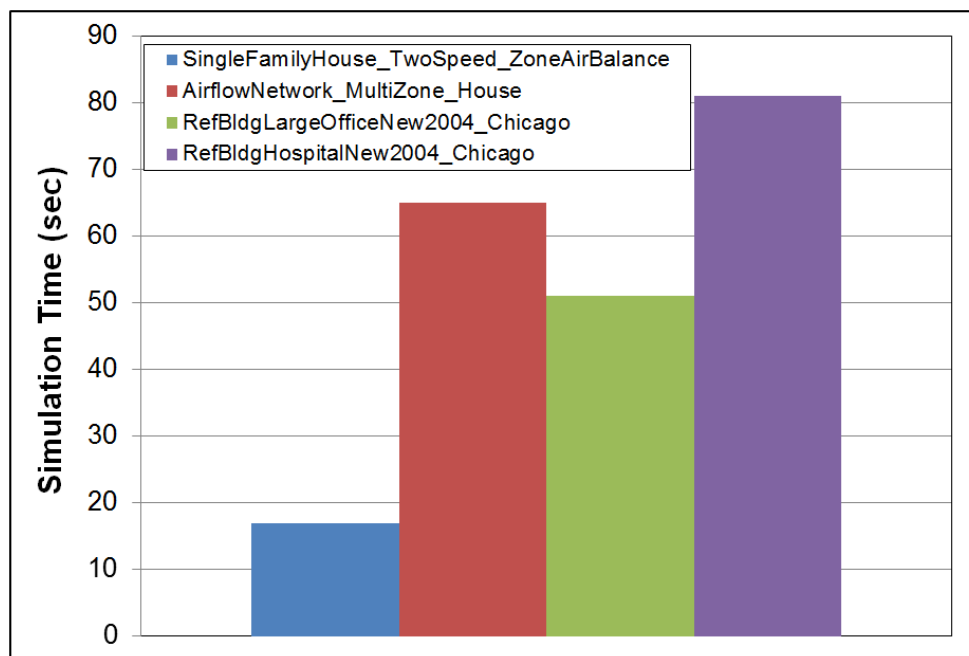


Figure 1.9: Example EnergyPlus simulation times for different building types

Table 1.1: Data from EnergyPlus example simulations

| File Name | Bldg Surf | Fenest | Zones | Sim Time (sec) |
|---|-----------|--------|-------|----------------|
| SingleFamilyHouse_TwoSpeed_ZoneAirBalance | 25 | 4 | 3 | 17 |
| AirflowNetwork_MultiZone_House | 25 | 4 | 3 | 65 |
| RefBldgLargeOfficeNew2004_Chicago | 130 | 12 | 15 | 51 |
| RefBldgHospitalNew2004_Chicago | 402 | 40 | 55 | 81 |

The test files used to generate Figure 1.9 and Table 1.1 come from EnergyPlus, V8.8 example files, which are distributed with the installation. Deru et al. (2011) gives additional data regarding the “RefBldg” files. From the data presented in the

figure and table, we can see that there is a large difference between buildings being simulated. On one end, we see two simulations of a three-zone house (living zone, attic zone, and garage zone). For these two simulations, the “SingleFamilyHouse” simulation required 17 seconds to simulate, whereas the “AirFlowNetwork” simulation required 65 seconds to simulate. On the other end of the building complexity spectrum, we have a hospital with 55 zones, 402 surfaces, and 40 fenestrations, and a large office with 130 building surfaces, 15 zones, and 12 fenestrations. For the large office, the model represents a 12 story with basement office building. However, only the basement, first story, level 6, and top story were modeled. A multiplier for level 6 was added to account for the additional building levels, without actually modeling them. Simulation times were 81 and 51 seconds, respectively, for the hospital and large office.

For the large building, the simulation time is quite manageable with a mean value of about 65 seconds. Different control strategies, or other complications could add to the runtime, but as presented with standard controls and plant equipment the simulation times are acceptable.

For the house simulations, the “SingleFamilyHouse” simulation uses a single lumped zone assumption with user specified infiltration rates, whereas the “AirFlowNetwork” house uses a more detailed pressure driven simulation algorithm to compute building infiltration based on wind speed, surface orientation, HVAC system leakage, etc. The simulation time for these vary significantly, from 17 seconds to 65 seconds, respectively. Based on this, we infer that there is some precedent within EnergyPlus to allow simulation time to increase when more detailed models are requested by the user. In this case, an increase in simulation time of $3.8\times$ is seen.

Determining the upper limit of what users would find “acceptable,” however, is a subjective question. It seems likely, though, that if the increase in simulation time were, say $300\times$, users may not readily adopt such methods except in the most extreme

situations.

One point worth noting: typically GHE simulations are run for multiple years and sometimes multiple decades to determine whether a GHE is sized properly. This is not necessary for a standard WBES without a GHE since a standard weather file is almost always used and the build performance from year to year is not expected to change, especially if the building does not incorporate a detailed simulation of the ground heat transfer effects through the building foundation. However, this multi-year simulation is possibly the only way to determine whether a GHE array is sized properly and determine if the building performance over that time period is acceptable. Any increase in simulation time for an annual simulation may create an additional penalty when adding multi-year simulations.

Therefore, with this information in mind we see that an acceptable simulation time is critical for WBES models to be adopted and used. The modeling methods incorporated during this work should, to the best extent possible, not worsen the simulation time.

1.3.2 Non-uniform GHE Array Arrangements

Non-uniform GHE arrangements are common in real-world designs. This means that, due largely to site constraints, boreholes are often not laid out in a uniform grid or other regular pattern such as L-shaped, U-shaped, rectangular, open box, etc. Similarly, pile heat exchangers are building foundation elements which have one or more U-tubes that have been installed within cast-in-place or pre-cast concrete. The location of these piles is based on architectural and structural considerations, and are therefore not placed in regular patterns.

The temperature response of boreholes which are placed in non-uniform arrangements can be computed using the FLS methods mentioned previously. The library approach which requires libraries of precomputed response factors is not practical for

these situations due to the infinite number of variations which could occur. If given no other option, designers would likely pick the closest configuration for which they have library data, or apply an FLS method to generate response factors which are specific to their particular geometry. These response factors could be reused once computed.

Therefore, the models developed during this work should be able to accurately model non-uniform GHE arrangements. Design of the model input structures should also be simple for users to apply for both uniform and non-uniform GHE arrangements. This may mean having several single input objects devoted to specific uniform GHE arrangements, and a simplified data object which allows placement of individual GHE.

1.3.3 Non-uniform GHE Depths

Response factor libraries often only treat GHE where all boreholes have the same depth. Often however, GHE are installed at non-uniform depths due to issues occurring during installation. This may lead to different flow rates in different boreholes. A designer performing due diligence would necessarily want to verify that these alterations to the design would meet the project's needs. However, this cannot be done with current models.

Again the FLS methods can handle these situations, but may be limited by computation time required. The library approach also fails in this situation.

Therefore, the models developed during this work should be able to model non-uniform GHE design depths, as this is a situation which occurs frequently in practice.

1.3.4 Non-Uniform GHE Inlet Conditions

Most GHE models treat the GHE inlet conditions for a GHE array as uniform (i.e. uniform flow rates and entering fluid temperatures). This is an appropriate approximation for GHE arrays with properly sized header pipes, uniform GHE depths, and all

GHE connected in parallel. For GHE which are connected in a series arrangement, the outlet temperature of one GHE will be the inlet temperature of the next GHE. For systems where GHE may be installed at different depths, the flow balance will be affected and non-uniform flow rates could be expected. Systems which have had improperly sized header pipes installed could also experience flow imbalance problems.

An example application is described by Hammock and Sullens (2017) where a building thermal energy storage (BTES) system was designed for a U.S. Marine logistics base in Albany, GA. The system uses 306, 200 m GHE with a minimum of 6.9 m spacing. The GHE are arranged in a “bullseye” pattern with concentric rings of interconnected GHE. The hot water from the chiller condenser enters the GHE on the external ring and then is piped in parallel cascading inward to the center of the GHE array.

Another example is described by Bernier and Cauret (2014) where experimental data from a GHE array of short boreholes piped in parallel were used to short GHE piped in parallel. The response factors were precomputed using an FLS model for long times (> 1 day), and a cylindrical heat source model for short times. A TRCM model was also used, which discretized each GHE into 5 segments. A single far-field ground temperature was used. The GHE array is composed of a 4×4 array with 9 m boreholes spaced 3 m apart in the vertical and horizontal directions. Each borehole row is connected together in series. The GHE rows are piped together in parallel, except that the flow direction changes for every other row; i.e. row 1 flows left, row 2 flows right, row 3 flows left, and row 4 flows right.

Their model shows some differences from the experimental data during heat pump startup times and state that their results would improve if a better estimate of the far-field ground temperature had been used. The results do compare well at the end of the heat pump cycle, though. The authors state that the simulated and measured heat extraction rates agree within $\pm 10\%$. This underscores the importance of using

an accurate estimate of the undisturbed ground temperature near the surface.

Therefore, any models developed during this work should be able to model non-uniform GHE inlet conditions such as would happen when GHE are piped in series, or when piped in parallel and have non-uniform depths.

1.3.5 Non-Uniform GHE Boundary Conditions

In theory, undisturbed ground temperatures vary periodically with depth; however, other effects can also cause disturbances in ground temperature. One such ground temperature disturbance could be due to buildings which have been installed in an area prior to the construction of a GHE. Gehlin et al. (2016) state that in urban areas, the heat leakage from buildings can significantly impact the temperature profile along the borehole. Along with these temperature variations, the soil moisture content will vary depending on the local climate. These effects are especially important for shallow GHE systems.

Thermal interference from other GHE are of primary concern and methods have been developed to model these situations. However, the GHE boundary condition which are assumed by the models also will have an effect on GHE performance and should not be neglected.

A recent study by Juhlin and Gehlin (2017) has shown that GHE depth in Sweden has been steadily increasing over the past decades. From 1980 to 2015 the mean depth for GHE installations of all sizes has increased from 120 m to 180 m. Gehlin et al. (2016) have shown that in Sweden where the heat pumps are primarily used for heating, the ground temperature can begin to increase below a depth of 120 m. This increase in ground temperature at this specific depth is site specific in this instance. In general; however, we expect ground temperature to increase steadily with depth due to the earth's geothermal heat flux. Pushing GHE's deeper into the ground will usually result in more advantageous ground temperatures for heating dominated sys-

tems. Increasing GHE depth; however, will also increase the thermal short-circuiting between the upward and downward legs of the GHE. Holmberg (2016) and Holmberg et al. (2016) also noted that for groundwater filled GHE the natural convection between the U-tube and the borehole wall significantly reduces the borehole thermal resistance, but its effects should be treated on a local scale. Spitler et al. (2016) have developed natural convection correlations for water-filled GHE, and notes the effects that different boundary conditions and short circuiting on the accuracy of the results.

The work performed by Bernier and Cauret (2014) is also relevant here. With the alternating series-piped GHE rows piped in parallel, the boundary conditions seen by each GHE is different than typically is expected for a parallel piped GHE array.

These models do show promise, but again, no generalized design methodology has been established which will allow simulation of such systems in the context of a WBES. So as a result, the models demonstrate a “one off” model which is unique to that particular system.

Therefore, any models developed during this work should not only be able to account for borehole-to-borehole interference, but should also be able to account for non-uniform ground temperatures and the effects of increased thermal short circuiting.

1.3.6 Modifying an Existing GHE System

Current models assume that the GHE has not been operated previously and that the GHE initial temperature is equal to the far-field ground temperature. This will be true at the beginning of a GHE’s operational lifetime. However, any changes to the system invalidate this assumption. For example, if the owner of a building with an existing GHE array decides to construct an addition to the building; or, perhaps the existing building load is expected to change significantly, say, if an office space is converted to server space. In these situations, the building owner may wish to add additional capacity to their already existing GHE system. In an ideal world, the

expansion would be constructed far away from the existing installation, but this may be impossible in actuality.

Another example is changing to a more efficient heat pump in a heating dominated climate (or a less efficient heat pump in a cooling dominated climate). In a heating dominated application, changing to a more efficient heat pump will result in *increasing* the energy extracted from the ground. Thus, systems which have been operating without issue for several decades may find that their boreholes are undersized after installing a new, more efficient heat pump.

Claesson (2013) discusses this issue for older heat pump systems in Sweden. Early adopters of heat pumps in Sweden typically applied a “rule of thumb” design method, and systems were only designed to accommodate 50% of the peak heating load. Newer systems apply more advanced design techniques and typically design for the heat pump system to handle 70% of the peak load. In these situations, designers may wish to drill additional depth in an already existing GHE to account for the increase in energy which needs to be extracted from the ground.

In both situations, the system designer will have few resources to pull from when attempting to model the system performance.

Yu et al. (2017) use an FLS model to simulate zoning effects on GHE performance. In the study, a 20×20 square GHE array is simulated with a 1.6:1 summer to winter load ratio. The GHE was loaded in the three summer months with 666 kW, while in the three winter months it was loaded with 411 kW. During the other six months, the system was not operated. Additionally, during the winter months the outer two rows of the GHE array were not operated, so as to extract as much heat from the center of the array as possible. This effectively reduced the GHE size to 18×18 during these months.

The results showed that the zoning operation can significantly improve the GHE outlet temperatures and enhance system performance. For operation with no zoning

operation in effect, after year 17 of a 20 year simulation the study’s “failure” benchmark was met. A failure was is caused when the GHE outlet temperature exceeds 40 °C. With the zoning operation, at year 20 the GHE outlet temperature was around 34 °C.

The work by Hammock and Sullens (2017) should also be referenced here. In their system, the GHE are piped in parallel in a “bullseye” configuration. When the system heat pumps are operating in cooling mode, the hot water is piped from the external ring to the center of the bullseye. During winter heating operations, the flow through the GHE is reversed and heat is extracted from the center of the GHE array in order to utilize energy previously stored in the GHE.

Therefore, the model developed during this work needs to accurately handle the effects of changing the GHE configuration over time.

1.3.7 Small Simulation Time Steps

GHE, when simulated independently from a building, are generally simulated for multiple decades, and operate on hourly or longer simulation time steps. Whole building energy simulations on the other hand, can and often do simulate equipment at time steps on the order of minutes to seconds. Zone and building structure elements may be simulated at longer time steps, but system components often need to be simulated at shorter time steps to resolve any transient effects. Current GHE models in building simulations often are not able to handle these types of situations, which can result in non-physical behavior of the system at short time steps.

Therefore, any models developed need to accurately model the short-term transient behavior of GHE systems regardless of the overall system level simulation time step.

1.4 Objectives

The objectives of this study are to improve the modeling capabilities of vertical GHE within the context of whole building energy simulations. Whole building energy simulation programs continue to be developed and used widely by architects, engineers, and energy analysts. As a result, it is important that this community have a GHE model which is generalized and sufficiently robust so as to handle the most important and practical design conditions.

Therefore, this study seeks to develop an accurate, tested, and validated WBES GHE model which can:

1. Simulate with simulation times that are acceptable for WBES. See Section 1.3.1.
2. Simulate non-uniform GHE arrangements. See Section 1.3.2.
3. Simulate non-uniform GHE depths. See Section 1.3.3.
4. Simulate non-uniform GHE inlet conditions. See Section 1.3.4.
5. Simulate non-uniform GHE boundary conditions. See Section 1.3.5.
6. Simulate GHE systems that change configuration over time. See Section 1.3.6.
7. Simulate short time step behavior of GHE. See Section 1.3.7.

1.5 Outline

The objective of this work is to improve the modeling capabilities of vertical GHE within the context of whole building energy simulations. The following is a brief description of each of the following chapters.

- Chapter 2 discusses load aggregation procedures, and how they can be optimized to enhance simulation time and accuracy. A large parametric study is performed, and results and recommendations are given.
- Chapter 3 develops an enhanced ground heat exchanger model for use in whole-building energy simulations. Experimental data from a multi-flow rate thermal

response test are used to validate the model.

- Chapter 4 develops cross-g-functions for use in simulating the interactions between thermally interacting ground heat exchangers.
- Chapter 5 presents a brief summary, conclusions, and recommendations for future work.

CHAPTER II

CHARACTERIZATION, TESTING AND OPTIMIZATION OF LOAD AGGREGATION METHODS FOR GROUND HEAT EXCHANGER RESPONSE-FACTOR MODELS

Abstract

Ground heat exchangers are often simulated using response factor-type models which rely on the GHE load history. As the simulation progresses, the number of GHE load history terms which need to be included in the temperature response computation grows. For extended, multi-year simulations the required computation time due to these history terms can be excessive which limits the usefulness of response factor-type models. To cope with this, load aggregation procedures have been developed that preserve the net effect the individual loads but reduce the overall number of computations.

The previously developed load aggregation methods can be characterized as two different methods, but with different parameters. The parameters each affect the accuracy and computational efficiency of the methods, yet there has been no systematic investigation of the parameter space. In this chapter, both methods are implemented and compared for a wide range of parameters. A final recommendation is made which results in a 73-fold reduction in simulation time when compared to non-aggregated simulations. For a worst-case situation with an imbalanced load profile on a densely packed borehole field, the MBE is less than 0.13 °C for five- and ten-year simulations. The resulting predicted heat pump energy consumption error is less than 0.3%.

This chapter is a paper which has been accepted for publication in the journal *Science and Technology for the Built Environment*.

2.1 Introduction

Ground source heat pump (GSHP) systems and their associated ground heat exchangers (GHE) are frequently installed to provide for efficient, economical building heating and cooling. However, due to the complex nature of the thermally interacting ground heat exchangers, it is often difficult to apply rule-of-thumb-based design approaches. Since the GHE represents potentially the largest single-item cost of a GSHP system, it is important for it to be designed properly. Therefore, for GSHP systems to be designed properly and compared against other heating and cooling systems, designers need the ability to simulate and compare the competing systems. Due to this, a great amount of effort has been put towards developing simulation models for GSHP and GHE systems.

One such GHE model that is often used for performing GHE simulations is the response factor model which originally was developed by developed Prof. Johan Claesson and his Ph.D. Student, Per Eskilson (Claesson and Eskilson, 1985; Eskilson, 1987; Eskilson and Claesson, 1988; Claesson and Eskilson, 1988). The model relies on spatial superposition and pre-computed response factors known as “g-functions.” For vertical GHE (which are often referred to as a borehole for a single GHE, or as “borehole fields” or “bore fields” for a group of boreholes), the g-functions are developed specifically for the GHE’s geometric arrangement of boreholes, including parameters such as borehole active length, H , borehole burial depth below the ground surface, D , borehole-to-borehole spacing, B , and borehole radius, r_b . The response factors then allow the borehole wall temperature response to be computed based on an assumption of constant borehole heat input rate, q , as is seen in 2.1

$$T_f = T_s + \frac{q}{2\pi k_s} \cdot g(t/t_s, r_b/H, B/H, D/H) \quad (2.1)$$

A variety of methods have been developed for computing g-functions, including

but not limited the methods described in the following works by Eskilson (1987); Yavuzturk and Spitler (1999); Zeng et al. (2002); Xu and Spitler (2006); Lamarche and Beauchamp (2007); Javed and Claesson (2011); Cimmino and Bernier (2014); Cimmino (2018a). Response factors methods have also been widely adopted and implemented in several popular building or GHE simulation programs, such as: EnergyPlus (Murugappan, 2002; Fisher et al., 2006), TRNSYS (Klein et al., 2016), and GLHEPro (Spitler, 2000). Details regarding how the response factor are developed and used will vary depending on application, so the reader should further consult additional literature for a treatment of these topics.

To account for temporally varying loads on the GHE, temporal superposition is used as shown in Equation 2.2, where i is the index denoting the end of a time step and n is the index denoting the current time step. Furthermore, by assuming quasi-steady state heat transfer, the mean fluid temperature, T_f , can be related to the borehole wall temperature, T_b , using the borehole thermal resistance, R_b , as shown in Equations 2.3 and 2.4. Further details can be found in Spitler and Bernier (2016). In these equations, when $i = 1$, $q_0 = 0$ which represents the GHE load at $t = 0$. By default, this will be 0 since no previous loads are assumed to have occurred.

$$T_b = T_s + \sum_{i=1}^n \frac{q_i - q_{i-1}}{2\pi k_s} \cdot g\left(\frac{t_n - t_{i-1}}{t_s}, r_b/H, B/H, D/H\right) \quad (2.2)$$

$$T_f = T_b + q_n \cdot R_b \quad (2.3)$$

$$T_f = T_s + \sum_{i=1}^n \frac{q_i - q_{i-1}}{2\pi k_s} \cdot g\left(\frac{t_n - t_{i-1}}{t_s}, r_b/H, B/H, D/H\right) + q_n \cdot R_b \quad (2.4)$$

A practical issue that arises from this temporal superposition of past loads, however, is the fact that the number of superposition calculations grows with the square

of the number of time steps (Yavuzturk and Spitler, 1999). As a result, applying this approach directly will greatly affect simulation runtime. For example, hourly annual or hourly multi-year simulations may be impractical without some way to reduce the number of computations required.

Therefore, in order to reduce runtime, load aggregation procedures have been developed which will reduce the number of superposition calculations. This results in reductions to the required simulation runtime. Load aggregation is the process of taking several individual loads that occurred over a given time interval and replacing them with a single load over the same time interval. If the individual loads occurred over uniform time step intervals the average load rate could be computed and applied for the aggregated load. If the loads have non-uniform time steps an energy-balance approach should be taken to ensure that energy is conserved.

An idealized load aggregation example is described here and in Table 2.1 The most current simulation time is represented by bin 1, which represents simulation time t_n . This bin has a duration of 1 time step, h . The load which is to be tracked, q_n , is the energy, e_n , divided by time step duration, h . As time steps occur, existing loads are displaced and shifted (right) farther into the GHE's load history. Further descriptions of the aggregation example are given below.

Table 2.1: Idealized aggregation example.

| Sim. Time | t_n | t_{n-1} | $t_{n-2} - t_{n-4}$ | $t_{n-4} - t_{n-6}$ |
|-----------|------------------|------------------|----------------------|----------------------|
| Duration | $1h$ | $1h$ | $2h$ | $2h$ |
| Bin No. | 1 | 2 | 3 | 4 |
| Time step | | | | |
| 1 | $\frac{e_1}{1h}$ | | | |
| 2 | $\frac{e_2}{1h}$ | $\frac{e_1}{1h}$ | | |
| 3 | $\frac{e_3}{1h}$ | $\frac{e_2}{1h}$ | $\frac{e_1}{2h}$ | |
| 4 | $\frac{e_4}{1h}$ | $\frac{e_3}{1h}$ | $\frac{e_1+e_2}{2h}$ | |
| 5 | $\frac{e_5}{1h}$ | $\frac{e_4}{1h}$ | $\frac{e_2+e_3}{2h}$ | $\frac{e_1}{2h}$ |
| 6 | $\frac{e_6}{1h}$ | $\frac{e_5}{1h}$ | $\frac{e_3+e_4}{2h}$ | $\frac{e_1+e_2}{2h}$ |

- Time step 1: a load, q_1 , occurs. The time duration for bin 1 is $1h$, so the energy

which is to be tracked for that time step, e_1 , is added to the bin.

- Time step 2: a new load, q_2 , occurs. The load in bin 1 is displaced into bin 2 and the new load which occurred at the current time step is placed in bin 1.
- Time step 3: a new load, q_3 , occurs. The load in bin 2 is displaced to bin 3, and similarly from bin 1 to 2. Bin 3 has a duration of 2 time steps, $2h$, therefore the energy which came from bin 2 now represents an average load over the bin's duration. This is shown by $e_1/2h$. As an example, if the load q_1 were 1 kW and the time step, h , were 1 hour, e_1 would represent 1 kWh of energy. It's average load over this time period of $2h$ is now $1/2$ kW.
- Time step 4: a new load, q_4 , occurs and the remaining loads are displaced as before. Bin 3 now contains e_1 and e_2 . Again, this bin has a duration of $2h$, therefore, it represents an average load over this time.
- Time steps 5-6: the previous process is repeated, with loads being displaced from recent bins into bins which represent times further in the past.

In the above example, the loads from 6 time steps are aggregated into 4 bins. When considering this example along with Equation 2.4, we can see that some computations have been eliminated. An example of how this temporal superposition is applied is given in Equation 2.5.

$$\begin{aligned}
T_{f,4} = T_s & \\
& + \frac{1}{2\pi k_s} \left(\frac{e_4}{1h} - \frac{e_3}{1h} \right) \cdot g \left(\frac{t_4 - t_3}{t_s} \right) \\
& + \frac{1}{2\pi k_s} \left(\frac{e_3}{1h} - \frac{e_1 + e_2}{2h} \right) \cdot g \left(\frac{t_4 - t_1}{t_s} \right) \\
& + \frac{1}{2\pi k_s} \left(\frac{e_1 + e_2}{2h} - 0 \right) \cdot g \left(\frac{t_4 - t_0}{t_s} \right) \\
& + q_4 \cdot R_b
\end{aligned} \tag{2.5}$$

In Equation 2.5, Equation 2.4 is applied with the values from Table 2.1 at time

step 4. The second, third, and fourth lines of the equation demonstrate the application of temporal superposition to compute the step loads which are applied to the GHE. Here, the g-function value, g , is assumed to be taken at the appropriate GHE configurations parameters of r_b/H , B/H , and D/H . The g-function values are computed as referenced from the current simulation time to the end of $i - 1$ bin.

Some questions arise from this simple example:

1. *What is the best method for transitioning loads from one bin to another?*

In the above example, the loads transitioned perfectly as is seen at time steps 4, 5 and 6. At time step 4, the energy from t_1 was retained in bin 3, and at time step 5 the same energy is shifted into the next bin. However, in practice, this is likely not possible. The value of the total energy in the bin is the only information which is expected to be retained, not the individual energy values. As a result, the information regarding “when” and “how much” energy should be shifted is lost. Individual load values could be retained this would defeat the purpose of the load aggregation method all together.

2. *How many aggregation bins should there be?*

In this example, the number of aggregation bins was 4 with a total interval of $6h$. Would there be any advantage to having more or fewer bins?

3. *How much time should each bin represent, and how should these bins be oriented relative to one another?*

This example keeps 2 bins from each level and then doubles their duration from h to $2h$. Is expanding the bin duration with a $2\times$ multiplier best, or are there other variations of this parameter which will give better results?

This study aims to answer these questions by comparing and optimizing current load aggregation methods. Several different load aggregation methods have been proposed. However, there has not been a direct comparison of the methods. Additionally, input parameters to the existing methods have not been optimized with the goal of

minimizing simulation runtime and maximizing accuracy. The work presented here describes the process used to test these aggregation algorithms, eventually leading to recommendations for a method and its respective parameters.

2.2 Literature Review

Several different load aggregation procedures have been proposed. These will be outlined and described here.

2.2.1 Static Methods

Yavuzturk and Spitler (1999) were the first to develop a load aggregation procedure to reduce simulation runtime for response factor models. The method relies on using “monthly” heat pulses to aggregate 730 hourly loads, though the method retains 192 hourly heat pulses for the most recent 192 simulation hours. In other words, once the first 922 ($192 + 730$) hours have passed, the 730 hours which are farthest in the past from the current simulation time are aggregated together. Once another 730 hours have passed the next 730 hours are aggregated into another bin. This process is repeated for the duration of the simulation.

Fundamentally, this method forms the basis for what is referred to in this paper as the “static” method. The method is characterized by smaller load bins which collapse into larger bins once enough of the smaller bins have been created. As this method is applied to the Yavuzturk and Spitler (1999) model, the smaller hourly-bins collapsed into the larger 730-hour bins after a sufficient number of smaller bins have been created.

The method could loosely be thought of as similar to the Lagrangian approach which, in the case of fluid flow characterizations, tracks individual particles or packets of fluid rather than tracking a fixed control volume through which fluid flows. In our case, however, we are concerned with tracking individual loads or load bins which

are formed from previously aggregated smaller bins. Once enough bins have been created, they collapse into larger bins. After a bin is formed, the load values remain within the bin until the bin is aggregated together with other similar bins.

The method is referred to as “static” because once the loads bins have been created, loads do not move in or out of the bin; i.e. the loads are “static” relative to the bin. Smaller bins can collapse into larger bins, but the loads themselves do not move out of the bin once the bin has been created.

To illustrate this, consider the example given in Table 2.2. In this example, we will assume that the time steps, h , have a value of 1 hour, and that we will keep a minimum of $3h$ before aggregating 2, $1h$ -bins into a single $2h$ -bin.

Table 2.2: Static method aggregation example

| Bin No. | | 1 | 2 | 3 | 4 | 5 |
|-----------|-------|-----|-----|-----|-------|-------|
| Time Step | | | | | | |
| 1 | Width | h | | | | |
| | Load | 1 | | | | |
| 2 | Width | h | h | | | |
| | Load | 0 | 1 | | | |
| 3 | Width | h | h | h | | |
| | Load | 0 | 0 | 1 | | |
| 4 | Width | h | h | h | h | |
| | Load | 0 | 0 | 0 | 1 | |
| 5 | Width | h | h | h | $2h$ | |
| | Load | 0 | 0 | 0 | $1/2$ | |
| 6 | Width | h | h | h | h | $2h$ |
| | Load | 0 | 0 | 0 | 0 | $1/2$ |
| 7 | Width | h | h | h | $2h$ | $2h$ |
| | Load | 0 | 0 | 0 | 0 | $1/2$ |

The steps occurring at each time step are described below.

- Time step 1: a new load with a value of 1 kW occurs. Because the time step is 1 hour, the energy represented by this load is 1 kWh which is placed in bin 1.
- Time steps 2-4: the load from bin 1 from the previous time step is displaced to bin 2. No new loads occur at time step 2, so a value of 0 is placed in bin 1.

This process is repeated for the next 2 time steps until bins 1-3 each contain a value of 0, and bin 4 has a value 1.

- Time step 5: no new load occurs at time step 5, so a value of 0 is placed in bin 1 and the other bins are displaced so that bins 1-4 contain a value of 0 and bin 5 contains a value representing a load of 1 kW, or an energy value of 1 kWh. As was stated when the example was defined above, we plan to keep three 1*h*-bins and then aggregate 2, 1*h*-bins into a single 2*h*-bin. As a result, the loads from bins 4 and 5 collapse into a 2*h* load bin with a value of 1/2 kW. Again, the bin represents a duration of 2*h*, but contains 1 kWh of energy, so the average load value is 1/2 kW.
- Time step 6: no new load occurs, so a value of 0 is placed in bin 1 and the other bins are displaced as before.
- Time step 7: no new load occurs, so a value of 0 is placed in bin 1 and the other bins are displaced as before. Bins 4 and 5 are again aggregated into a single bin of duration 2*h*. These bins contained no energy, so the value they represented is 0 kW.

The key questions related to the parameters controlling this method and the subsequent parametric study are:

1. How many aggregation bins should be retained at each level?
2. How much time should bins at each aggregation level represent?

As shown in the above example, a minimum of 3, 1*h*-bins were kept which then collapsed into 2*h* bins. However, for an annual hourly simulation we could just as easily have kept 2, 5, or 10 1*h*-bins which collapse into 3*h*, 5*h*, or 10*h* sized bins. Or just about any other combination of these or other bin sizes. Our objective is to minimize simulation time and maximize accuracy, but it's not currently obvious which combination of parameters will yield this behavior.

The static method developed by Yavuzturk and Spitler (1999) utilized the parameters shown in Table 2.3. At aggregation level 1, a minimum of 192 hourly-bins are kept. At aggregation level 2, the 1-hour bins collapse into 730-hour bins, when possible. The authors tested the minimum hourly history periods parameter of 24, 192, and 730 hours. However, the method was not optimized any further. $N_{b,i}$ represents the number of bins at the i^{th} level.

Table 2.3: Yavuzturk and Spitler (1999) method parameters

| Level | Duration (hr) | Min. $N_{b,i}$ |
|-------|---------------|----------------|
| 1 | 1 | 192 |
| 2 | 730 | N/A |

Liu (2005) developed another variation of the static load aggregation method which is stated to be an improvement on the case developed by Yavuzturk and Spitler (1999). The author referred to the scheme as a “hierarchical” approach and used the following parameters to guide the aggregation process.

- A minimum of 12 hourly-bins are kept for the 12 most recently simulated hours.
- Hourly loads are then aggregated into daily, 24-hour bins. These bins are referred to as “small” bins.
- Five small bins are aggregated into “medium” bins with a minimum of three small bins kept after aggregation. In other words, once eight small bins have been created, the five which are most distant from the current simulation time are aggregated into medium bins to represent a period of 120 hours.
- 73 medium bins are then aggregated into “large” bins which represents 8760 simulation hours, with 40 medium bins to be kept unaggregated. In other words, once 113 medium bins have been created, the 73 which are most distant from the current simulation time are aggregated into a period of 8760 hours.

These are summarized in the simulation case descriptions in Table 2.4.

Table 2.4: Liu (2005) method simulation case descriptions

| Level | Duration (hr) | Min. $N_{b,i}$ |
|-------|---------------|----------------|
| 1 | 1 | 12 |
| 2 | 24 | 3 |
| 3 | 120 | 40 |
| 4 | 8760 | N/A |

The author claims that the case results in generating only 12% of the aggregation bins which results in a 20% reduction in simulation time when compared to the Yavuzturk and Spitler (1999) case.

Bernier et al. (2004) Bernier et al. (2004) also developed another variation on the static aggregation method which was termed the “multiple-load aggregation algorithm” (MLAA). The method uses a GHE model formulation which relies on a cylindrical heat source equation rather than the response factor approach outlined previously. Regardless of this, though, the load aggregation procedure which is described is applicable to the work performed here.

The authors tested several different variations for the bin duration parameter, but settled on the following:

- A minimum of 12 hourly-bins are kept.
- Hourly-bins are aggregated into bins representing 48 hours, termed “daily” bins.
- Daily bins are aggregated into 168 hour “weekly” bins.
- Weekly bins are aggregated into 360 hour “monthly” bins.

Table 2.5: Bernier et al. (2004) original aggregation parameters

| Level | Duration (hr) | $N_{b,i}$ |
|-------|---------------|-----------|
| 1 | 1 | 12 |
| 2 | 48 | Unknown |
| 3 | 168 | Unknown |
| 4 | 360 | N/A |

Something that should be pointed out regarding this work’s testing of the MLAA case is the fact that the aggregation bins specified by the authors do not aggregate

together evenly. As the static method is formulated in this work, the aggregation bin’s durations must be integer combinations of each other. For example, we can take several smaller bins and combine them together to form a larger bin, but we cannot take smaller bins and a fractional bin to form a larger bin. In the case of the MLAA case, 48 is not an integer multiple of 168 so this discrepancy causes a minor implementation issue. From a practical standpoint, it would be possible to combine smaller bins and a fractional bin together, since we would just include the fraction of the bin’s energy which is proportional to the bin fraction we are including. However, this would force us to recompute all subsequent bins, which is an added computational expense. The authors also do not say whether any holding periods were used besides the one mentioned for the hourly loads.

To get around these problems, parameter combinations were created to bracket the intervals specified by the authors. These are specified below in Tables 2.6 and 2.7. Cases 1-4 show the minimum number of bins that will be held unaggregated for each level, and cases a-c show the duration in hours for each bin. All combinations of cases 1-4 and a-c were run in an attempt to bracket the original method.

Table 2.6: Bernier et al. (2004) minimum number of bins, $N_{b,i}$

| Level | 1 | 2 | 3 | 4 |
|-------|----|---|---|-----|
| Case | | | | |
| 1 | 12 | 4 | 3 | N/A |
| 2 | 12 | 4 | 3 | N/A |
| 3 | 12 | 4 | 4 | N/A |
| 4 | 12 | 1 | 1 | N/A |

Table 2.7: Bernier et al. (2004) bin durations (hr)

| Level | 1 | 2 | 3 | 4 |
|-------|---|----|-----|-----|
| Case | | | | |
| a | 1 | 48 | 144 | 432 |
| b | 1 | 48 | 144 | 288 |
| c | 1 | 48 | 144 | 288 |

Fossa and Minchio (2013) later noted some temperature prediction errors for sim-

ulations using the original MLAA method for situations with annual load profiles, of which contained extreme examples where there were no thermal loads for extended periods of time. To improve the method, the authors added a 1440-hour load block to the original method. The authors termed this modification “MLAA17.”

One observable disadvantage of the static method is that it is difficult to store and reuse g-function values once they have been computed. As is seen in Equation 2.4, the g-function is referenced from the current simulation time to the end of the bin for which you are computing. Precomputing and reusing g-functions for the first set of bins is not a problem, but issues arise for subsequent bins. This is because the duration of bins can be any integer multiple of the previous bin’s duration, and each bin level can have any arbitrary number of holding periods. As a result, it becomes difficult to determine beforehand the time intervals for which g-functions will be needed. Therefore, it is easier to simply compute the g-function values as needed at the beginning of each time step rather than attempting to precompute and store them.

An example of this can be seen by referring to Table 2.2. Response factors for bins 1-3 could easily be stored and reused. However, for subsequent bins, the end time of each bin varies at each time step. For example, at time step 4, bin 4 ends at the end of $4h$ time steps. Advancing to time step 5, bin 4 now ends at time step $5h$, thus requiring the g-function be recomputed. Advancing again to time step 6, bin 4 now ends again back at $4h$. This effect cascades up through the list of bins, and with additional bin durations and holding periods it becomes difficult to track. It quickly becomes more efficient to simply recompute the g-function values rather than determining which of all possible combinations of g-functions to store and retrieve.

2.2.2 Dynamic Method

Wentzel (2005) describes another type of load aggregation procedure which differs

from the static method. The author used the method to model a foundation wall using dynamic thermal networks, and not a GHE. Claesson and Javed (2012) later simplified the method and applied it to modeling GHE. The method could be characterized as an Eulerian approach, which in a fluid flow application, tracks the flow through a fixed control volume rather than tracking individual packets or particles of fluid. In our case, we predefine the bins and allow energy to move through the bins. Hence, we term the method “dynamic” since the loads move relative to the aggregation bins. This work has taken the frame of reference to be oriented around the load values, not the aggregation bins. Thus the reasoning for labeling the Yavuzturk and Spitler (1999)-type methods “static” and the Claesson and Javed (2012)-type methods “dynamic.” In the case of the static method, the bins move relative to the current simulation time, but the loads themselves are fixed within the bins, whereas the dynamic method bins are fixed relative to the current simulation time, but the loads move within the bins.

The dynamic method is illustrated in Table 2.8, which is an example taken from Claesson and Javed (2012). However, to summarize the method we can say for each bin at each time step a fraction of the energy is shifted farther into the load history. This fraction is defined by current simulation time step and each bin’s time duration. So, for example, if we have a time step of $1h$, and an individual bin has a duration of $10h$, one-tenth of the load is transitioned out of the bin ($1h/10h = 0.1 = 10\%$) at each time step. If the bin duration were $1h$, all the energy in the bin would be transitioned out of the bin ($1h/1h = 1 = 100\%$) at each time step.

In Table 2.8, the values of the GHE loads for each time step within each bin are represented. Horizontally, the bin durations are given as $1h$ or $2h$, where h represents the length of the time step. For this example, we can assume that the time step, $1h$, is 1 hour. As before, the most recent load is always in the first bin. See the following description:

- Time step 1: a new load with a value of 1 kW occurs. Because the time step is

- 1 hour, the energy represented by this load is 1 kWh which is placed in bin 1.
- Time step 2: bin 1 has a duration of $1h$, and given that the current time step is $1h$, all of the energy from bin 1 will move to bin 2.
 - Time step 3: Bin 2 has a duration of $1h$ and contains 1 kWh of energy. Given the time step, $1h$, all of the energy from bin 2 is moved to bin 3. However, bin 3 has a duration of $2h$, so the load represented by this bin is now $1/2$. Again, energy is conserved but the original pulse of 1 kWh is now spread over a $2h$ time interval.
 - Time steps 4-7: the process described previously is repeated. This results, for example, in Bin 7 containing half the energy of Bin 6 of hour 6, and Bin 6 in hour 7 containing half the energy of Bin 6 in hour 6 and half the energy of Bin 5 from hour 6.

Table 2.8: Dynamic aggregation example

| Bin No. | 1 | 2 | 3 | 4 | 5 | 6 | 7 |
|-----------|-----|-----|------|------|------|------|------|
| Width | h | h | $2h$ | $2h$ | $2h$ | $2h$ | $2h$ |
| Time Step | | | | | | | |
| 1 | 1 | | | | | | |
| 2 | 0 | 1 | | | | | |
| 3 | 0 | 0 | 1/2 | | | | |
| 4 | 0 | 0 | 1/4 | 1/4 | | | |
| 5 | 0 | 0 | 1/8 | 2/8 | 1/8 | | |
| 6 | 0 | 0 | 1/16 | 3/16 | 3/16 | 1/16 | |
| 7 | 0 | 0 | 1/32 | 4/32 | 6/32 | 4/32 | 1/32 |

Because the bin durations are predetermined and are fixed relative to the current simulation time (i.e. in our above example bin 3, for example, will always represents the loads which occurred from 2-4 hours before the current simulation time), the g-function values can be precomputed. This eliminates the need to continuously compute these values at each time step, as was the case with the static method.

However, another issue which arises due to this method is the fact that the method introduces diffusion and dispersion errors. The diffusion errors occur due to the

magnitude of the load values diffusing with time, as is seen with the amplitude of the original value which is decreasing with time. The dispersion errors occur due to the load values dispersing into the GHE history faster than actually occurs by the natural passing of simulation time. To illustrate this, let us consider the previous dynamic method example.

At time step 7, the original load value of 1 kWh is now smeared across 5 different bins. The true value should be $1/2$ and be located within bin 5. However, value at bin 5 is $3/16$. This illustrates the diffusive nature of the method, meaning the amplitudes of the pulses diffuse with time. We can also see that the load value has propagated as far as $12h$ into the load history, since we have non-zero values in bins 6-7. Again, the true value should be $1/2$ and located at bin 5, and as a result of the dispersion, load values are occurring further into the history than should happen naturally. This illustrates the dispersive nature of the method. We expect the hours which are most near to the current simulation time to have the largest effect on the GHE short-term temperature response. This is the reason why the aggregation methods commonly preserve nearly all loads near the most recent simulation time unaggregated. We do not expect hourly load variations from, say, several days before the current simulation time to have a significant effect on the current short-term temperature response. What is important, however, is that energy is conserved.

Regarding the method's implementation, the dynamic method can be characterized using two parameters; the expansion rate of the bin levels, and the number of bins at each level. The number of aggregation levels can be expanded as needed to meet the requirements of the duration of the simulation.

The dynamic method implemented by Claesson and Javed (2012) uses an expansion rate of 2, and 5 bins at each level. The authors also use 16 aggregation levels as this is more than enough to perform a 20-year simulation, though this could be expanded or contracted as needed to fit the simulation time. This example is illustrated

in Table 2.9.

The duration of the bins within each level is indicated in the bin duration column in Table 2.9. Here, the authors determine the duration of bins within each level with the following formula, where t_b is the duration of each bin in hours, r_e is the expansion rate, and i is the level number.

$$t_b = r_e^{i-1} \tag{2.6}$$

Table 2.9: Dynamic method as proposed by Claesson and Javed (2012)

| Level | Level Bin Duration | Simulation Hours | | | | |
|-------|--------------------|------------------|--------|--------|--------|--------|
| | | 1 | 2 | 3 | 4 | 5 |
| 1 | h | 1 | 2 | 3 | 4 | 5 |
| 2 | 2h | 7 | 9 | 11 | 13 | 15 |
| 3 | 4h | 19 | 23 | 27 | 31 | 35 |
| 4 | 8h | 43 | 51 | 59 | 67 | 75 |
| 5 | 16h | 91 | 107 | 123 | 139 | 155 |
| 6 | 32h | 187 | 219 | 251 | 283 | 315 |
| 7 | 64h | 379 | 443 | 507 | 571 | 635 |
| 8 | 128h | 763 | 891 | 1019 | 1147 | 1275 |
| 9 | 256h | 1531 | 1787 | 2043 | 2299 | 2555 |
| 10 | 512h | 3067 | 3579 | 4091 | 4603 | 5115 |
| 11 | 1024h | 6139 | 7163 | 8187 | 9211 | 10235 |
| 12 | 2048h | 12283 | 14331 | 16379 | 18427 | 20475 |
| 13 | 4096h | 24571 | 28667 | 32763 | 36859 | 40955 |
| 14 | 8192h | 49147 | 57339 | 65531 | 73723 | 81915 |
| 15 | 16384h | 98299 | 114683 | 131067 | 147451 | 163835 |
| 16 | 32768h | 196603 | 229371 | 262139 | 294907 | 327675 |

The simulation hours columns indicate the end hour of the GHE load history for which that bin is applicable. Starting at level 1, the first bin (which has a value of 1) will account for the current simulation load. Moving right, next bin will account for the load from 1-2 hours into the GHE load history. This process is repeated until the end of the level. At level 2, the first bin (which has a value of 7) accounts for loads from 5-7 hours into the GHE load history. The next bin accounts for hours 7-9, etc.

2.2.3 Other Methods

Marcotte and Pasquier (2008) apply a FFT algorithm to compute the GHE fluid temperature and then compare that method with a load aggregation method similar to the dynamic method. The authors hold 48 hourly loads unaggregated. Then from there, the approach begins aggregating into 2-hour, 4-hour, 8-hour, etc. bins. The purpose of the paper was to show the advantages of the FFT methods over the load aggregation methods. However, these methods are not suitable for simulations with loads that evolve during the simulation, and which are not known beforehand since this is required by the FFT methods.

Lamarche (2009) and Lamarche and Beauchamp (2007) give a method that does not require load aggregation to solve for the fluid temperature with a GHE. The method relies on the infinite cylinder source solution given by Carslaw and Jaeger (1959). After some mathematical manipulations and assumptions using the Duhamel theorem, the author develops a solution which is independent of the previous loads. Solution of the method, however, requires a Laplace transform inversion. To do this the author uses commercial software and notes that high precision variables (at least 50 digits of precision) are needed to accurately perform the computations.

Other non-load load history dependent schemes have been developed but are not reviewed here. The subject of load aggregation along with g-function models—which is the subject of this paper—are methods which are currently being used in available GHE hourly simulation and sizing tools. As a result, it is important to characterize how the various load aggregation methods behave so current tools can be optimized.

2.3 Methodology

In order to compare the methods, a parametric study was performed by sweeping the input parameters for each method over a wide range of inputs. The input parameters for the static and dynamic methods are described in Section 2.2.

Simulations for all variations of the static and dynamic methods, as well as all aggregation methods referenced previously were simulated for 1, 5, and 10 years using balanced and imbalanced load profiles. The load profiles were generated using EnergyPlus (Crawley et al., 2001) with an input file created by Deru et al. (2011). The balanced load profile simulations have approximately the same energy being rejected to and extracted from the ground during each simulation year. The imbalanced load profile contains loads which reject much more heat to the ground than is extracted over the course of the simulation year. The balanced load profile was generated by simulating the building using the Cincinnati, Ohio USA TMY3 weather file which is provided by DOE (2018). The imbalanced load profile used the Miami, Florida USA TMY3 weather file which is also provided by DOE (2018). The loads data generated by EnergyPlus were for a single, hourly-annual simulation, which yielded 8760 load values. These values were repeated for multi-year simulations and the ground heat exchanger flow rate was fixed at 0.1 kg/s for each time step. g-functions for the borehole were generated using finite line source methods (Cimmino, 2018a).

The simulation input file contained a description of a small, five-zone office building which contained air heating and cooling coils. The system modeled did not contain a simulation of a ground source heat pump. The loads used were taken from the simulation by aggregating the total air-side loads for the building and scaling them proportionally so that the peak load value was appropriate given the borehole being simulated. This resulted in peak cooling or heating loads on the ground heat exchanger of 5 kW. The ground heat exchanger simulated was installed at Oklahoma State University in 1997 and is described in Beier et al. (2018). A plot of the load profiles is given in Figure 2.1. The loads in tabular form are available in a data repository (Mitchell, 2019).

Once each case had been simulated, the simulation data were compared against simulations which did not incorporate load aggregation. The root-mean squared error

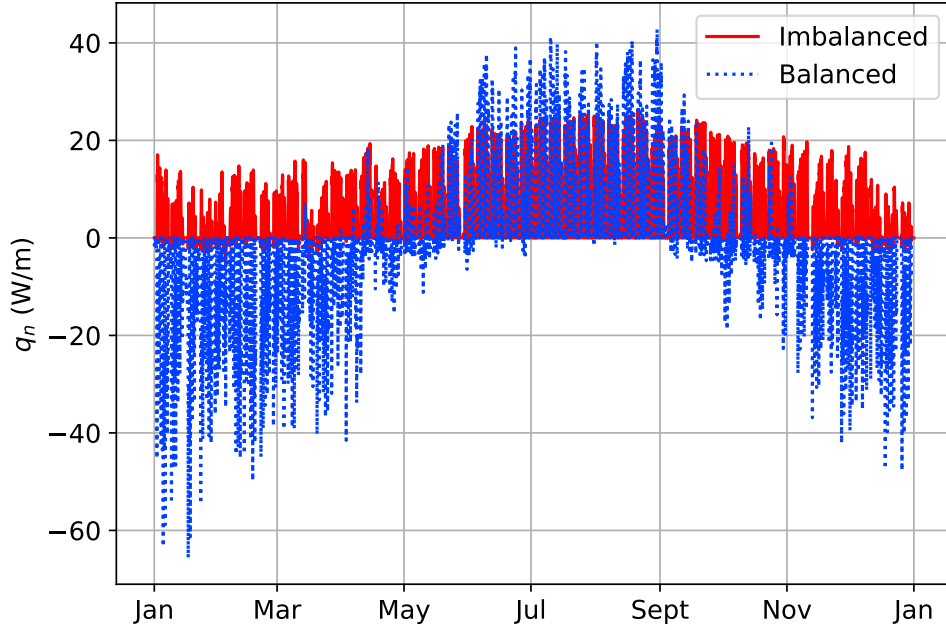


Figure 2.1: Load Profiles

(Equation 2.7) for the borehole mean fluid temperatures (MFT) and the simulation time fraction (SFT) were then computed for each case. Simulation time fraction is the simulation time divided by the simulation time for the respective non-aggregated simulation case.

$$\text{RMSE} = \sqrt{\frac{\sum_{i=1}^n (\hat{y}_i - y_i)^2}{n}} \quad (2.7)$$

All simulations were run at the OSU High Performance Computing Center on the “Cowboy” cluster. The cluster consists of 252 standard compute nodes, each with dual Intel Xeon E5-2620 “Sandy Bridge” hex core 2.0 GHz CPU’s, with 32 GB of 1333 MHz RAM.

The aggregation study and all data analysis were done using the Python programming language. The source code for the project is available here: <https://github.com/mitchute/GLHE>, at code commit SHA 2f6554f85494389530c7c679a1b4cfd67735c23c

2.3.1 Static Method

Besides simulating the previously described cases (Yavuzturk and Spitler 1999, Bernier et al. 2004, Liu 2005), a parametric study was performed for the static method by varying the input parameters of the static method over a wide range. These parameter combinations are shown in Tables 2.10 and 2.11.

Tables 2.10 shows cases a-v, each of which represents a scheme for setting the duration of the bins at each aggregation level. Starting with case “a”, the bins increase at a $2\times$ multiplier, starting from an hourly level of 1 hour, then increasing to 2, 4, 8, etc. Case “b” uses a $3\times$ multiplier, case “c” uses a $4\times$ multiplier; etc. Note that there is no $6\times$ multiplier case. It was not noticed until after all simulations had been completed that this had been omitted. Regardless, the results it would have produced are expected to be bracketed by the other cases.

Table 2.11 shows the minimum number of hourly bins, and the minimum number of the remaining “other” bins which will need to be held before any aggregation can occur. Cases 1-12 show the minimum number of hourly bins, and cases α , β , γ , and δ indicate the minimum number of the remaining bins.

All possible combinations of the parameters outlined were simulated, for a total of 1056 case combinations ($22 \times 12 \times 4$) for the static method parametric study. Note that each of these cases were simulated for 1, 5, and 10-year simulations, and that they were simulated using balanced and imbalanced load profiles.

2.3.2 Dynamic Method

Parameters for the dynamic method parametric study were the expansion rate and number of bins in each level, $N_{b,i}$. Expansion rate was varied from 1.25 to 3.00 at an interval of 0.25. However, a value of $\frac{1+\sqrt{5}}{2} = 1.618\dots$ (golden ratio) was also included. This yields a total of 9 expansion rates. The number of levels, N_L was expanded as needed to fit the simulation runtime requirements.

Table 2.10: Static method parametric study simulation case durations, in hours

| Level | Cases | | | | |
|-------|-------|-------|-------|-------|-------|
| | a | b | c | d | e |
| 1 | 1 | 1 | 1 | 1 | 1 |
| 2 | 2 | 3 | 4 | 5 | 7 |
| 3 | 4 | 9 | 16 | 25 | 49 |
| 4 | 8 | 27 | 64 | 125 | 343 |
| 5 | 16 | 81 | 256 | 625 | 2401 |
| 6 | 32 | 243 | 1024 | 3125 | 16807 |
| 7 | 64 | 729 | 4096 | 15625 | |
| 8 | 128 | 2187 | 16384 | | |
| 9 | 256 | 6561 | | | |
| 10 | 512 | 19683 | | | |
| 11 | 1024 | | | | |
| 12 | 2048 | | | | |
| 13 | 4096 | | | | |
| 14 | 8192 | | | | |
| 15 | 16384 | | | | |

| | f | g | h | i | j |
|---|------|------|-------|-------|-------|
| 1 | 1 | 1 | 1 | 1 | 1 |
| 2 | 8 | 9 | 10 | 11 | 12 |
| 3 | 64 | 81 | 100 | 121 | 144 |
| 4 | 512 | 729 | 1000 | 1331 | 1728 |
| 5 | 4096 | 6561 | 10000 | 14641 | 20736 |

| | k | l | m | n | o | p |
|---|------|------|------|------|------|------|
| 1 | 1 | 1 | 1 | 1 | 1 | 1 |
| 2 | 13 | 14 | 15 | 16 | 17 | 18 |
| 3 | 169 | 196 | 225 | 256 | 289 | 324 |
| 4 | 2197 | 2744 | 3375 | 4096 | 4913 | 5832 |

| | q | r | s | t | u | v |
|---|------|------|------|-------|-------|-------|
| 1 | 1 | 1 | 1 | 1 | 1 | 1 |
| 2 | 19 | 20 | 21 | 22 | 23 | 24 |
| 3 | 361 | 400 | 441 | 484 | 529 | 576 |
| 4 | 6859 | 8000 | 9261 | 10648 | 12167 | 13824 |

Table 2.11: Static method parametric study minimum number of bins

| Case | Min. $N_{b,1}$ | Case | Min. $N_{b,2-n}$ |
|------|----------------|----------|------------------|
| 1 | 4 | α | 4 |
| 2 | 8 | β | 6 |
| 3 | 10 | γ | 8 |
| 4 | 20 | δ | 10 |
| 5 | 30 | | |
| 6 | 40 | | |
| 7 | 50 | | |
| 8 | 60 | | |
| 9 | 70 | | |
| 10 | 80 | | |
| 11 | 90 | | |
| 12 | 100 | | |

The number of bins at each level for the first and last levels were varied from 1-10, and set to the number of levels, N_L . Though every level could have a different number of bins, we limited the study to cases where $N_{b,i}$ was linearly proportional to the number of bins in the first and last aggregation levels. For example, if the starting level has $N_{b,1} = 1$ and the ending level has $N_{b,10} = 10$, and there are 10 aggregation levels, level 5 would have 5 bins, $N_{b,5} = 5$.

To further illustrate, for the example given previously by Claesson and Javed (2012) and shown in Table 2.9, the number of bins per level is 5, $N_{b,i} = 5$, the number of levels is 16, $N_L = 16$, and expansion rate is 2, $r_e = 16$.

These combinations of input parameters resulted in a total of 1089 test combinations ($9 \times 11 \times 11$) for the dynamic method parametric study. As before, each of these combinations were tested for 1, 5, and 10 simulation years, and for the balanced and imbalanced load profiles.

2.4 Results

2.4.1 General Parametric Study Results Analysis

The simulation results for the balanced load profile, 10-year simulation cases can be seen in Figure 2.2. Each symbol represents a test case. It is desirable to have low simulation time fractions and low RMSE of the MFT. Therefore, the closer to the lower left-hand corner of the plot, the more desirable the outcome.

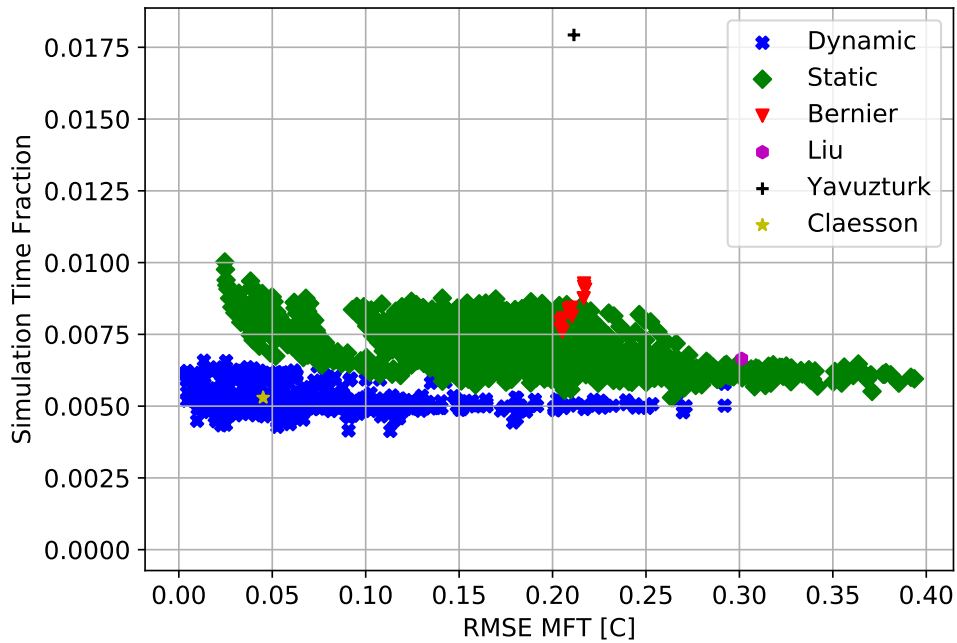


Figure 2.2: Balanced load, 10-year parametric simulation results

Tables 2.12 to 2.14 show the maximum, mean, and minimum statistics for the MFT RMSE and STF for the balanced and imbalanced load profiles. The simulation time fractions are nearly identical for both balanced and imbalanced load profiles, hence only the simulation time fractions for the balanced load profile are shown. As a reminder, implementations by Yavuzturk and Spitler (1999), Bernier et al. (2004), and Liu (2005) are specific cases of the static method, whereas Claesson and Javed (2012) is a specific case of the dynamic method.

As can be seen in Figure 2.2, the dynamic method outperforms the static meth-

Table 2.12: Balanced load cases RMSE [$^{\circ}\text{C}$] $\times 10^3$ statistics

| Sim. Years | Metric | Method | | | | | |
|------------|--------|---------|--------|---------|-------|-----------|----------|
| | | Dynamic | Static | Bernier | Liu | Yavuzturk | Claesson |
| 1 | Max | 304.1 | 409.0 | 248.8 | 198.2 | 207.5 | 45.7 |
| | Mean | 59.5 | 167.7 | 234.4 | | | |
| | Min | 3.0 | 33.3 | 226.3 | | | |
| 5 | Max | 292.3 | 398.6 | 220.3 | 290.1 | 211.0 | 45.3 |
| | Mean | 57.6 | 181.1 | 213.3 | | | |
| | Min | 6.2 | 28.7 | 208.0 | | | |
| 10 | Max | 292.1 | 393.6 | 217.4 | 301.2 | 211.4 | 45.1 |
| | Mean | 57.4 | 185.3 | 210.5 | | | |
| | Min | 4.4 | 24.6 | 204.3 | | | |

Table 2.13: Balanced load cases simulation time fraction $\times 10^3$ statistics

| Sim. Years | Metric | Method | | | | | |
|------------|--------|---------|--------|---------|------|-----------|----------|
| | | Dynamic | Static | Bernier | Liu | Yavuzturk | Claesson |
| 1 | Max | 33.7 | 65.3 | 40.3 | 41.3 | 141.0 | 28.2 |
| | Mean | 27.8 | 45.2 | 39.4 | | | |
| | Min | 24.3 | 32.0 | 38.4 | | | |
| 5 | Max | 11.2 | 17.1 | 13.7 | 12.2 | 33.3 | 8.1 |
| | Mean | 8.0 | 12.0 | 12.4 | | | |
| | Min | 6.3 | 8.6 | 11.7 | | | |
| 10 | Max | 7.0 | 10.0 | 9.3 | 6.6 | 17.9 | 5.3 |
| | Mean | 5.2 | 7.1 | 8.4 | | | |
| | Min | 4.1 | 5.3 | 7.6 | | | |

Table 2.14: Imbalanced load cases RMSE [$^{\circ}\text{C}$] $\times 10^3$ statistics

| Sim. Years | Metric | Method | | | | | |
|------------|--------|---------|--------|---------|-------|-----------|----------|
| | | Dynamic | Static | Bernier | Liu | Yavuzturk | Claesson |
| 1 | Max | 390.4 | 454.9 | 376.3 | 298.6 | 350.3 | 54.7 |
| | Mean | 79.0 | 197.9 | 371.1 | | | |
| | Min | 4.1 | 24.9 | 367.6 | | | |
| 5 | Max | 385.3 | 479.6 | 379.5 | 354.6 | 359.8 | 52.3 |
| | Mean | 75.6 | 206.3 | 374.2 | | | |
| | Min | 4.0 | 26.3 | 370.0 | | | |
| 10 | Max | 367.3 | 468.7 | 380.1 | 365.0 | 361.5 | 50.7 |
| | Mean | 73.9 | 207.9 | 375.1 | | | |
| | Min | 3.5 | 24.6 | 370.8 | | | |

ods with respect to STF for nearly all individual cases simulated. Additionally, the dynamic method average STF is better than the STF for all other methods, for all loads and simulation durations. The dynamic method was also generally better than the other methods in terms of MFT accuracy, though, there is some scatter in this metric across the methods for individual case comparisons. Regardless, the dynamic method MFT RMSE for all load and year simulation cases is better than all other methods.

The static method with the parameters used by Yavuzturk and Spitler (1999) fared worst with respect to STF, though for example the 0.0179 value of STF for the 10 year simulation shown in Table 2.13 represents a 56-fold decrease in computational time compared to the non-aggregated simulation. The parameter combinations used by Bernier et al. (2004) and Liu (2005) were also worse than most of the static cases, and were worse than all dynamic cases. The parameter combinations used by Yavuzturk and Spitler (1999), Bernier et al. (2004) and Liu (2005) all have similar RMSE.

2.4.2 Detailed Dynamic Parametric Study Analysis

The dynamic method implemented by Claesson and Javed (2012) fared quite well when compared to the static cases, and relatively well overall when compared to the other dynamic cases. The dynamic cases showed high accuracy and low runtime fractions in all cases. There were, however, many dynamic simulation cases which yielded better accuracy and better simulation time savings than the original Claesson and Javed (2012) parameters. In an attempt to characterize the parameters that give the best performance, the Pareto frontier values for the dynamic cases for all permutations of load profiles and simulation time were found. The Pareto values for the balanced load profile, 10-year cases are shown in Figure 2.3.

The Pareto optimum is a criterion established by Vilfredo Pareto which asserts

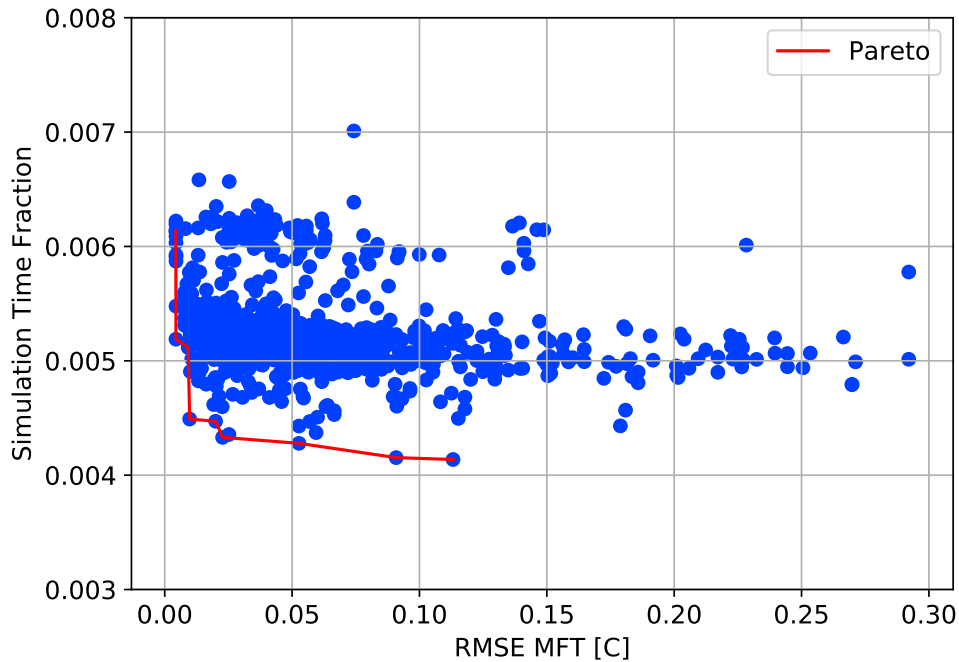


Figure 2.3: Balanced load, 10-year dynamic method simulation cases with Pareto front

that the state of a given system is Pareto optimal, and thus efficient, if and only if there are no feasible alternative states of that system in which at least one objective is better off and no one is worse off (Honderich, 2005). In other words, data which meet the Pareto optimum criterion cannot be moved without making at least one individual objective worse. In our case, the Pareto points identify the parameter combinations which give the maximum accuracy (lowest RMSE) for a given simulation time fraction or the lowest simulation time fraction for a given accuracy.

The Pareto optimum points were identified using the Python “pareto” library (Woodruff and Herman, 2018) which implements the popular Non-dominated Sorting Genetic Algorithm, NSGA-II (Deb et al., 2002). The Pareto data for the balanced and imbalance load profile, 1-, 5-, and 10-year cases have been tabulated and are given in the Appendix in Tables 2.15 to 2.20. Note that the MFT RMSE and the STF values are typically on the order of 10^{-3} . Therefore, to better show the values they have been multiplied by 10^3 for convenience.

Table 2.15: Balanced load, 1-year Pareto data

| RMSE $\times 10^3$ | STF $\times 10^3$ | r_e | N_b | n |
|--------------------|-------------------|-------|-------|-----|
| 3.0 | 31.9 | 1.25 | 28 | 21 |
| 3.1 | 29.2 | 1.25 | 28 | 27 |
| 13.9 | 29.0 | 1.25 | 10 | 25 |
| 14.1 | 28.9 | 1.25 | 10 | 25 |
| 14.4 | 28.4 | 1.25 | 10 | 28 |
| 14.6 | 26.6 | 1.25 | 10 | 29 |
| 14.8 | 25.9 | 1.25 | 10 | 32 |
| 15.7 | 25.7 | 1.25 | 8 | 31 |
| 19.3 | 25.4 | 1.50 | 10 | 18 |
| 24.2 | 25.3 | 1.75 | 10 | 12 |
| 24.4 | 25.3 | 1.50 | 5 | 16 |
| 27.7 | 25.0 | 1.62 | 7 | 15 |
| 36.2 | 24.9 | 1.62 | 8 | 16 |
| 40.5 | 24.7 | 1.75 | 4 | 13 |
| 44.2 | 24.7 | 2.25 | 7 | 9 |
| 52.7 | 24.6 | 1.50 | 3 | 19 |
| 56.5 | 24.6 | 1.50 | 2 | 19 |
| 73.9 | 24.6 | 2.50 | 7 | 10 |
| 84.1 | 24.5 | 3.00 | 6 | 8 |
| 141.7 | 24.3 | 3.00 | 2 | 8 |

Table 2.16: Balanced load, 5-year Pareto data

| RMSE $\times 10^3$ | STF $\times 10^3$ | r_e | N_b | n |
|--------------------|-------------------|-------|-------|-----|
| 6.2 | 10.4 | 1.25 | 35 | 27 |
| 6.4 | 9.6 | 1.25 | 35 | 31 |
| 6.4 | 9.6 | 1.25 | 35 | 31 |
| 6.4 | 9.1 | 1.25 | 35 | 35 |
| 8.9 | 8.7 | 1.50 | 22 | 18 |
| 9.1 | 8.3 | 1.50 | 22 | 20 |
| 9.1 | 7.2 | 1.50 | 22 | 20 |
| 25.1 | 7.1 | 1.62 | 7 | 18 |
| 34.6 | 7.1 | 2.00 | 8 | 13 |
| 36.8 | 7.0 | 1.50 | 3 | 22 |
| 38.1 | 6.9 | 1.75 | 4 | 16 |
| 43.5 | 6.3 | 1.75 | 5 | 18 |
| 52.6 | 6.3 | 1.75 | 4 | 18 |

Table 2.17: Balanced load, 10-year Pareto data

| RMSE $\times 10^3$ | STF $\times 10^3$ | r_e | N_b | n |
|--------------------|-------------------|-------|-------|-----|
| 4.4 | 6.1 | 1.25 | 38 | 30 |
| 4.4 | 5.2 | 1.25 | 38 | 34 |
| 9.2 | 5.1 | 1.25 | 9 | 31 |
| 9.8 | 4.5 | 1.25 | 10 | 41 |
| 20.0 | 4.5 | 1.62 | 10 | 22 |
| 22.7 | 4.3 | 1.75 | 10 | 16 |
| 52.7 | 4.3 | 2.25 | 5 | 13 |
| 90.8 | 4.2 | 2.75 | 3 | 10 |
| 113.2 | 4.1 | 2.75 | 4 | 12 |

Table 2.18: Imbalanced load, 1-year Pareto data

| RMSE $\times 10^3$ | STF $\times 10^3$ | r_e | N_b | n |
|--------------------|-------------------|-------|-------|-----|
| 4.1 | 30.1 | 1.25 | 28 | 21 |
| 7.5 | 29.0 | 1.25 | 10 | 22 |
| 10.5 | 27.3 | 1.25 | 9 | 25 |
| 10.8 | 27.0 | 1.25 | 10 | 26 |
| 16.6 | 26.8 | 1.50 | 10 | 15 |
| 17.1 | 26.8 | 1.50 | 9 | 16 |
| 17.4 | 26.5 | 1.25 | 5 | 28 |
| 19.9 | 26.4 | 1.25 | 4 | 28 |
| 20.4 | 26.0 | 1.50 | 10 | 17 |
| 21.7 | 25.7 | 1.50 | 10 | 17 |
| 39.4 | 25.5 | 1.75 | 8 | 14 |
| 51.6 | 25.5 | 2.00 | 5 | 11 |
| 54.0 | 25.4 | 2.25 | 5 | 9 |
| 63.5 | 25.2 | 1.75 | 3 | 13 |
| 74.3 | 25.1 | 2.25 | 4 | 10 |
| 97.3 | 25.0 | 2.50 | 5 | 10 |

Table 2.19: Imbalanced load, 5-year Pareto data

| RMSE $\times 10^3$ | STF $\times 10^3$ | r_e | N_b | n |
|--------------------|-------------------|-------|-------|-----|
| 4.0 | 12.3 | 1.25 | 35 | 27 |
| 4.4 | 10.9 | 1.25 | 35 | 30 |
| 4.5 | 10.2 | 1.25 | 35 | 31 |
| 4.6 | 10.1 | 1.25 | 35 | 31 |
| 4.8 | 9.9 | 1.25 | 35 | 32 |
| 4.9 | 9.3 | 1.25 | 35 | 33 |
| 5.3 | 9.1 | 1.25 | 35 | 35 |
| 9.2 | 8.6 | 1.50 | 22 | 18 |
| 10.5 | 8.3 | 1.25 | 8 | 33 |
| 12.8 | 8.0 | 1.50 | 22 | 21 |
| 16.6 | 8.0 | 1.62 | 20 | 19 |
| 18.4 | 7.7 | 1.50 | 8 | 20 |
| 18.9 | 7.3 | 1.50 | 7 | 18 |
| 24.0 | 7.2 | 1.50 | 6 | 18 |
| 37.6 | 6.8 | 1.62 | 9 | 21 |
| 90.3 | 6.6 | 1.50 | 3 | 25 |

Table 2.20: Imbalanced load, 10-year Pareto data

| RMSE $\times 10^3$ | STF $\times 10^3$ | r_e | N_b | n |
|--------------------|-------------------|-------|-------|-----|
| 3.5 | 6.2 | 1.25 | 38 | 30 |
| 4.0 | 6.0 | 1.25 | 38 | 34 |
| 4.1 | 6.0 | 1.25 | 38 | 34 |
| 4.2 | 6.0 | 1.25 | 38 | 35 |
| 4.3 | 5.8 | 1.25 | 38 | 35 |
| 4.3 | 5.6 | 1.25 | 38 | 35 |
| 6.8 | 5.5 | 1.25 | 10 | 31 |
| 8.5 | 5.1 | 1.50 | 24 | 21 |
| 9.7 | 5.1 | 1.25 | 9 | 36 |
| 11.3 | 5.0 | 1.25 | 8 | 37 |
| 11.5 | 4.3 | 1.25 | 7 | 36 |
| 23.1 | 4.2 | 1.62 | 10 | 20 |
| 29.4 | 4.1 | 2.00 | 16 | 15 |
| 50.2 | 4.0 | 1.50 | 4 | 25 |
| 99.3 | 3.8 | 3.00 | 4 | 10 |

Analysis of the Pareto data for all simulation cases show that accuracy is increased with smaller expansion rates. For the Pareto data show in the tables, over half of the points in each table have an expansion rate of 1.5 or smaller. We can also see that the Pareto data with the highest accuracy will have a larger number of bins in the first aggregation level. The data show that a significant number of these Pareto simulations have starting and ending level bin numbers of 10 or lower, although, the cases with the highest accuracy generally have a large number of bins in the first aggregation level. The cases with the starting and ending number of bins > 10 are expected to be less frequent due to how the parametric study input parameters were defined.

Figure 2.4 shows the dynamic method balanced load profile, 10-year simulation cases with the data colored by the expansion rate. In the figure, we can see that smaller expansion rates, in general, tend to lead to higher accuracy results. For all cases, the higher expansion-rate simulations tend to be shifted right, whereas the lower expansion-rate simulations tend to be shifted left.

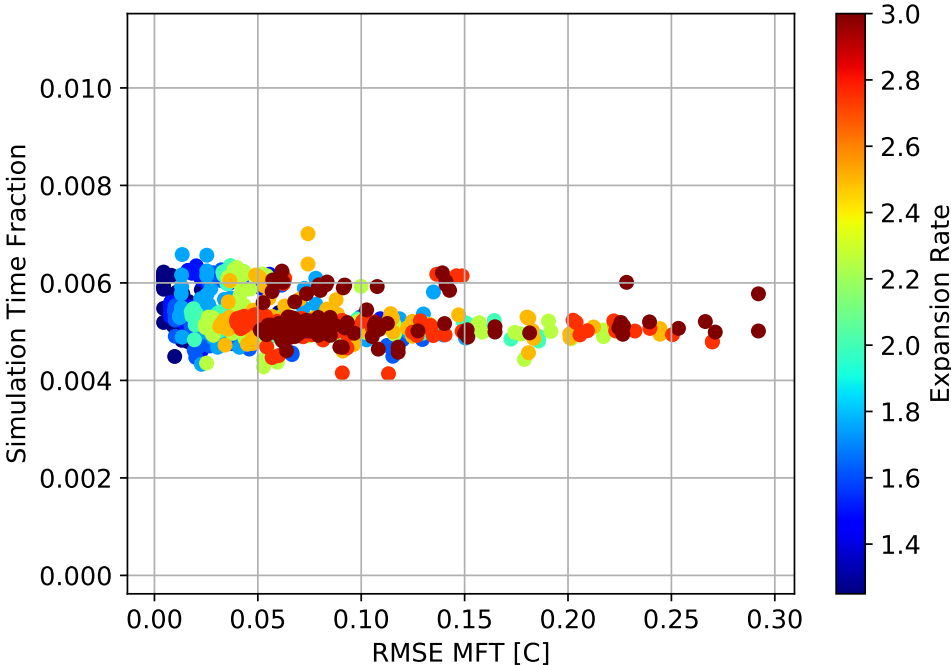


Figure 2.4: Dynamic method balanced load, 10-year cases colored by expansion rate

From this analysis, it appears that the lower expansion-rate simulations give higher accuracy results. Also, based on the analysis of the data from the Pareto simulations for all dynamic test cases, we can see that many of the best simulations have starting and ending number of bins per level of $1 < N_{b,i} \leq 10$. To investigate this, the dynamic cases were again plotted, except this time for only the 1.25, 1.50, 1.62 (golden ratio), and 1.75 expansion rates, with the cases colored by the number of bins in the starting level. Figure 2.5 shows this data for the 10-year balanced simulation cases.

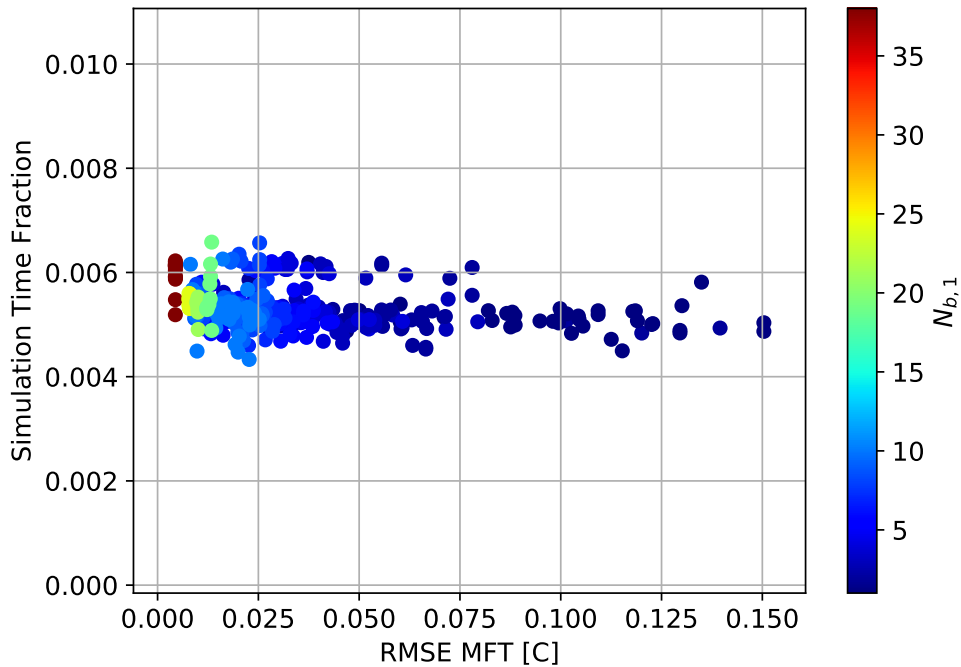


Figure 2.5: Dynamic method balanced load, 10-year cases with selected expansion rates and results colored by the number of bins in the first level.

In Figure 2.5, we can see that the configurations with many bins at the first aggregation level tend to have very high accuracy. We also see that despite this, cases with 10 or fewer bins in the first aggregation level also perform very well. It was expected that configurations with a high number of bins at the first aggregation level would perform well regarding accuracy because loads that occurred most recently in the GHE’s simulation history have the largest effect on the GHE short-term temperature response. This is the reason why all aggregation methods prioritized keeping

the most recent loads unaggregated. However, there is a point of diminishing returns beyond about 10 bins at the first level.

2.4.3 Final Configuration Selection

In order to select a final dynamic method configuration that is generally useful across all parameter variations, simulation times, and load profile combinations, a final selection analysis is performed. To do this, we first wish to determine the effect the aggregation method has on heat pump performance by computing the COP errors relative to the non-aggregated simulations. In other words, given the expected MFT error from the simulations, how much of an effect will this ultimately have on the heat pump model’s energy prediction?

Heat pump performance data were taken from a currently available high-efficiency water-to-air heat pump. The model selected has one-half ton nominal heating and cooling capacity and uses R-410A refrigerant. Tabular performance data for the heat pump are given in Table 2.21 and were taken at constant air- and water-side flow rates.

Table 2.21: Heat pump performance data

| Source Temp. [°C] | COP_c | COP_h |
|-------------------|---------|---------|
| -1.1 | 8.5 | 3.1 |
| 4.4 | 8.1 | 3.5 |
| 10.0 | 7.5 | 4.0 |
| 15.6 | 6.7 | 4.4 |
| 21.1 | 5.7 | 4.8 |
| 26.7 | 4.8 | 5.0 |
| 29.4 | 4.4 | 5.0 |
| 32.2 | 4.0 | 5.0 |
| 37.8 | 3.3 | |
| 43.3 | 2.7 | |
| 48.9 | 2.2 | |

To compute the worst-case effect on performance, the derivative of the COP with respect to source temperature was computed and the maximum value determined.

For cooling operation, this occurred at 21.1 °C and yielded an absolute value of 0.17 COP_c/°C; for heating it occurred at 10 °C and yielded a value of 0.09 COP_h/°C. Derivatives were computed using a simple backward difference. This gave a fractional COP change per degree Celsius in heating or cooling mode of about 0.026 COP/COP-°C. When computing energy consumption, this is equivalent to an error of 2.6%/°C.

Using this analysis, we can then determine how much effect errors in source water temperature predictions will have on the heat pump performance predictions. If we conservatively set the maximum allowable error in heat pump COP at 1%, the corresponding permissible error in source water temperature is about 0.4°C in heating or cooling modes of operation. This means that errors in the source water temperature predictions below this value will result in less than 1% error in the heat pump COP. In Tables 2.15 to 2.20 we can see that for the Pareto data for the corresponding 1-, 5-, and 10-year balanced and imbalanced load profile cases, the maximum MFT RMSE is about 0.14°C, which results in about 0.4% COP error prediction. However, most of the values are well below this. Also remember that the analysis is based on the worst-case scenario, meaning estimates of heat pump COP change as a function of source temperature were picked to be the maximum possible values. As a result, most of the heat pump error due to the aggregation method will be less than this. It is expected that aggregation methods recommended here will have a negligible effect on heat pump performance predictions.

Now that error limits have been assessed, we can continue with picking a configuration which will yield the best results over the entire range of simulation parameter variations. To do this, we consider all the dynamic simulation cases for all parameter variations. One complication in the implementation of the dynamic method is including the capability to change the number of bins at each level. This has not been shown to be necessary to achieve high-performance results. Therefore, only simulation configurations with an equal number of bins per aggregation level will be

considered from here onward. This reduces the number of simulation configurations from over 1000, to 90. From there the RMSE for all configurations were assessed and configurations with RMSE values greater than 0.1°C for any simulation duration or load profile were discarded. After that, the mean RMSE and mean STF for all configurations were computed and a Pareto analysis performed. The results of this are shown in Figure 2.6. The Pareto data are shown in Table 2.22.

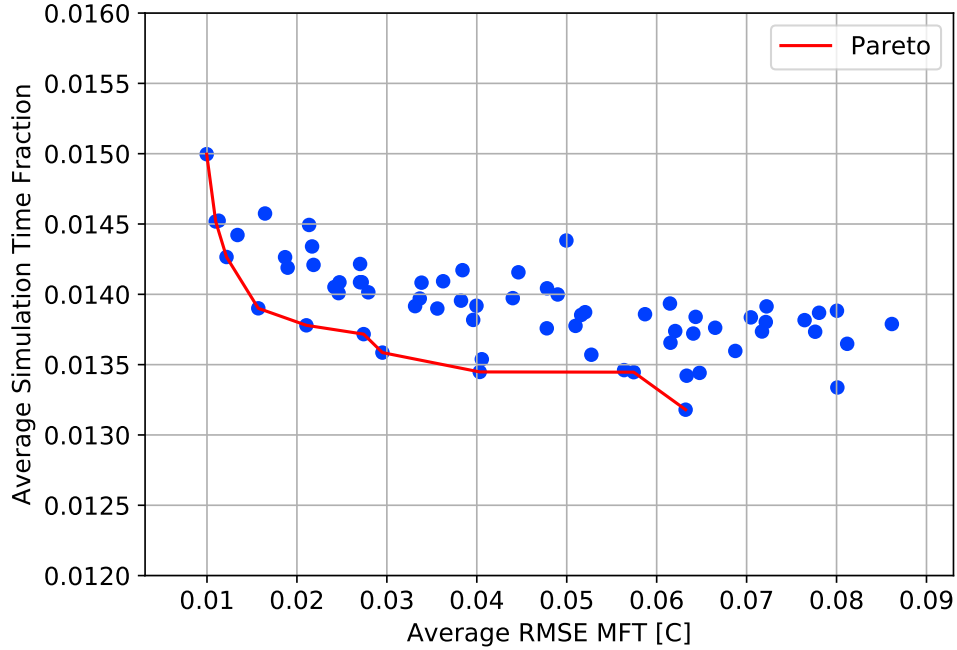


Figure 2.6: Mean STF and RMSE for dynamic configurations with RMSE less than 0.1°C

Table 2.22: Pareto data for dynamic configurations with RMSE less than 0.1°C

| r_e | N_b | RMSE $\times 10^3$ | MBE $\times 10^3$ | STF $\times 10^3$ |
|-------|-------|--------------------|-------------------|-------------------|
| 1.25 | 10 | 9.97 | 2.13 | 15.00 |
| 1.25 | 9 | 10.97 | 2.31 | 14.52 |
| 1.25 | 7 | 12.17 | 3.07 | 14.27 |
| 1.25 | 5 | 15.70 | 4.21 | 13.90 |
| 1.62 | 9 | 21.05 | 5.04 | 13.78 |
| 1.75 | 9 | 27.42 | 5.86 | 13.72 |
| 1.62 | 6 | 29.51 | 7.44 | 13.59 |
| 1.75 | 5 | 40.33 | 10.39 | 13.45 |
| 2.50 | 9 | 57.44 | 10.61 | 13.45 |
| 3.00 | 10 | 63.22 | 11.51 | 13.18 |

Given the results and above analysis, any of the final configurations given will yield very good simulation performance. However, the value at the “knee” of the curve is selected as the final recommended dynamic method configuration, which uses an expansion rate of 1.62, and 9 bins per aggregation level. Some improvement in accuracy or STF can be gained by selecting other combinations; however, these gains are minimal. After further analysis of the recommended configuration, it was also determined that the maximum MFT error with respect to the non-aggregated simulation for all hours was about 0.2°C, which when applied using the heat pump performance data given previously yielded about 0.05% error in predicted heat pump energy usage.

Mean bias error (MBE) for these cases was also computed for the final Pareto cases and is presented in Table 2.22. MBE is expected to be less than RMSE, and any trends in the MBE will indicate whether the errors are biased in one direction or if they tend to be balanced over time. MBE is computed as indicated in Equation 2.8 and the results presented show that the MBE is significantly smaller than the RMSE, suggesting that the aggregation errors tend to balance over time.

$$MBE = \frac{1}{n} \sum T_{f,none} - T_{f,agg} \quad (2.8)$$

Comparing the method with the recommended parameters to the case by given by Claesson and Javed, the recommended parameter results for the balanced and imbalance load profile, for the 1-, 5- and 10-year simulations resulted in an RMSE reduction from 0.0489°C to 0.02105°C. Of course, these values are already quite low, but do result in an RMSE reduction of 56.9% and slight reduction of STF by 0.5%. It should be noted that due to natural variations in the computer hardware used for the simulations, some minor runtime variations are expected. When compared to the static method cases, and many other dynamic method cases, the current recommendation is expected to produce STF improvements while maintaining high accuracy

results.

The above results were computed for a single borehole case. Single boreholes tend to show less long-term temperature change than densely packed large bore fields. As another check of the recommended parameters, the dynamic method with the recommended parameters was used to simulate a 10×10 borehole field set at 6 m spacing with the imbalanced load profile for 1-, 5- and 10-year simulations. All other parameters for the borehole are the same as were described previously for the other simulation cases. However, in order to keep the GHE operating in the same temperature range as the single borehole case (i.e. maximum heat pump entering fluid temperature around 40°C), the loads per unit length were scaled to 70% of those for the single boreholes. Highly imbalanced loads with a large, densely backed borehole field will result in an upward trend in return fluid temperature over time. As a result, the aggregation errors for these cases will be amplified over time.

The RMSE results for these cases are shown in Table 2.23, and the MBE results are shown in Table 2.24. STF values are not presented but are similar to the values for the respective previous single borehole cases, as is expected.

Table 2.23: 10×10 GHE and single BH RMSE [$^{\circ}\text{C}$] results

| Single BH | 10 x 10 BH | |
|------------|------------|--------|
| RMSE 1-yr | 0.0120 | 0.0622 |
| RMSE 5-yr | 0.0114 | 0.1360 |
| RMSE 10-yr | 0.0109 | 0.1432 |

Table 2.24: 10×10 GHE and single BH MBE [$^{\circ}\text{C}$] results

| Single BH | 10 x 10 BH | |
|-----------|------------|--------|
| MBE 1-yr | 0.0073 | 0.0500 |
| MBE 5-yr | 0.0062 | 0.1261 |
| MBE 10-yr | 0.0047 | 0.1234 |

From the results, we can see that the RMSE and MBE remain small for densely packed borehole fields with highly imbalanced loads. The MBE for the 5-yr case corresponds to a maximum error in predicted heat pump energy consumption of

about 0.3%. Therefore, the recommended aggregation method and parameters given above are expected to perform well for all GHE configurations and simulation duration combinations.

Another check that is performed is by comparing the recommended case against the test case demonstrated by Fossa and Minchio (2013). This is an extreme case where the load is held constant for 4000 hours, then set to zero while still flowing circulating fluid for another 4000 hours. Using the borehole given previously, the normalized load is set to 20 W/m while flowing circulating fluid at 0.1 kg/s. The result is shown in Figure 2.7.

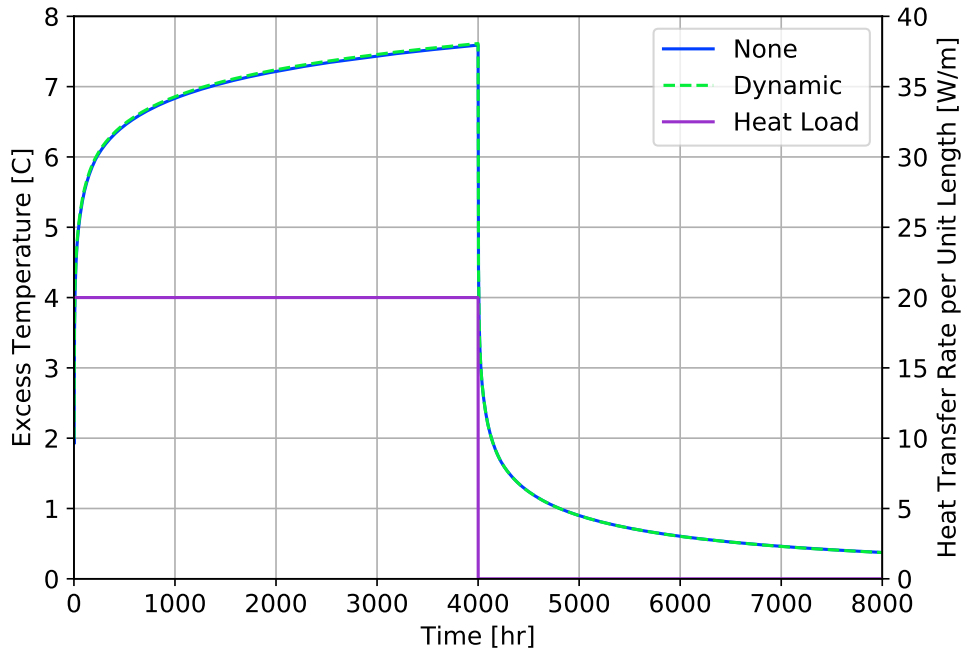


Figure 2.7: Extended duration loading-unloading test results

In the figure, the recommended dynamic method compares very well against the non-aggregated case with a maximum error of 0.07°C. Static methods are not compared here, but were shown by Fossa and Minchio (2013) to have maximum errors of about 0.55°C and 0.15°C for the MLAA and MLAA-17 methods, respectively. Arguably, heat pump entering fluid temperatures are of limited interest for hours when there is no load (i.e. the heat pumps are off), but the recommended dynamic method

performs quite well.

2.5 Conclusions and Recommendations

This paper has described a large parametric study that was performed to investigate different load aggregation methods for response factor type GHE models. The simulations performed and subsequent analysis have shown that the dynamic method described by Claesson and Javed (2012) gave significant reductions in simulation time compared to the static method and equivalent or better accuracy. However, using the parametric study, we found combinations of parameters that give even better results than the parameters utilized by Claesson and Javed. Compared to the Claesson and Javed parameters, the best parameters (expansion rate of 1.62 and 9 bins per aggregation level) give a further 57% reduction in MFT RMSE error with essentially equivalent simulation runtime. The improvement in computational speed varies with the length of the simulation, but taking the case of a 10-year simulation, the mean simulation time for all dynamic cases is 27% lower than the mean simulation time for all static cases, and 71% lower than the simulation time for the original Yavuzturk and Spitler scheme.

Investigation of the dynamic load aggregation method parameters showed that:

1. Smaller expansion rates tend to yield higher accuracy results.
2. A higher number of bins in the first aggregation level tends to yield higher accuracy results, although very good accuracy can be achieved with less than 10 bins per aggregation level. It is also not necessary to vary the number of bins per aggregation level to achieve high accuracy, low-runtime simulations.

Performance of the dynamic load aggregation method with the recommended parameters (expansion rate of 1.62 and 9 bins per aggregation level) was further investigated for a worst-case scenario – a densely packed 100-borehole ground heat exchanger

with an imbalanced load profile. For five- and ten-year simulations, the MBE in fluid temperature is a little less than 0.13°C , which will result in an error of less than 0.3% in the prediction of the heat pump energy consumption. At the same-time, on average a 73-fold reduction in simulation time compared to a non-aggregated simulation is achieved, which is similar to the reduction achieved with the Claesson and Javed (2012) parameters.

CHAPTER III

AN ENHANCED VERTICAL GROUND HEAT EXCHANGER MODEL FOR WHOLE BUILDING ENERGY SIMULATION

3.1 Introduction

Whole-building energy simulation (WBES) programs such as EnergyPlus (Crawley et al., 2001), and TRNSYS (Klein et al., 2016) have equipment-loop simulation algorithms that pass component¹ entering and exiting conditions² flow-wise from upstream components to down-stream components. These components are generally connected in a loop so that every component on the loop is in some way connected every other component on the loop. Equipment which is active at any given time step may be controlled by an individual controller, or by a larger control algorithm which specifies control for the entire system. These components may also make requests to other components to request specific performance. For example, a chiller model which has a minimum required flow rate may require that all other components on the loop run at its minimum flow rate, even though they could be operated at a lower flow rate.

Passive equipment, on the other hand, simply operates by providing what it can at the current given conditions. For GHE, the models are only expected to be passed entering conditions, which in this case is the circulating fluid's temperature and mass flow rate. As is expected in the real-world, the GHE is only going to give whatever performance it can physically deliver, regardless what the other components on the

¹e.g. pumps, boilers, chillers, heat exchangers, etc.

²e.g. flow rates, temperatures, humidity ratios, etc.

loop require for successful operation. The objective of this study is to develop a GHE model which behaves in a similar, passive manner, and also to develop it for use in WBES environments. Some of the constraints associated with that are given below.

First, it is obviously expected that the the model which is developed be accurate and produce physically realistic results. Some modeling assumptions may be necessary to meet secondary needs, such as simulation time. However, regardless of that, the models should still give a result that is as accurate as possible. In addition to that, often times WBES simulation operate at non-uniform time steps, so the models should also accurately simulate GHE behavior at short and long time steps.

Second, the models developed should simulate GHE behavior as quickly and efficiently as possible. WBES simulations are often run on personal computers, such as laptops or desktop computers. These programs also are generally not so sophisticated so as to employ parallel- or multi-processing methods. Simulations are often run on a single computational process, which results in each model or sub-model within a WBES simulation to be run in order, concurrently. Therefore, adding model complexity which significantly increases simulation time should not be done except when necessary. Beyond this, modelers often use WBES to perform parametric analysis of designs, so any increase in simulation time has the potential to quickly amplify the total simulation time for any parametric study performed. This has the potential to become a challenge for designers who do not have access to a computer cluster.

Third, the models should be formulated so they can operate within a WBES environment. This means that the models should be formulated so that the boundary conditions for the model can be clearly defined by the flow-wise upstream component and the external environment. For GHE, this signifies that the GHE outlet fluid temperature can be computed directly from the inlet fluid's temperature and mass flow rate, and by other user-defined or environmental parameters. GHE loads are not expected to be known before hand.

Fourth, the models developed should not rely on libraries, software, or other resources that are not freely available or which must exist external to the simulation environment. Historical WBES GHE models have relied on third-party libraries or software tools to provide input data for the simulation. This creates an additional burden on the modeler, and as a result, the models developed here must be able to operate in a standalone manner.

3.2 Literature Review

A full literature of materials relevant to this topic has been given in Chapter 1; however, the topics of ground heat exchanger modeling and response factor generation methods are of primary importance. Each method and modeling technique has its own unique advantages and disadvantages, as is typical. However, these are not discussed again here.

3.3 Methodology

A number of GHE modeling methodologies have been reviewed and discussed in Section 1.2. These model types are: analytical, response factor, TRCM, and direct numerical. Of these, the only the response factor models are suitable for WBES applications due to their computational efficiency. This section outlines the development of an enhanced response factor model and discusses how it is used in WBES.

3.3.1 Enhanced Response Factor Model

Response factor models have been developed and used in WBES previously (Fisher et al., 2006). This model, which is based on the original formulation by Eskilson (1987); Claesson and Eskilson (1988) has functioned well; however as noted previously, it has trouble simulating short time steps, which are time steps which approach or are shorter than the GHE circulating fluid transit time. So called “short time step”

response factors have been developed (Yavuzturk and Spitler, 1999; Xu and Spitler, 2006; Brussieux and Bernier, 2018) which extend these limits, but non-physical behavior can still occur.

The original response factor model is given in Equation 3.1 where the GHE load is used to compute the borehole wall temperature. However, most of the time computation of the borehole wall temperature is not useful for WBES, so the GHE mean fluid temperature is computed through a steady-state resistance value, as seen in Equation 3.2. The g-function values, g , are assumed to be computed at the appropriate time and GHE configuration as seen in Equation 3.3, where t_n represents the simulation time of the current time step.

$$T_b = T_s + \sum_{i=1}^n \frac{q_i - q_{i-1}}{2\pi k_s} \cdot g \quad (3.1)$$

$$T_f = T_b + q_n R_b \quad (3.2)$$

$$g = g\left(\frac{t_n - t_{i-1}}{t_s}, r_b/H, B/H, D/H\right) \quad (3.3)$$

As presented above, the model is not suited for WBES since this model requires the GHE load as an input parameter. However, this equation can be reformulated after assuming a relationship between the mean fluid temperature and the GHE inlet and outlet temperatures, and after assuming that the fluid heat transfer rate, q_f , and the borehole wall heat transfer rate, q_b , are equal³. A simple borehole schematic indicating the location of q_f and q_b is shown in Figure 3.1. A full derivation of this model has been given in Appendix A.

Response factor models are computationally efficient which is a significant consideration for WBES GHE modeling; however, the models do not perform well when high

³This is the cause of the non-physical behavior of the model.

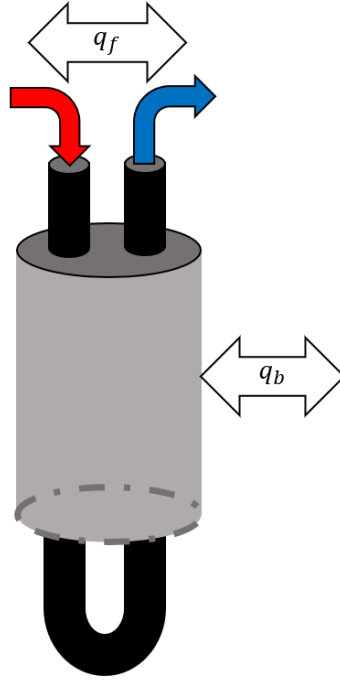


Figure 3.1: Single U-tube borehole.

loads are applied suddenly and when simulation time steps are short. This was shown previously in Chapter 1. Going beyond the short time step methods, several authors have modified the historical response factor model given by Claesson and Eskilson to improve the short-term, dynamic accuracy of the model. These are described here.

Loveridge and Powrie (2013) developed an addition to the original response factor model formulation for modeling concrete pile heat exchangers. The original model was modified by adding a “concrete response function,” g_c , to account for the transient response of the pile heat exchanger. The concrete response function is multiplied by the concrete resistance, R_c , which is analogous to the grout resistance for borehole heat exchangers. The pipe resistance term, R_p , is also pulled out separately and multiplied by the current heat load, instead of the borehole resistance as in the historical response factor model. This is shown Equation 3.4.

$$T_f = T_s + \sum_{i=1}^n \frac{q_i - q_{i-1}}{2\pi k_s} \cdot g + R_c \sum_{i=1}^n (q_i - q_{i-1}) \cdot g_c + q_n R_p \quad (3.4)$$

To be clear, the heat transfer rate applied above is the fluid heat transfer rate, q_f , not the borehole wall (or pile wall) heat transfer rate. Also, it appears that the reason behind decoupling the concrete resistance from the pipe resistance is to allow for added flexibility to account for varying changes in pipe thermal resistance. The concrete resistance is expected to be constant, whereas the pipe resistance will change with changes to the temperature of the circulating fluid and flow rates, so separating the concrete and pipe resistance is useful. Pipe thermal resistance is defined in Equation 3.5.

$$R_p = R_{p,i,conv} + P_{p,cond} \quad (3.5)$$

Pipe internal convection and pipe wall conduction resistances are defined in Equations 3.6 and 3.7, respectively. Nu is the Nusselt number computed based on the circulating fluid properties, flow rate, etc. For straight, smooth pipe with turbulent flow the Gnielinski (1976) correlation is often used along with the friction factor relation for smooth pipe by Petukhov (1970).

$$R_{p,i,conv} = \frac{1}{\pi Nu_{i,conv} k_f} \quad (3.6)$$

$$R_{p,cond} = \frac{\ln(d_{p,o}/d_{p,i})}{2\pi k_p} \quad (3.7)$$

The method developed was successfully used to model pile heat exchangers with hourly loads; however, the method was not used for sub-hourly loads. The method was later used by Alberdi-Pagola (2018) and Alberdi-Pagola et al. (2018); however, these studies also appear to be limited to hourly time steps.

Pile heat exchangers are expected to be relatively short in length when compared to vertical borehole heat exchangers. As a result, the transit time of the circulating fluid from inlet to outlet is also expected to be lower. Also, because sub-hourly time

steps are not expected, the above model is expected to perform well under these conditions. However, if the simulation time step approaches the transit time, the model is expected to have trouble predicting the short term dynamic response. This notwithstanding, the approach shows promise for the current application.

Others have directly computed g-functions for the purpose of directly predicting the GHE exiting fluid temperature. Dusseault and Pasquier (2018) briefly mentions the method, but a full derivation is given by Pasquier et al. (2018). The approach provides a way to utilize the Eskilson-type g-functions and combine them with the short time step g-functions for directly computing the fluid temperature. To compute these entering fluid temperature g-functions a relatively complicated TRCM is utilized (Pasquier and Marcotte, 2012, 2014). As described in Section 1.2.3, directly simulating GHE using TRCM may not be fast enough for WBES. However, this approach only uses the TRCM to generate entering fluid temperature g-functions, so that may be an acceptable approach. One issue that should be given careful consideration is the complexity and computation speed of the TRCM since the entering fluid temperature g-functions need recomputed at each flow change. In addition, the process of recombining the long time step and entering fluid temperature g-functions would need to re-occur at each flow change as well, so this potentially could result in an added computation.

The approach adopted in this work may be considered a blend between the approach by Loveridge and Powrie (2013) and Pasquier et al. (2018). The proposed model is given in Equation 3.8.

$$T_{out} = T_s + \sum_{i=1}^n \frac{q_i - q_{i-1}}{2\pi k_s} \cdot g + R_b \sum_{i=1}^n (q_i - q_{i-1}) \cdot g_b \quad (3.8)$$

In this formulation, the GHE exiting fluid temperature is computed directly by modifying the historical response factor model (Equation 3.2) with the addition of so called “exiting fluid temperature” (ExFT) response factors (or “g-functions”). These

ExFT response factors are computed to determine the temperature difference of the GHE exiting fluid temperature from the borehole wall temperature. As a result, the model can be thought of as two individual parts, which are given in Equations 3.9 and 3.10.

$$T_b - T_s = \sum_{i=1}^n \frac{q_i - q_{i-1}}{2\pi k_s} \cdot g \quad (3.9)$$

$$T_{out} - T_b = R_b \sum_{i=1}^n (q_i - q_{i-1}) \cdot g_b \quad (3.10)$$

The first part comes from the historical response factor model. By applying this equation, the GHE borehole wall temperature difference from the soil temperature can be computed. The second part is the new formulation which computes the GHE exiting fluid temperature difference from the GHE borehole wall temperature.

Again for clarity, the heat transfer rate applied here is the calorimetric fluid heat transfer rate as calculated from the inlet and outlet temperatures, and flow rate of the GHE. This is seen in Equation 3.11, where T_{in} is the GHE entering fluid temperature and T_{out} is the GHE exiting fluid temperature.

$$q_f = \frac{\dot{m}_f c_{p,f}}{H_{tot}} (T_{in} - T_{out}) \quad (3.11)$$

There are several reasons for formulating the model as shown above. These will be discussed here.

- A significant amount of effort has been expended to understand and improve the original response factor model. Since its publication, researchers have performed many studies which enhance understanding of the methods and improve on the original work. This work similarly builds on the original model, about which much is already known and which has already been widely adopted.
- Because the formulation builds on the historical response factor model, software

or other programs that already have this model implemented can more easily make modifications to incorporate the enhancements. This simplifies adoption of the model in WBES environments.

- Again, because the formulation builds on the historical response factor model, methods for generating standard borehole wall temperature g-functions are still applicable. As are load aggregation procedures which are critical to maintaining low simulation times.
- By clearly defining the heat transfer rate applied in this model as the fluid's heat transfer rate, the domain inside the borehole and the domain between the borehole wall and the far-field soil temperature can be coupled together easily through two separate response factor computations. This more easily allows the transient effects to be handled, even down to time steps below the transit time of the GHE circulation fluid.

Additional details about how the original and ExFT g-functions are developed, and how the model is used in WBES are given next.

3.3.2 Model Reformulation for WBES Usage

In order for the model to be applied in WBES, the model needs to be formulated from known quantities. In this case, we wish to pass an entering fluid temperature and mass flow rate to the GHE model, and have it compute and return the exiting fluid temperature.

Starting with Equation 3.8, we will let Equation 3.12 apply so the current model becomes as shown in Equation 3.13.

$$c_0 = \frac{1}{2\pi k_s} \tag{3.12}$$

$$T_{out} = T_s + c_0 \sum_{i=1}^n (q_i - q_{i-1}) \cdot g + R_b \sum_{i=1}^n (q_i - q_{i-1}) \cdot g_b \quad (3.13)$$

To be clear, in response factor models the multiplication of the heat rate differences by the g-function values is a convolution operation. For example, if three time steps have occurred, the summation-convolution operation would be as follows:

$$\begin{aligned} \sum_{i=1}^3 (q_i - q_{i-1}) \cdot g &= (q_3 - q_2) g \left(\frac{t_3 - t_2}{t_s} \right) \\ &+ (q_2 - q_1) g \left(\frac{t_3 - t_1}{t_s} \right) \\ &+ (q_1 - q_0) g \left(\frac{t_3 - t_0}{t_s} \right) \end{aligned} \quad (3.14)$$

Next, because the current heat load is not known, it is deconvolved from the response factor summations.

$$\begin{aligned} T_{out} &= T_s + c_0 (q_n - q_{n-1}) \cdot g_n + c_0 \sum_{i=1}^{n-1} (q_i - q_{i-1}) \cdot g \\ &+ R_b (q_n - q_{n-1}) \cdot g_{b,n} + R_b \sum_{i=1}^{n-1} (q_i - q_{i-1}) \cdot g_b \end{aligned} \quad (3.15)$$

For simplification, we will let the g-function values for the current heat load be noted as shown in Equations 3.16 and 3.17.

$$g_n = g \left(\frac{t_n - t_{n-1}}{t_s} \right) \quad (3.16)$$

$$g_{b,n} = g_b \left(\frac{t_n - t_{n-1}}{t_s} \right) \quad (3.17)$$

From there, the historical terms are gathered together in Equation 3.18, which

then leaves Equation 3.19.

$$c_1 = c_0 \sum_{i=1}^{n-1} (q_i - q_{i-1}) \cdot g + R_b \sum_{i=1}^{n-1} (q_i - q_{i-1}) \cdot g_b \quad (3.18)$$

$$T_{out} = T_s + c_0 (q_n - q_{n-1}) \cdot g_n + R_b (q_n - q_{n-1}) \cdot g_{b,n} + c_1 \quad (3.19)$$

After this, we apply another replacement to simplify the notation (Equation 3.20), which then leaves Equation 3.21 after the current heat transfer rate, q_n , and the previous time step heat transfer rate, q_{n-1} are gathered together.

$$c_2 = c_0 g_n + R_b g_{b,n} \quad (3.20)$$

$$T_{out} = T_s + c_2 q_n - c_2 q_{n-1} + c_1 \quad (3.21)$$

Since we wish to clearly define the model in terms of the fluid heat transfer rate, Equation 3.11, is again introduced in Equation 3.22, after another simplification is applied in Equation 3.23.

$$q_f = c_3 (T_{in} - T_{out}) \quad (3.22)$$

$$c_3 = \frac{\dot{m}_f c_{p,f}}{H_{tot}} \quad (3.23)$$

After Equation 3.22 is substituted into Equation 3.21, and after some algebraic manipulation, we arrive at the final solution in Equation 3.24.

$$T_{out} = \frac{T_s + c_2 c_3 T_{in} - c_2 q_{n-1} + c_1}{1 + c_2 c_3} \quad (3.24)$$

The model is now cast in terms of known quantities. The question remains,

though, regarding how the g-function values will be computed. To do this, a simplified dynamic borehole model has been developed. This will be discussed next, then computation of the g-function values will be discussed.

3.3.3 Dynamic Borehole Model

As discussed previously, this model can be considered a blend between the approaches outlined by Loveridge and Powrie (2013) and Pasquier et al. (2018). In the case of the work on pile heat exchangers, the authors used a detailed numerical model to compute the transient response (Loveridge, 2012); in the case of the borehole heat exchanger, a detailed TRCM was used to determine the short-term, dynamic response (Pasquier and Marcotte, 2012, 2014). A similar approach will be taken here; however, since computation time is so important, a fast solution is desired.

To do this, a simple dynamic borehole model has been developed which will be used to compute the ExFT g-functions. The model is composed of two simple, 1D dynamic pipe models for simulating the transit delays, and a simple four-node TRCM for simulating heat transfer within the borehole. This is seen in Figure 3.2

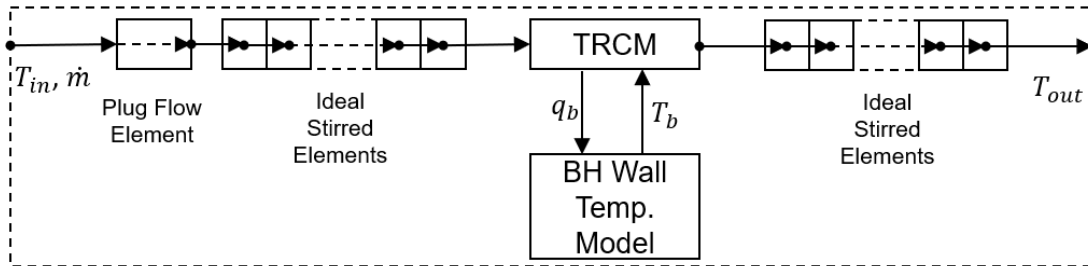


Figure 3.2: Dynamic model borehole schematic

3.3.3.1 Simple Borehole TRCM

A schematic of one segment of the TRCM borehole is shown in Figure 3.3. The model is a simple, five-node model. For comparison, the model used by Pasquier and Marcotte (2014) has 16 nodes per segment.

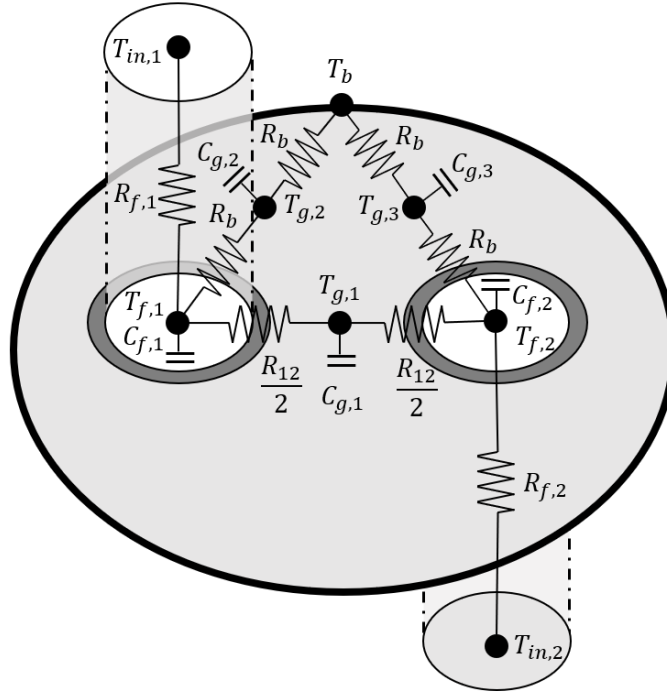


Figure 3.3: Simple TRCM

The resistance values are set using the 1st-order approximation of multipole method (Bennet et al., 1987; Claesson, 2011; Claesson and Hellström, 2011), where R_b is the borehole thermal resistance and R_{12} is the direct-coupling resistance. Javed and Spitler (2017) discuss the accuracy of these methods and note that in most situations, the 1st-order approximation is accurate to within 1%.

Equations for computing R_b have been given in Javed and Spitler (2016) and Javed and Spitler (2017), and will not be repeated here. However, the relations for the direct-coupling resistance using the multipole method are not given, so they have been derived from the Delta-circuit resistance network and given in Equation 3.25 in terms of the borehole resistance and the total internal borehole resistance, R_a . Both of which can be computed directly from the multipole method. Fluid resistance in the flow direction is computed as shown Equation 3.26

$$R_{12} = \frac{4R_a \cdot R_b}{4R_b - R_a} \quad (3.25)$$

$$R_f = \frac{1}{\dot{m}_f c_{p,f}} \quad (3.26)$$

Equations for computing the temperature of each of the temperature nodes from the borehole segment model are given below.

$$C_{f,1} \frac{dT_{f,1}}{dt} = \frac{T_{in,1} - T_{f,1}}{R_{f,1}} + \frac{T_{g,1} - T_{f,1}}{R_{12}/2} dz + \frac{T_{g,2} - T_{f,1}}{R_b} dz \quad (3.27)$$

$$C_{f,2} \frac{dT_{f,2}}{dt} = \frac{T_{in,2} - T_{f,2}}{R_{f,2}} + \frac{T_{g,1} - T_{f,2}}{R_{12}/2} dz + \frac{T_{g,3} - T_{f,2}}{R_b} dz \quad (3.28)$$

$$C_{g,1} \frac{dT_{g,1}}{dt} = \frac{T_{f,1} - T_{g,1}}{R_{12}/2} dz + \frac{T_{f,2} - T_{g,1}}{R_{12}/2} dz \quad (3.29)$$

$$C_{g,2} \frac{dT_{g,2}}{dt} = \frac{T_{f,1} - T_{g,2}}{R_b} dz + \frac{T_b - T_{g,2}}{R_b} dz \quad (3.30)$$

$$C_{g,3} \frac{dT_{g,3}}{dt} = \frac{T_{f,2} - T_{g,3}}{R_b} dz + \frac{T_b - T_{g,3}}{R_b} dz \quad (3.31)$$

The thermal capacity for each node is set from the product of their respective heat capacity and volume. This is shown below for the fluid capacity elements, assuming equivalent pipe sizes for both pipes in the segment.

$$C_{f,1} = \rho_f c_{p,f} V_{f,1} \quad (3.32)$$

$$C_{f,2} = C_{f,1} \quad (3.33)$$

The grout capacity nodes are slightly different since it is difficult to determine what fraction of the total volume grout should be associated with each node. Therefore, this fractional value is included in the grout capacity nodes and will be discussed later.

Total grout volume can be determined from determining the total volume inside of the borehole and subtracting the total pipe volume.

$$C_{g,1} = f_g \rho_g c_{p,g} V_g \quad (3.34)$$

$$C_{g,2} = C_{g,3} = \frac{(1 - f_g) \rho_g c_{p,g} V_g}{2} \quad (3.35)$$

Equations 3.27 through 3.31 are solved together simultaneously using a Runge-Kutta 4-5 time integration scheme (Moin, 2010). Model boundary conditions are the inlet temperatures and mass flow rates for each leg of the U-tube segment, and the borehole wall temperature. All node temperatures are initialized to the undisturbed ground temperature.

The borehole wall boundary temperature is updated each time step using the response factor calculation seen in Equation 3.1. g-function response factors are computed using pygfunction library (Cimmino, 2018c) which uses finite-line source methods for long time step g-functions (Cimmino, 2018a). Short time step g-functions are computed using the 1D, radial finite volume model developed by Xu and Spitler (2006)⁴. However, instead of using the model to evaluate the fluid temperature rise and then subtract off the borehole resistance—which effectively results in a negative borehole wall temperature response at short time steps—the actual borehole wall temperature rise is evaluated and then the short time step g-functions are computed. Additional details regarding this will be given in a subsequent section.

3.3.3.2 Dynamic Pipe Model

In order to simulate the transit delay effects within the borehole, a dynamic pipe model is used. The model was originally developed by Bischoff and Levenspiel (1962),

⁴To be clear, these are the short time step g-functions used for computing borehole wall temperature.

and later improved by Skoglund and Dejmek (2007). Rees (2015) applied the model in a fashion similar to the current application, except that the author used a 2D radial-angular finite volume model to compute the heat transfer within the borehole. The model applies a single plug-flow element that tracks the history of the pipe inlet temperatures, then the temperature nodes along the pipe are mixed together in ideally stirred tank elements. Skoglund and Dejmek (2007) recommends that 16 elements is sufficient to achieve a good balance between accuracy and performance. In the model applied here, only the plug-flow time delay is applied to the inlet pipe. The outlet pipe directly mixes the element temperatures together to determine the dynamic temperature response. Computing the temperature of the stirred elements can be accomplished with a tri-diagonal matrix inversion solution, often referred to as the Thomas Algorithm (Moin, 2010). This convenient formulation makes the computations execute quickly.

All details regarding model implementation are given in the previous references, and are not repeated here.

Figures 3.4 and 3.5 show the non-dimensional pipe response vs. non-dimensional transit time for flows with Reynolds numbers of approximately 5,000 and 50,000, respectively. Multiple data series are given to show the effect of the solution time step on the response of the pipe model. To maintain the accuracy of the dynamic response, the pipe models applies sub-time steps for any simulation time step above 10% of the transit time.

The model—per its name—is limited to simulating turbulent flows. However, this study has used the model for laminar flows as well, so addressing this is recommended future work.

Note that the general methods developed in this chapter for an enhanced response factor model are not dependent on this particular dynamic borehole model. Any dynamic model which computes the short-term, transient temperature response of

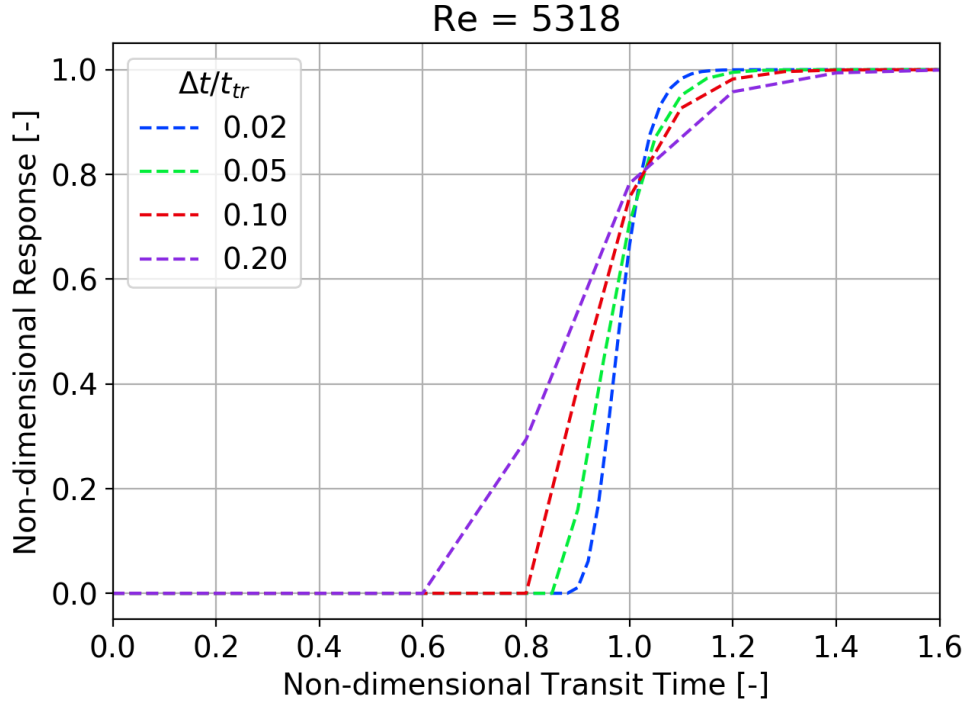


Figure 3.4: Dynamic pipe model response for $Re \approx 5000$

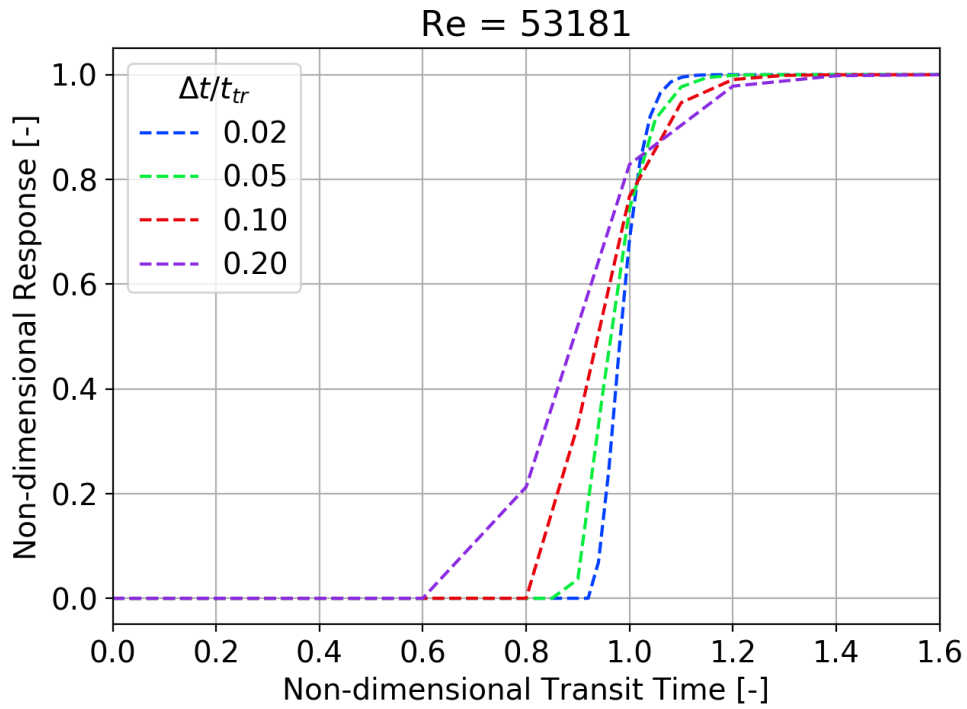


Figure 3.5: Dynamic pipe model response for $Re \approx 50,000$

the borehole could be used, assuming it is accurate and fast to compute.

3.3.3.3 Dynamic Borehole Model Validation

In order to validate the dynamic borehole model, a parametric study using the model was run and compared against experimental data collected by the present author in 2014. The data was collected from two multi-flow rate thermal response tests (MFRTRT) where the heat input rate was held constant and the flow rate was varied at discrete intervals. The first “high” flow rate test varied the flow from 0.15 kg/s, to 0.30 kg/s, to 0.45 kg/s. This resulted in flows with Reynolds numbers of approximately 12k, 21k, 32k, respectively. The second “low” flow rate test varied the flow from 0.02 kg/s to 0.2 kg/s in eight intervals. This resulted in flows with Reynolds numbers ranging from approximately 2.2k to 22k. Additional information regarding the tests is described by Beier et al. (2018).

Since the dynamic borehole model is only expected to be run long enough to generate the ExFT g-functions, the model was only run for 24 h using the GHE inlet conditions recorded from the experimental data. The parameters varied in the study were the grout fraction, number of iterations, number of TRCM segments, and the simulation time step. The results from the parametric study plot the simulation time required for exercising the model for a single flow rate on the vertical axis, and plot the root mean squared error (RMSE) of the exiting fluid temperature on the horizontal axis. Each data point represents the average simulation time and RMSE for an individual configuration for the low and high MFRTRT.

Figure 3.6 shows the effect of varying the grout fraction from 0.25, 0.5, and 0.75. As a reminder, the grout fraction is the fraction of total grout mass associated with each of the grout nodes. A grout fraction of 0.9 indicates that 90% of the grout mass is part of grout node 1, and 10% is part of grout node 2. From the figure, a clear trend relating simulation time and exiting fluid temperature accuracy can not be seen.

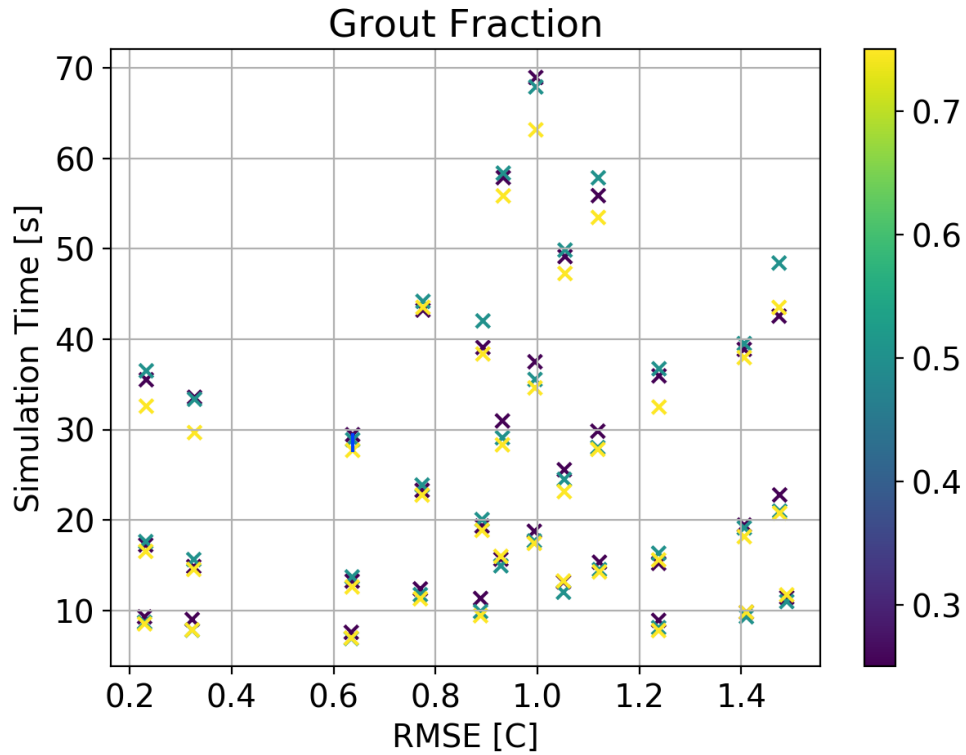


Figure 3.6: Grout fraction effects on dynamic borehole model

Figure 3.7 shows the how variations in the number of iterations affects the simulation time and accuracy of the model. The data connected with a blue line indicate simulations which have the same configuration, but for which the number of iterations are varied. In the figure, we can see that increasing the number of iterations increases the accuracy of the simulation. Differences in simulation time are consistent with more iterations requiring additional simulation time.

Figure 3.8 shows variations in the number of segments used in the TRCM. Again, data connected by the blue line are simulations with the same configuration and a different number of segments. Counter-intuitively the best solution is the one which only utilizes 1 segment. The reason for this behavior is currently unknown.

Finally, Figure 3.9 shows variations due to the effects of changing from 15 s to 30 s time steps. No trend in accuracy is observed. As expected, larger time steps result in lower total simulation times.

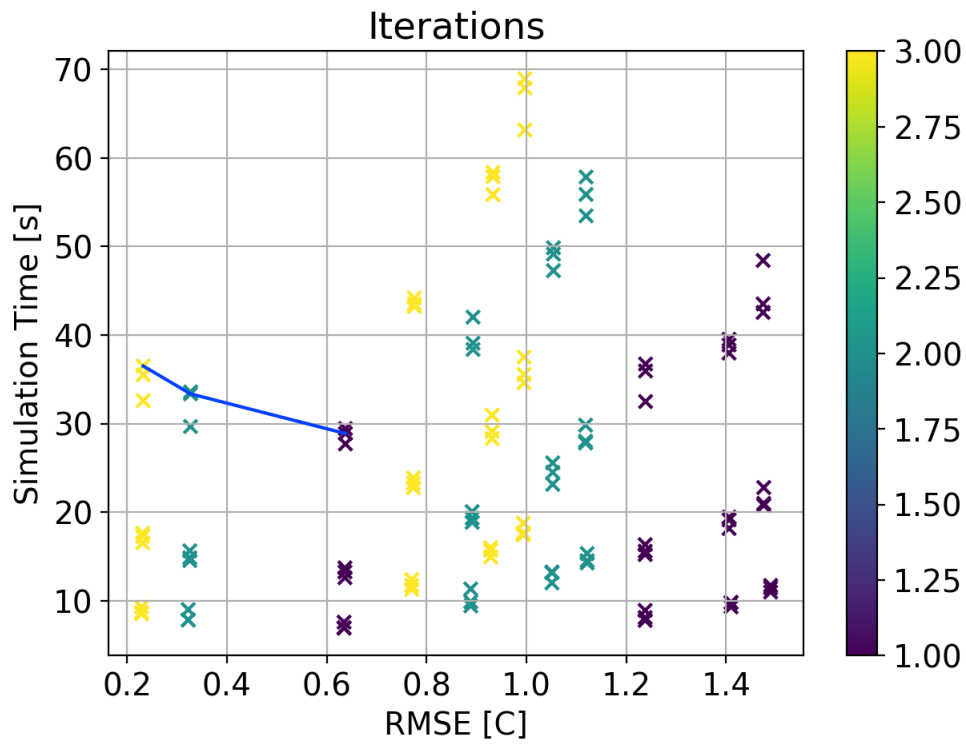


Figure 3.7: Iteration count effects on dynamic borehole model

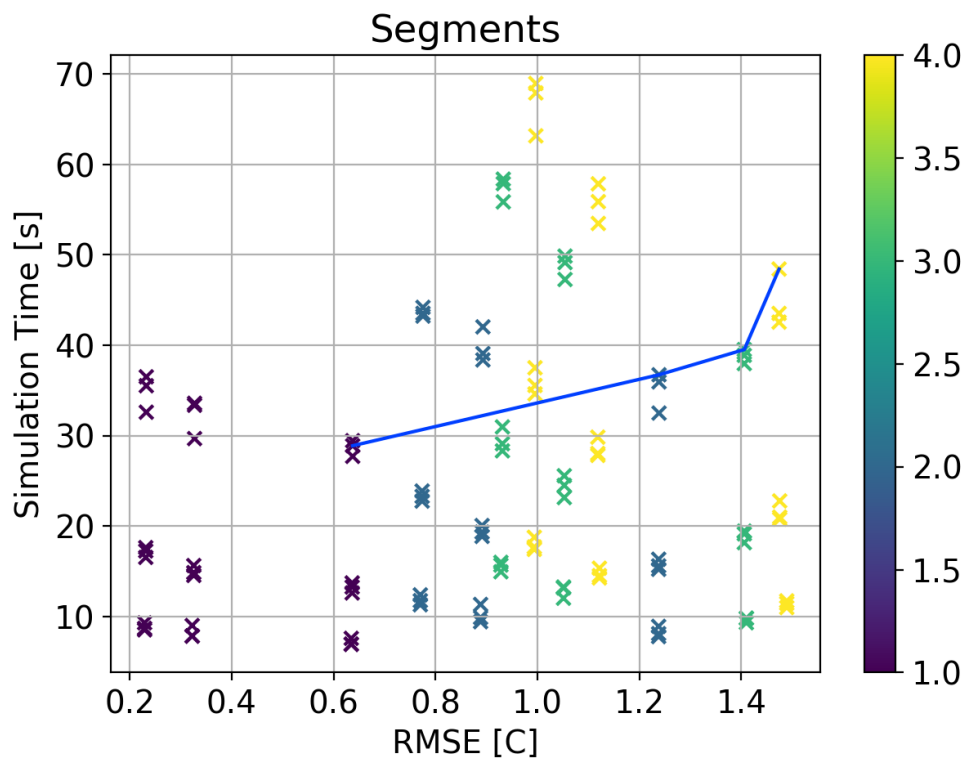


Figure 3.8: Segment count effects on dynamic borehole model

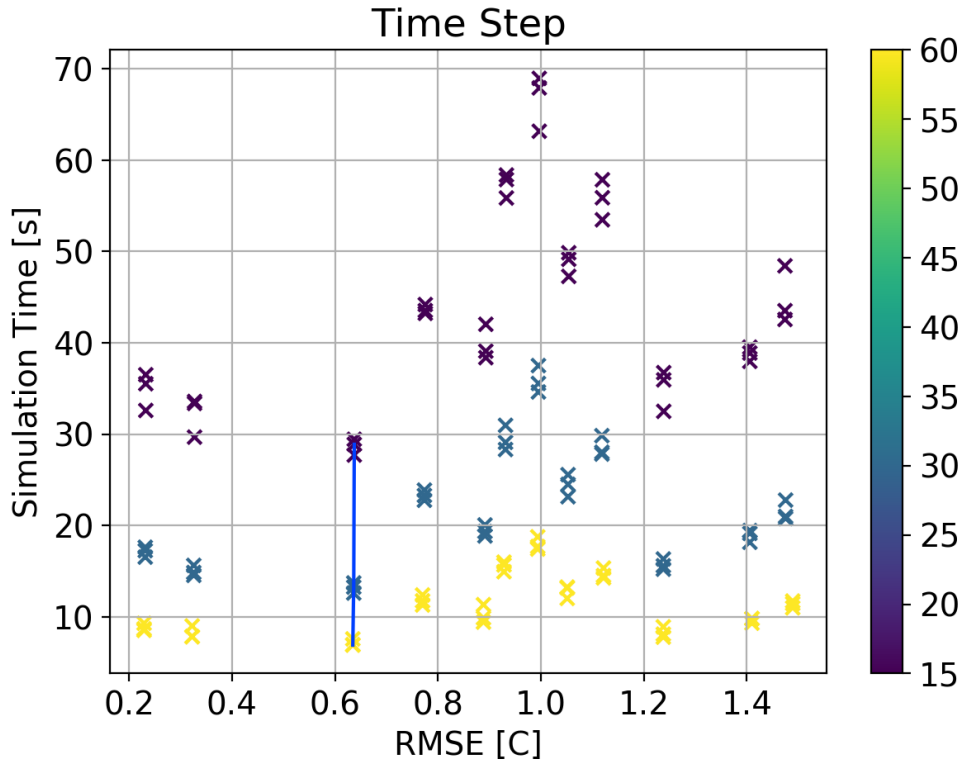


Figure 3.9: Time step effects on dynamic borehole model

Figure 3.10 shows the data with the Pareto front identified. The Pareto front was identified using the “pareto” Python library (Woodruff and Herman, 2018) which employs the popular non-dominated sorting genetic algorithm, NSGA-II (Deb et al., 2002).

The Pareto data is given in Table 3.1. The second configuration identified was then used to run the dynamic borehole model to simulate using additional data from the MFRTRT. The mean bias error (MBE) is also given, which is the average exiting fluid temperature error.

Table 3.1: Dynamic borehole model Pareto data

| N_{it} | N_{seg} | Δt | f_g | RMSE [C] | MBE [C] | Time [s] |
|----------|-----------|------------|-------|----------|---------|----------|
| 3 | 1 | 60 | 0.75 | 0.229 | -0.073 | 8.5 |
| 2 | 1 | 60 | 0.5 | 0.322 | -0.169 | 7.8 |
| 1 | 1 | 60 | 0.5 | 0.634 | -0.448 | 6.9 |

Figure 3.11 show the first two hours of data comparing the high-flow MFRTRT.

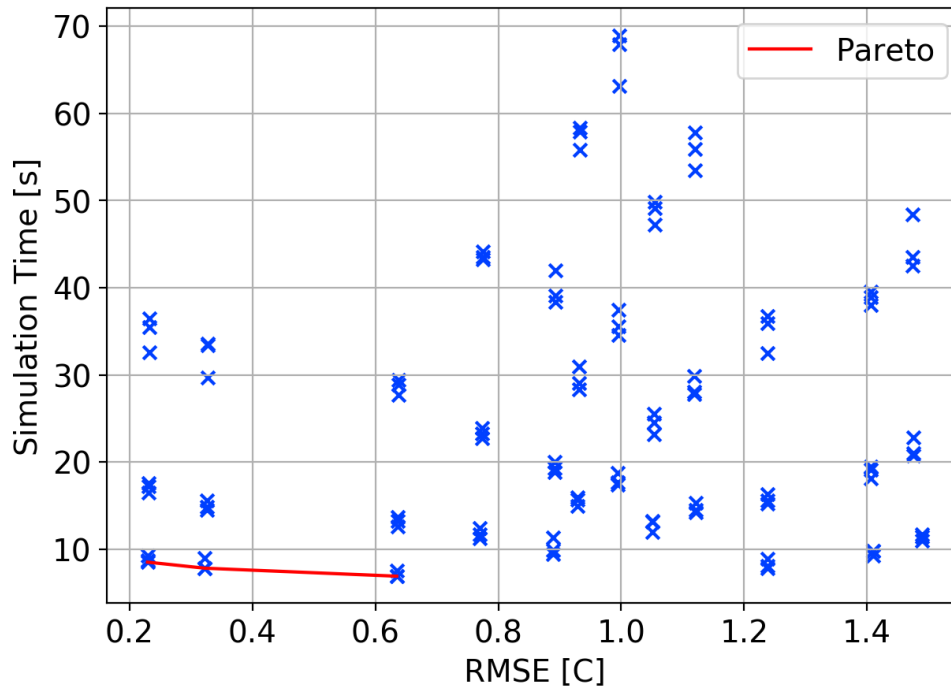


Figure 3.10: Pareto values for variations in dynamic borehole model input parameters

As before, the model is driven from the experimental measurements of the GHE inlet temperature and flow rate. The outlet temperature error is also plotted. Despite the dynamic borehole model being an extremely simple model, the results shown are promising. Some error associated with transit time computation are shown near the first of the test; however, the general trend of the model follows the experimental data well. For most of the first two hours, the exiting fluid temperature error is within 0.5°C .

Figure 3.12 show the full 9 days of the high-flow MFRTRT. Again, during most of the test, the exiting fluid temperature error is within 0.5°C , with the exception of the periods during the flow rate step-change. Again, these are caused by errors in the transit delay prediction.

Figure 3.13 show the first 2 hours of the low-flow MFRTRT. As before, there is some error in the transit time prediction. The flow is laminar during this test. As a reminder, the centerline velocity for laminar flows is $2\times$ the average pipe ve-

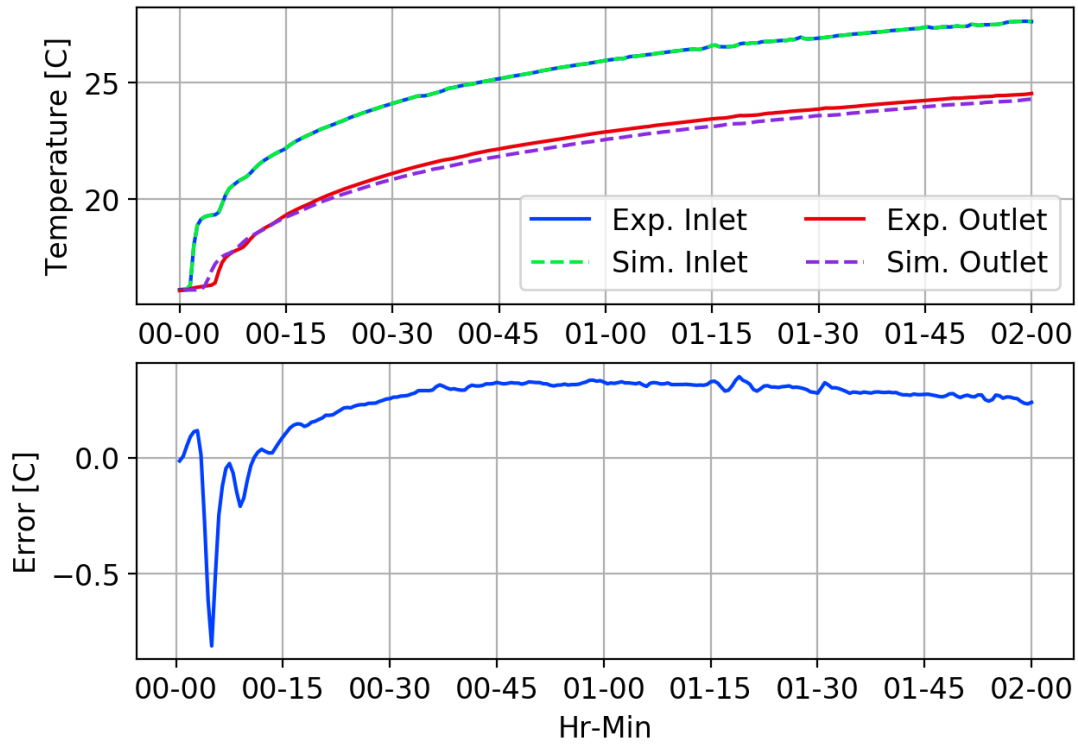


Figure 3.11: Dynamic borehole model compared to first 2 hours of high-flow MFRTRT

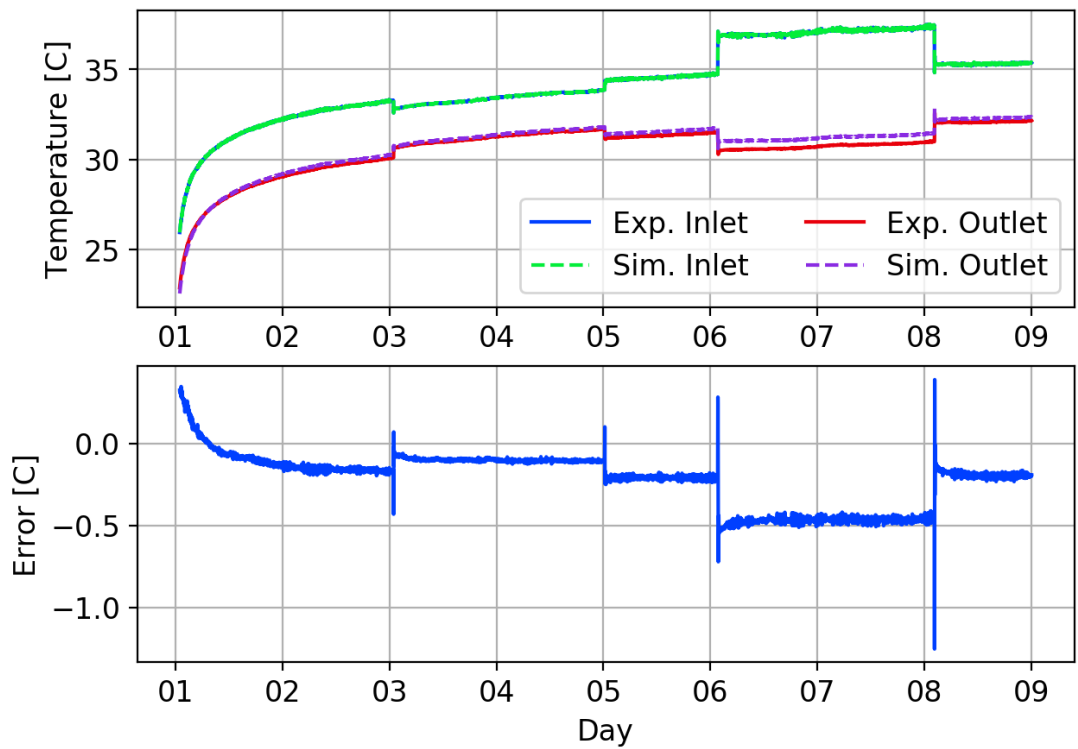


Figure 3.12: Dynamic borehole model compared to high-flow MFRTRT

locity. Therefore, the pipe temperature response will be faster, when comparing non-dimensional transit times than will turbulent flows. Therefore, improving the pipe model to more accurately account for laminar flow will likely correct this error.

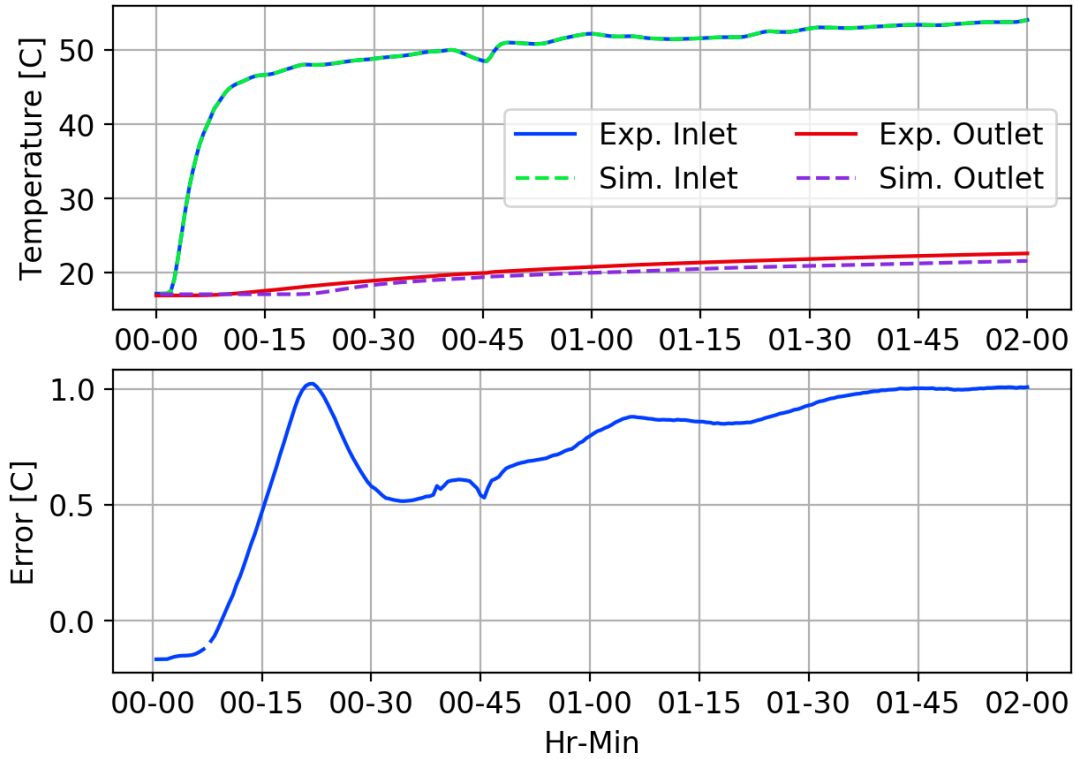


Figure 3.13: Dynamic borehole model compared to first 2 hours of low-flow MFRTRT

Figure 3.14 shows the first two days of the low-flow MFRTRT. Some experimental errors occurred which will require some special treatment to apply the current model. Therefore, no additional comparisons are made beyond the two days shown. Exiting fluid temperature error is slightly higher than the high-flow MFRTRT.

Some improvements could be made to the dynamic borehole model since there is some counter-intuitive behavior occurring. Despite this, the model is sufficient to generate ExFT g-functions for the enhanced response factor model.

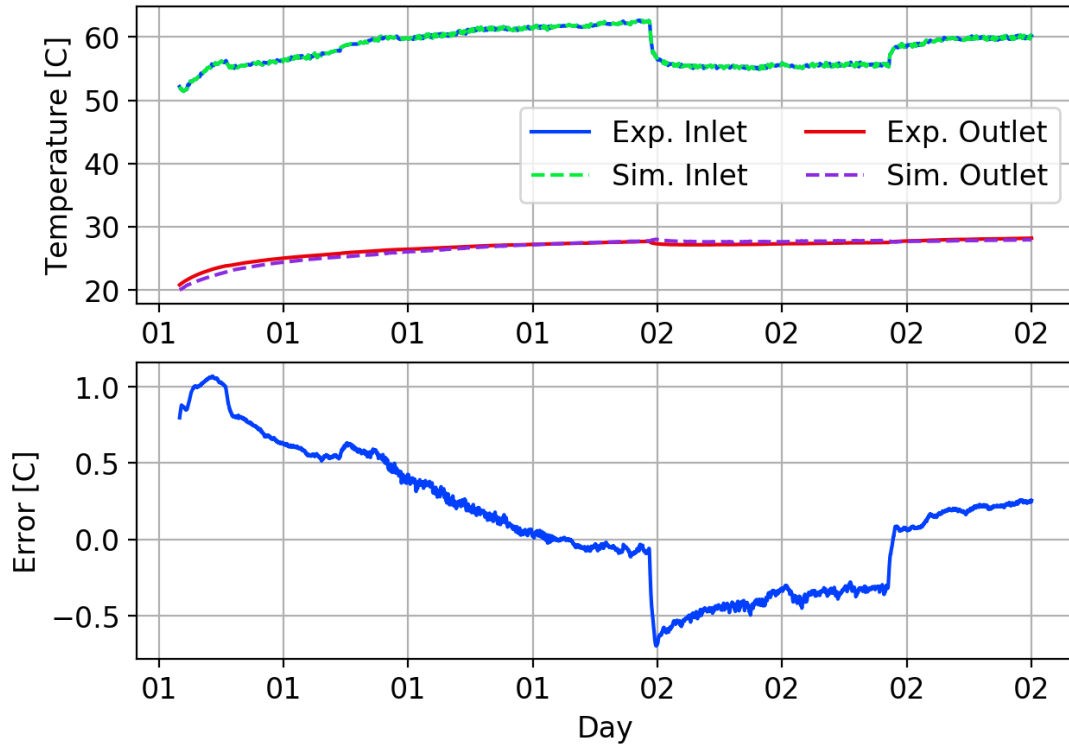


Figure 3.14: Dynamic borehole model compared to 3 days of low-flow MFRTRT

3.3.4 Exiting-Fluid-Temperature Response Factor Generation

To generate the ExFT g -functions, the simplified dynamic borehole model is exercised with a constant heat load and constant flow rate. Once the model is initialized, the inlet flow rate is held constant and the inlet temperature is computed based a first-law energy balance for a fixed heat input rate. The dynamic borehole model exiting fluid temperature is then fed back into the inlet of the GHE after again applying a first-law energy balance for a fixed heat input rate. By exercising the model in this fashion, the transit delay effects can be estimated and incorporated into the g_b values computed.

The temperature response data from the model is then converted to the ExFT g -function values, and given for their respective non-dimensional time. The ExFT g -functions are computed as shown in Equation 3.36. Non-dimensional time that is used for response factor models is computed as shown in Equation 3.37.

$$g_b = \frac{T_{ExFT} - T_b}{q_f \cdot R_b} \quad (3.36)$$

$$\ln(t/t_s) = \ln\left(\frac{t}{H_{ave}^2 / (9\alpha_s)}\right) \quad (3.37)$$

In Equation 3.36, the temperature difference and the heat transfer rate are expected to be proportional to one another, so the only changes expected in the resulting g_b values computed will be due to the borehole resistance calculation. R_b includes the pipe resistance which will be affected by changes in flow rate and fluid temperature. In order to check the sensitivity of the ExFT g -functions to the borehole resistance, g_b was computed for various heat input rates and flow rates, and then R_b values were compared.

Figure 3.15 shows R_b values for a constant flow rate of $\dot{m}_f = 0.2$ kg/s, and variable heat input rates to the dynamic borehole model of, 2, 10, and 40 W/m. Also shown is the error of the 2 and 10 W/m cases from the 40 W/m case. The only variations shown are due to changes in the circulating fluid properties, which are updated each time step using the CoolProp thermophysical fluid properties library (Bell et al., 2014). As expected, g_b values will not be significantly affected by choosing a given value for the heat rate used to exercise the dynamic borehole model.

Figure 3.16 shows R_b for a constant heat rate of $q = 10$ W/m, and variable flow rates. Reynolds numbers for the flow rates vary from about 500 to 50,000. As can be seen, R_b changes significantly due to changes in flow rate. This presents some challenges for the current method, in that the flow rate value used for computing g_b is not arbitrary. Therefore, it is expected that multiple g_b series will need to be computed to account for variations in flow rate.

Figures 3.17 and 3.18 show the temperature rise vs. time for a constant heat input rate of 10 W/m. The borehole modeled is the borehole used by Beier et al. (2018),

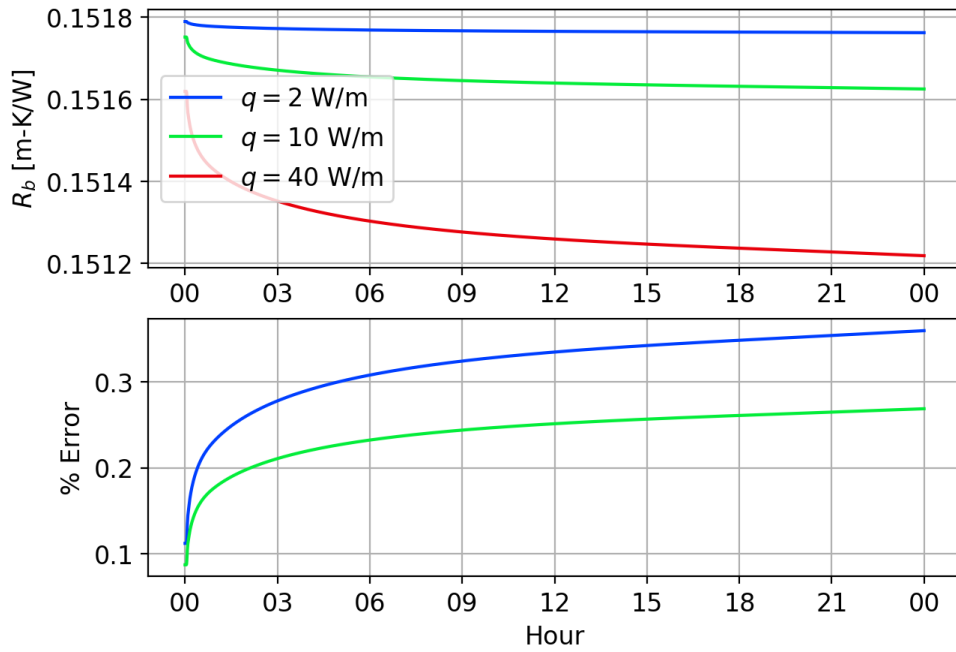


Figure 3.15: R_b vs. time for a constant flow rate, variable heat input rate

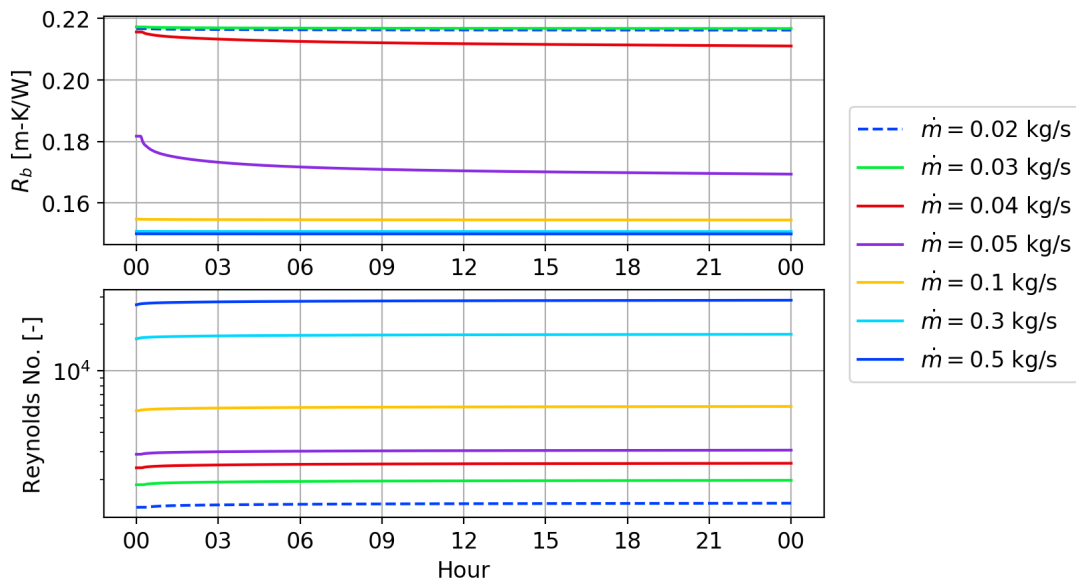


Figure 3.16: R_b vs. time for a constant heat rate, variable circulating fluid flow rate

which is a 76.2 m borehole heat exchanger installed at Oklahoma State University, circa 1995. The flow rate is varied from laminar to turbulent flows.

Figure 3.17 show the temperature response for 2 h of simulation time. The delayed response of the different data series is due to the transit time delay effects. As expected, low flow rates lead to long transit times, where as high flow rates result in low transit times. Figure 3.18 shows the same data, but plotted for 24 h.

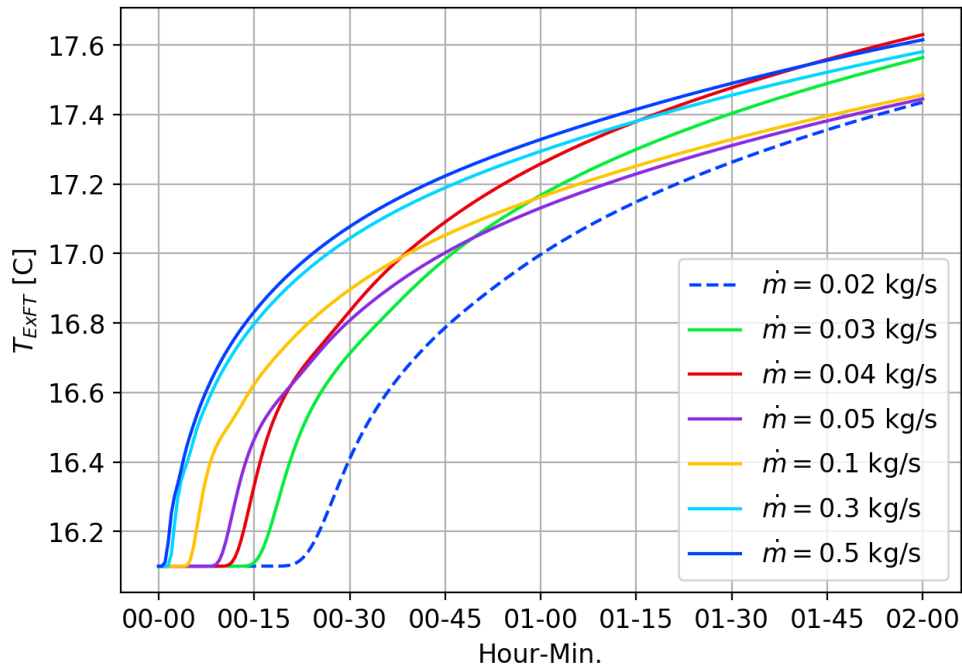


Figure 3.17: Dynamic borehole model temperature response for 2 hours

Figure 3.19 shows the g_b values computed which are plotted vs. non-dimensional time. As expected, higher flow rate data begins to rise sooner than low flow rate data. “Wiggles” in the data are directly related to the transit delay effects. Excerpted data from the g_b computations at $t = 24$ h is given in Table 3.2.

From the Table, we can see that the fluid heat transfer rate is nearly constant. Additionally, the borehole resistance decreases with flow rate, except for the first flow rate of 0.02 kg/s which is 0.5% lower than the resistance at 0.03 kg/s. The cause of this is unknown at the moment, but is likely attributable to differences in fluid property computations due temperature differences. The borehole wall temperature

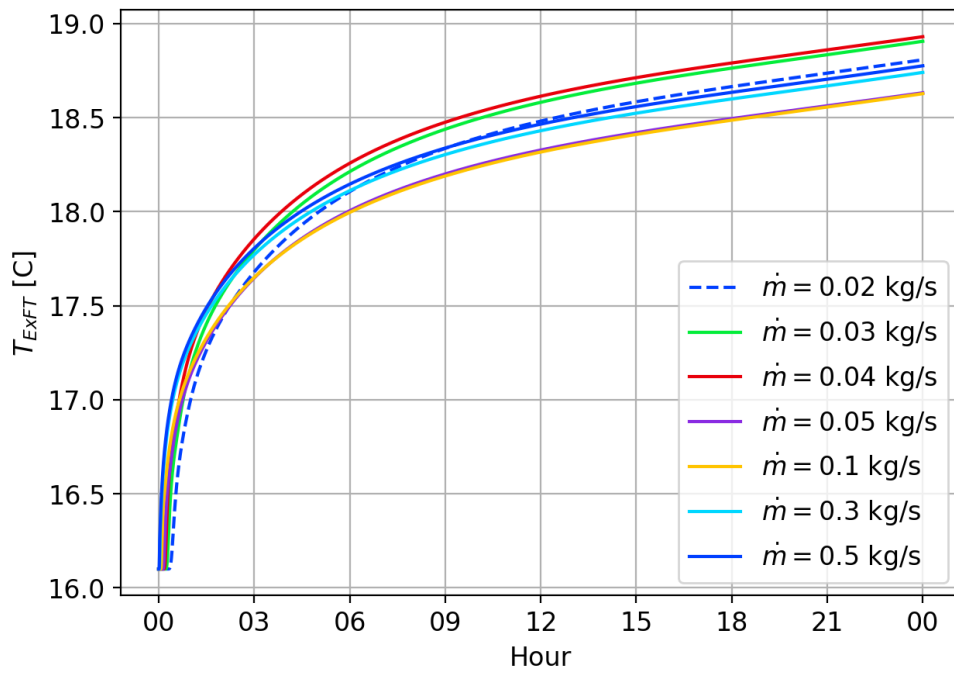


Figure 3.18: Dynamic borehole model temperature response for 24 hours

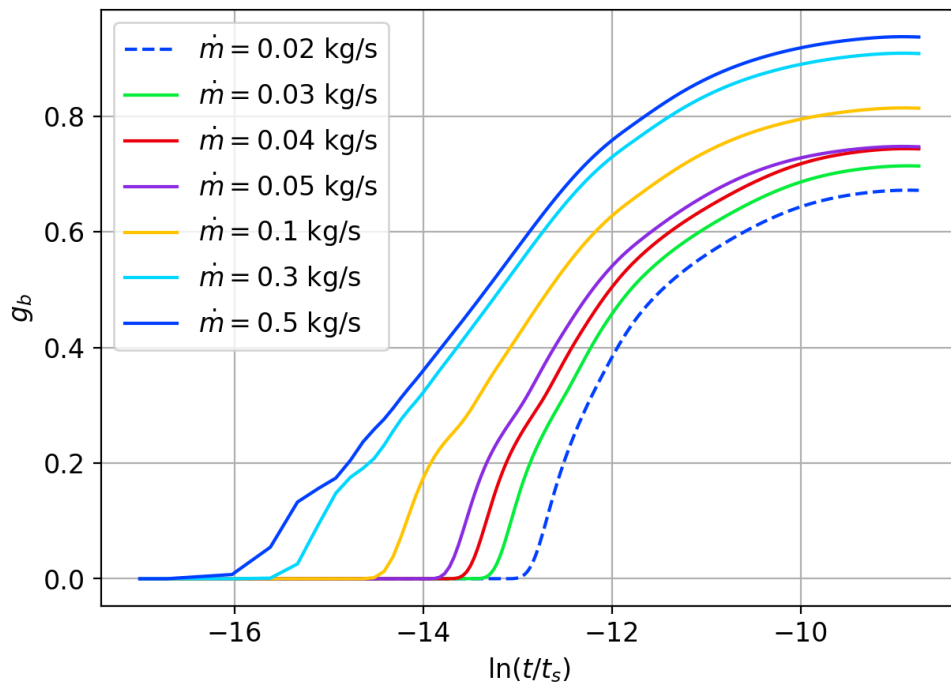


Figure 3.19: g_b vs. $\ln(t/t_s)$

is also nearly constant as is expected since the heat transfer expected at the borehole wall should approach a steady value after enough time, regardless of the fluid flow rate.

Table 3.2: Data from g_b calculations taken at $t = 24$ h

| \dot{m}_f | Re | $\ln(t/t_s)$ | g_b | T_{out} | T_b | q_f | R_b | $T_{out} - T_b$ | $q_f \cdot R_b$ |
|-------------|-------|--------------|-------|-----------|-------|-------|----------|-----------------|-----------------|
| kg/s | - | - | - | °C | °C | W/m | °C/(W/m) | °C | °C |
| 0.02 | 1400 | -8.8 | 0.67 | 18.80 | 17.34 | 9.989 | 0.216 | 1.45 | 2.16 |
| 0.03 | 1967 | -8.8 | 0.71 | 18.89 | 17.35 | 9.991 | 0.217 | 1.55 | 2.16 |
| 0.04 | 2534 | -8.8 | 0.74 | 18.92 | 17.35 | 9.993 | 0.211 | 1.57 | 2.11 |
| 0.05 | 3079 | -8.8 | 0.75 | 18.62 | 17.35 | 9.994 | 0.169 | 1.27 | 1.69 |
| 0.1 | 5894 | -8.8 | 0.81 | 18.62 | 17.36 | 9.996 | 0.154 | 1.26 | 1.54 |
| 0.3 | 17209 | -8.8 | 0.91 | 18.73 | 17.36 | 9.996 | 0.151 | 1.37 | 1.51 |
| 0.5 | 28535 | -8.8 | 0.94 | 18.76 | 17.36 | 9.994 | 0.150 | 1.40 | 1.50 |

Figure 3.20 shows g_b and flow rate values from Table 3.2 plotted with points colored by the borehole resistance. From the figure, we can see that the borehole resistance drops significantly after the flow transitions from laminar to turbulent conditions. Although, from the table we can also see that these points correspond to Reynolds numbers of approximately 2.5k and 3.1k, so the flow transition limits for Nusselt and friction factor correlations may need to be adjusted slightly. Plots of the borehole total internal resistance, R_a , and direct coupling resistance, R_{12} , also show similar behavior.

We should note that the outlet temperature does not increase monotonically from lowest to highest flow rates, as would be expected from a simple heat exchanger analysis with fixed heat transfer rate and boundary conditions. We need to keep in mind, though, that the dynamic borehole model accounts for short circuiting which is affected by the borehole thermal resistance. In addition, the ExFT g-functions are computed based partially on the borehole wall temperature response which changes with time. Careful inspection of Figure 3.18 (and exiting fluid temperature data in Table 3.2) will show that the exiting fluid temperature increases for monotonically for laminar flows, and then increases again monotonically for turbulent flows. There-

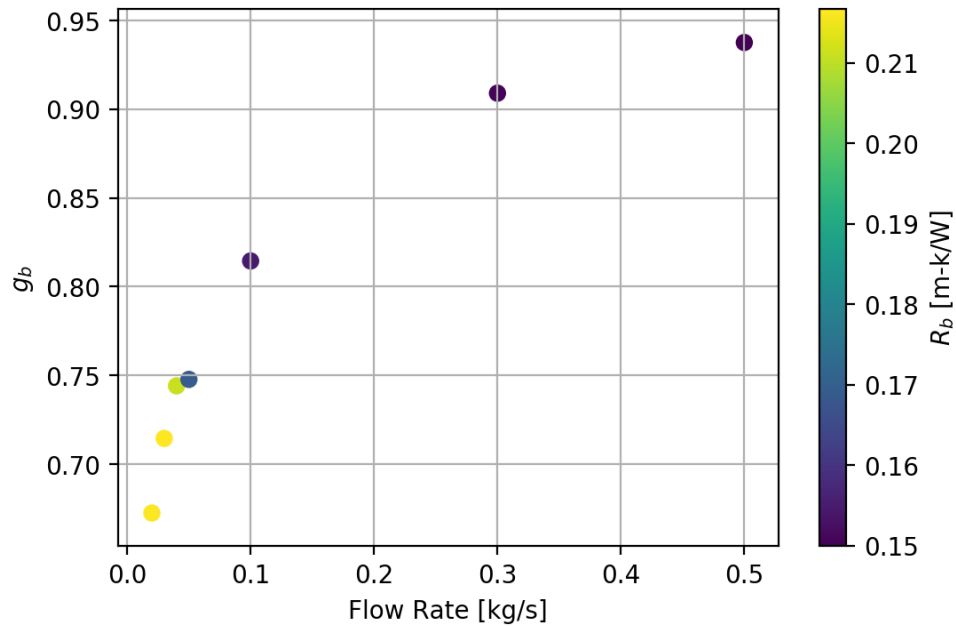


Figure 3.20: g_b vs. flow rate with points colored by R_b , taken at $t = 24$ h

fore, it is expected that this behavior is due to the many interactions between fluid temperature, fluid properties, and flow rate which all affect short circuiting and the dynamic response of the borehole model.

Figure 3.21 shows the fluid heat transfer rate plotted on the vertical axis with the borehole wall heat transfer rate plotted on the horizontal axis.

The dynamic borehole model is exercised with a load of 10 W/m applied to GHE inlet fluid, and as can be seen from Figure 3.21 and Table 3.2, the fluid heat transfer rate is with about 0.1% of that value. However, the borehole wall heat transfer rate has only reached to within about 2% of the steady-state value after 24 h operation time. Therefore, an appropriate convergence limit should be set and checked when generating exiting fluid temperature g-functions.

Because the effect of flow rate is so significant, the ExFT g-function values are computed at a few discrete flow rates over the expected flow rates. The ExFT g-function values are then determined by performing an interpolation between the two independent variables: flow rate and non-dimensional time.

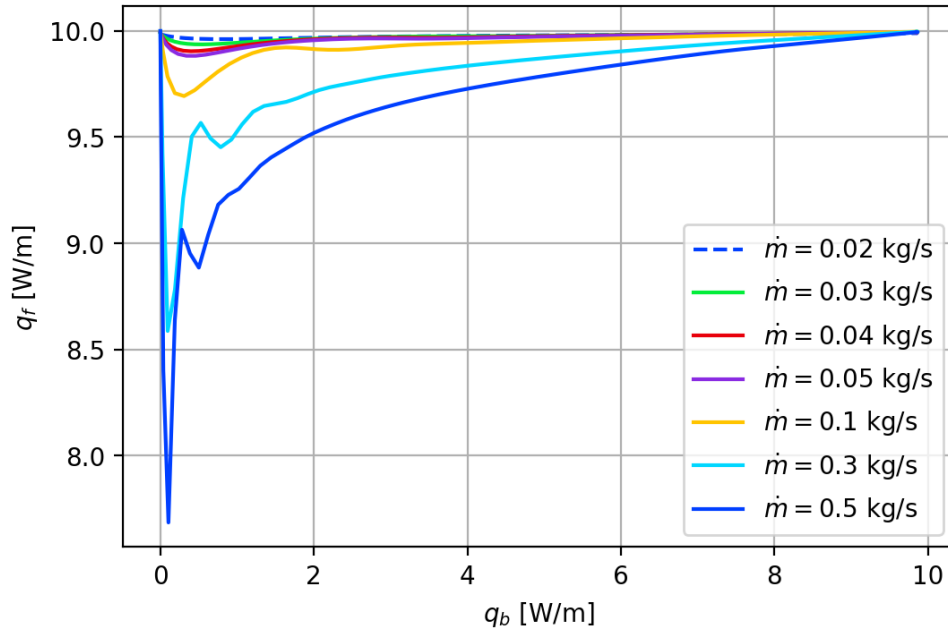


Figure 3.21: q_f vs. q_b for data used to generate g_b data

3.3.5 Borehole-Wall-Temperature Response Factor Generation

Standard g-function values used for computing the borehole wall temperature rise could be computed in any number of ways. These have been discussed in the literature review, and are not repeated here. The methods developed by Cimmino (2018a) will be used through the pygfunction Python library (Cimmino, 2018c) for computing the long time step g-functions. Short time step borehole wall temperature g-functions are computed using the 1D radial finite-volume model developed by Xu and Spitler (2006). These g-functions are plotted for the MFRTRT borehole discussed in Beier et al. (2018) in Figure 3.22. Since it can be difficult to understand non-dimensional time values, some dimensional values are given as well.

As stated previously, the g-function values are evaluated to give the borehole wall temperature rise, not the fluid temperature rise. For this reason, the values approach 0 for lower $\ln(t/t_s)$ values. The original implementation of the model by Xu and Spitler (2006) subtracts off the steady-state borehole resistance so the mean fluid temperature could be computed. Other short time step g-function generation methods do this as

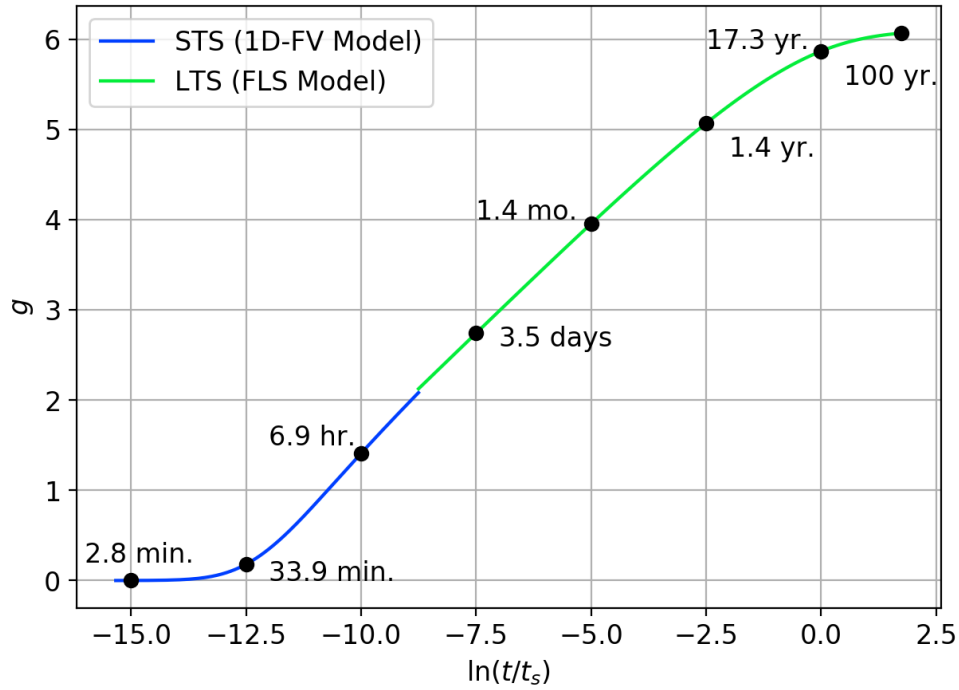


Figure 3.22: g vs. $\ln(t/t_s)$

well; however, this is not correct for the current model's formulation. As expected, some time is required for the heat to conduct from the fluid, through the grout, to the borehole wall. As seen in the plot, this time is on the order of 20-30 min for this particular borehole.

The model by Xu and Spitler (2006) is a 1D, radial finite volume model (Patankar, 1991), which is formulated with a tri-diagonal solution scheme (Moin, 2010). The solution is integrated with a fixed time step of 2 min for 24 h, after which the long time step g -function methods are applied.

As with the dynamic borehole model, the choice of flow rate will affect the short time step borehole wall g -functions. However, since we are evaluating the borehole wall temperature with a fixed heat input rate, the effect on the short time step g -functions is expected to be quite small. Figure 3.23 shows the short time step g -functions computed using different flow rates. The lowest flow rate has a Reynolds number of approximately 500; the highest flow rate has a Reynolds number of ap-

proximately 50,000.

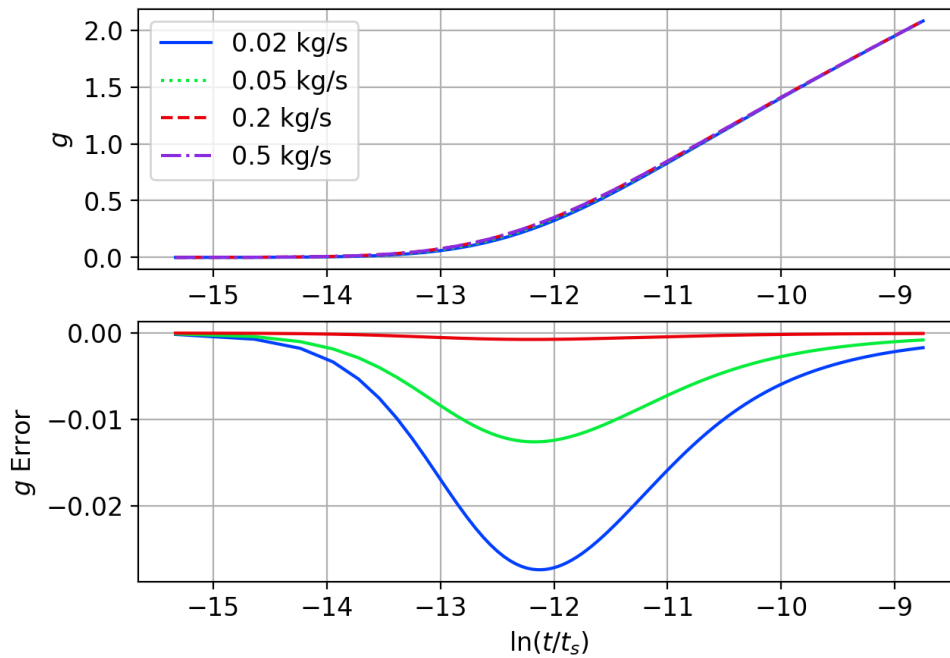


Figure 3.23: Short time step g-functions vs. $\ln(t/t_s)$ for various flow rates

Because the effect is negligible, the model fixes the flow rate at 0.2 kg/s and is not recomputed for different flow rates.

3.4 Validation

The enhanced response factor model is validated using the MFRTRT data. Validation results for the high- and low-flow tests are given. For all cases, the experimental measurements for temperature and flow rate were used as the inlet conditions for the GHE model.

3.4.1 High-flow MFRTRT

Figure 3.24 shows the temperature comparison for the first two hours of the high-flow test. The simulation was run using a 60 s time step. As occurred during the comparison of the dynamic borehole model, some transit delay errors are present

during the first five minutes of the simulation which result in larger errors in the temperature predicted. However, once the first flow transit periods have passed, the model and experimental data agree quite well.

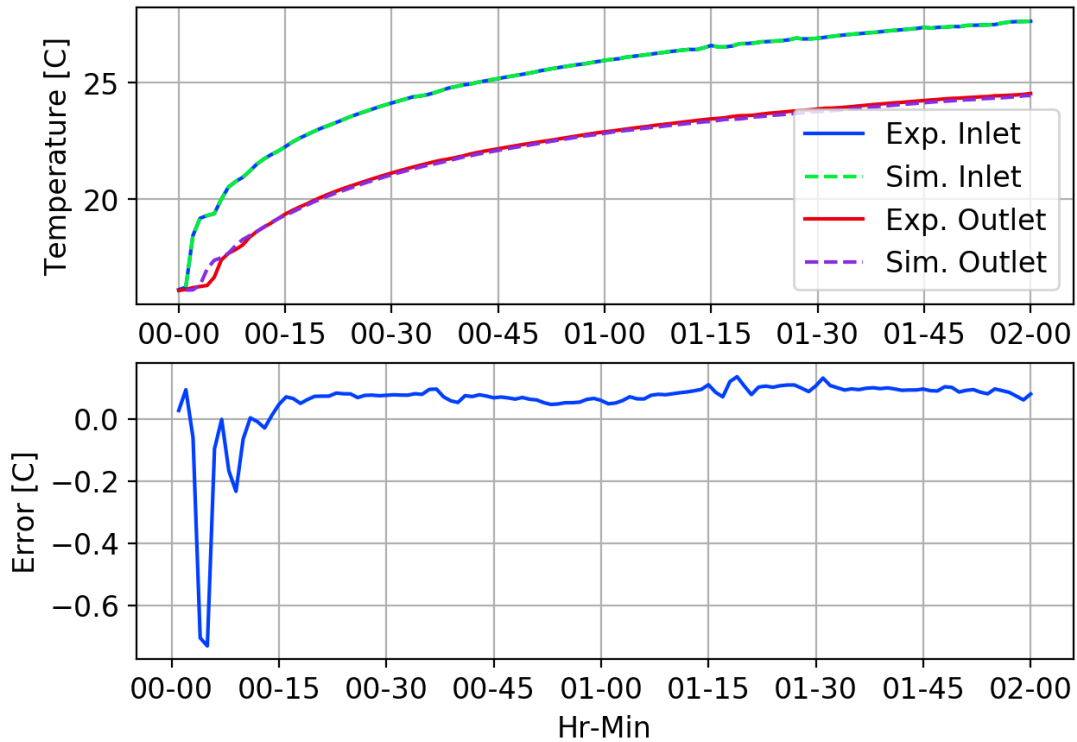


Figure 3.24: Enhanced model results for high-flow MFRTRT. First 2 hours. 60 s time step.

Figure 3.25 shows the temperature comparison for the first flow rate change using a 60 s time step. During this period, the flow rate is changed from approximately 0.3 kg/s up to 0.45 kg/s, which results in a smaller temperature difference between the inlet and outlet of the GHE. The figure shows good a dynamic response compared to the experiment during this step change in flow, and the absolute outlet temperature error remains under 0.2°C.

Figure 3.26 shows the temperature comparison for the fourth flow change during the high-flow MFRTRT. Again, a 60 s time step is used for the simulation. In this case, the flow rate steps from 0.3 kg/s down to 0.15 kg/s, resulting in a larger temperature difference. The dynamic response in this case is not as good as the data shown

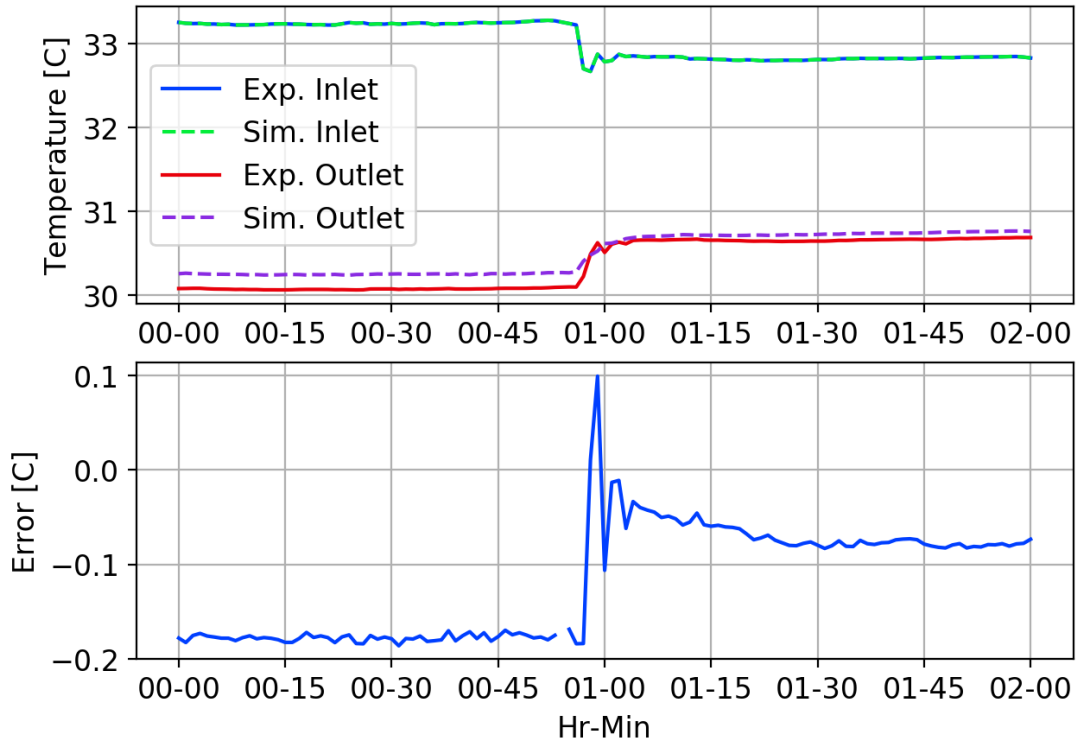


Figure 3.25: Enhanced model results for high-flow MFRTRT. First flow rate change. 60 s time step.

from the previous flow rate change. Here, maximum absolute errors of about 0.8°C are observed briefly; however, this can be attributed to the errors in the dynamic borehole model transit time prediction. Absolute errors after this settle between 0.5 - 0.6°C . Referring back to Figure 3.12, we can see that a similar error is occurring for the dynamic borehole model. This suggests that the error is due to inaccuracies in the dynamic borehole model, and that improvements to this model would likely result in better overall temperature predictions from the enhanced response factor model.

Figures 3.27 and 3.28 show the full high-flow MFRTRT data compared using the enhanced response factor model using 60 s and 1 h time steps, respectively. Figure 3.27, as in previous plots, show higher errors at times when the flow rate changes, but level off after that. Again, these errors are attributed to the errors in the transit time predicted using the dynamic borehole model. The overall temperature difference is generally under predicted by about 0.5°C .

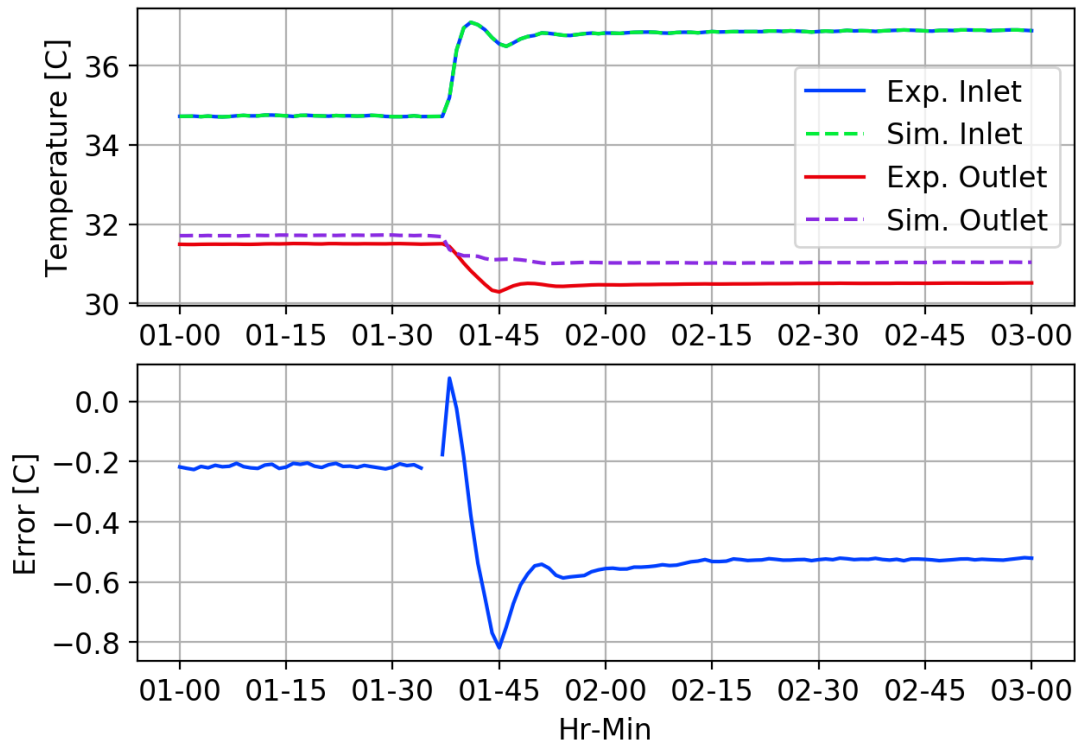


Figure 3.26: Enhanced model results for high-flow MFRTRT. Fourth flow rate change. 60 s time step.

For the simulation using a 1 h time step which is shown in Figure 3.27, these transit time errors are not present since a 1 h time step is between $10\text{-}30\times$ the GHE transit time. The overall trend of the exiting fluid temperature error is consistent with the 60 s time step simulation data.

Another comparison which can be made is by looking at the effects of directly using the ExFT g-function values which were computed for the current flow rate, or by interpolating between ExFT g-function values which were computed for different flow rates. The high-flow MFRTRT has three discrete flow rates: 0.15 kg/s, 0.3 kg/s, 0.45 kg/s. To compare, simulations were run using 60 s and 1 h time steps using either the ExFT g-function values computed for the correct flow rate, or using interpolated ExFT g-functions values from ExFT g-functions which were computed for 0.1 kg/s, 0.3 kg/s, 0.5 kg/s. In this case, ExFT g-functions for the middle flow rate will not be interpolated, but the higher and lower flow rates will be.

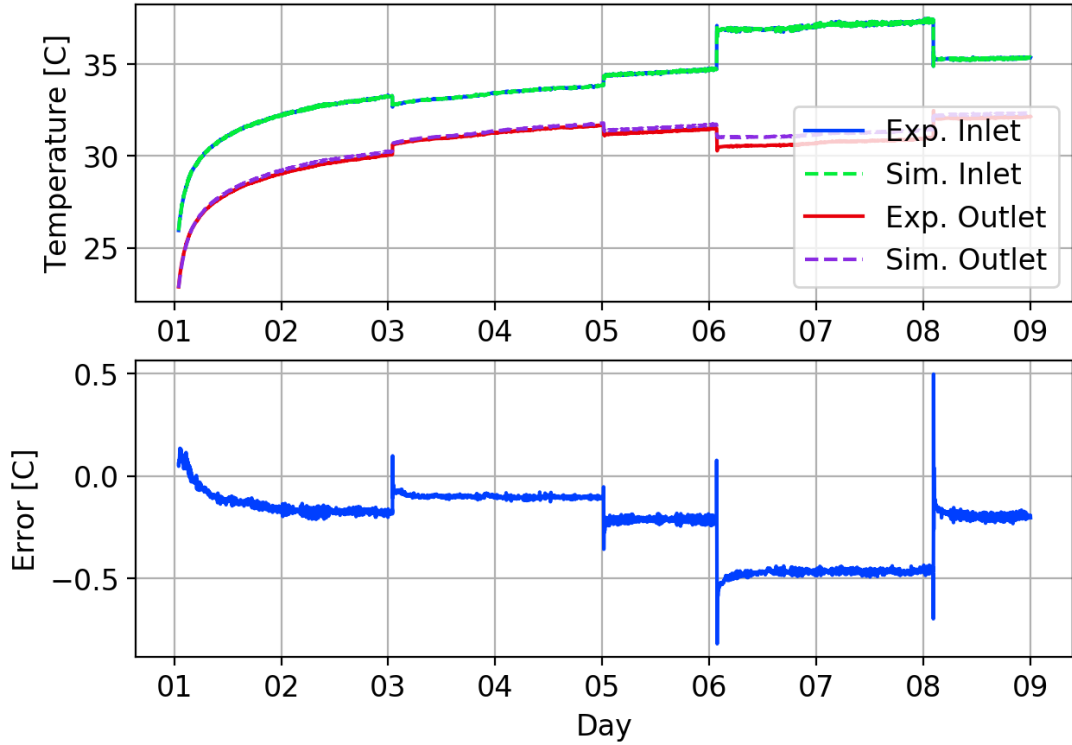


Figure 3.27: Enhanced model results for high-flow MFRTRT. Full data set. 60 s time step.

Table 3.3 shows the RMSE and MBE for the high-flow simulations directly using ExFT g-functions for the current flow rate, or by interpolating between flow rates. The results show a very slight decrease in accuracy for using the ExFT g-functions for the correct flow rate vs. the interpolated g-functions. However, it should be noted that due to the already-noted errors in the dynamic borehole model, these differences in RMSE and MBE are not be considered the final word on whether or not the method affects the results. At the very least, we can say that interpolating between g-function values does not significantly affect the results. This is at least for flow changes that remain within the turbulent flow regime.

Table 3.3: RMSE/MBE for High-Flow MFRTRT

| Time Step [s] | 60 | | 3600 | |
|---------------|---------|--------|---------|--------|
| Scheme | Interp. | Direct | Interp. | Direct |
| RMSE [C] | 0.2721 | 0.2886 | 0.4182 | 0.4289 |
| MBE [C] | 0.2161 | 0.2886 | 0.2059 | 0.2152 |

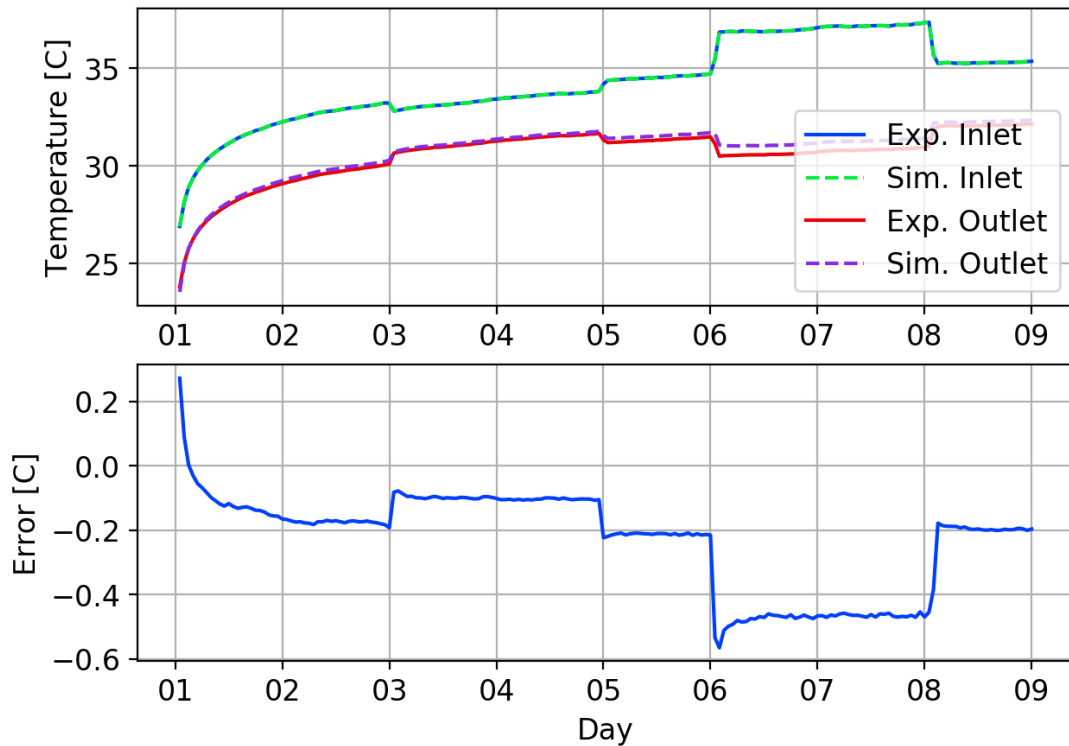


Figure 3.28: Enhanced model results for high-flow MFRTRT. Full data set. 1 hr time step.

Figures 3.29 and 3.30 shows the heat transfer error from the experimental data and the simulation, for a 60 s and 1 h time step, respectively. In both cases, the heat transfer error is less than -10%, except during flow changes, and near -5-6% for the test duration. Note that the experimental uncertainty in the heat transfer measurements are not shown here, but are discussed in Beier et al. (2018). For the high-flow test, the heat transfer error is generally around $\pm 3-7\%$, depending on flow rate. Additionally note that the soil and grout parameters are estimated values, and that changes in these values can easily affect the results enough to affect the error predicted. Further optimization of the soil and grout parameter values could result in reductions to the the overall error.

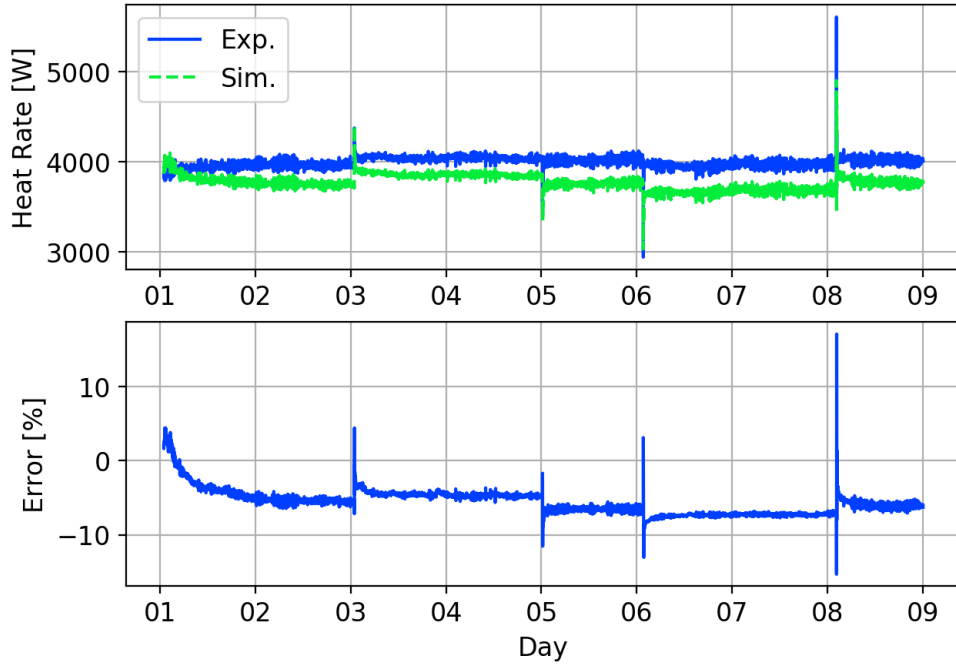


Figure 3.29: Enhanced model heat transfer results for high-flow MFRTRT. Full data set. 60 s time step.

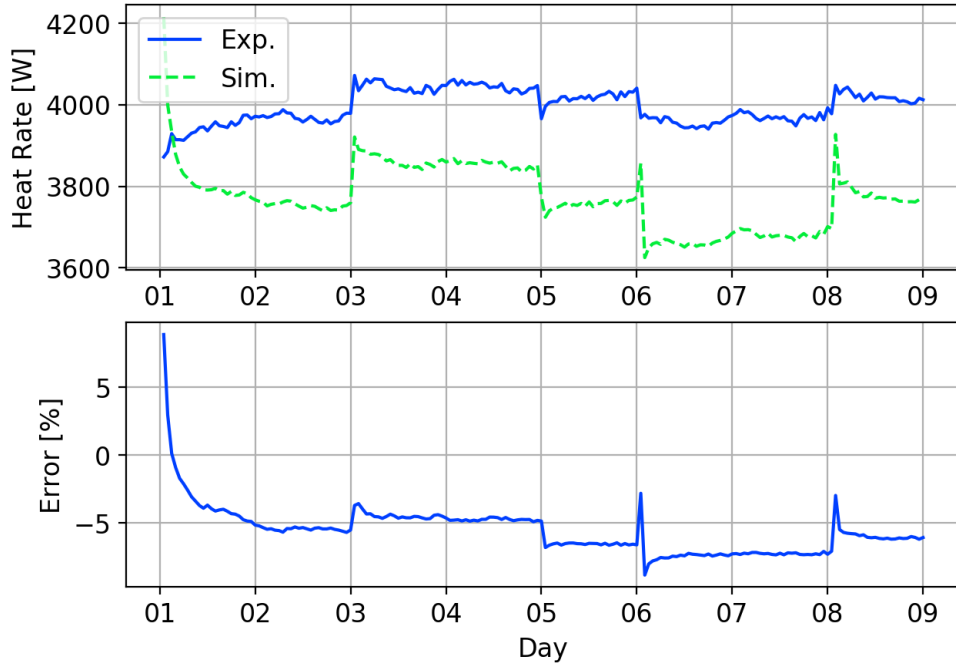


Figure 3.30: Enhanced model heat transfer results for high-flow MFRTRT. Full data set. 1 hr time step.

3.4.2 Low-Flow MFRTRT

Figure 3.31 shows the model compared to 68 h of data from the low-flow MFRTRT. The absolute exiting fluid temperature error is higher than the high-flow test, as the temperature difference is under predicted by about 1 °C. As with the high-flow test, a similar error can be seen from in Figure 3.14 from the direct simulation using the dynamic borehole model. Again, this suggests that errors in the enhanced response factor method can be addressed by improving the accuracy of the dynamic borehole model used to generate the ExFT g-functions.

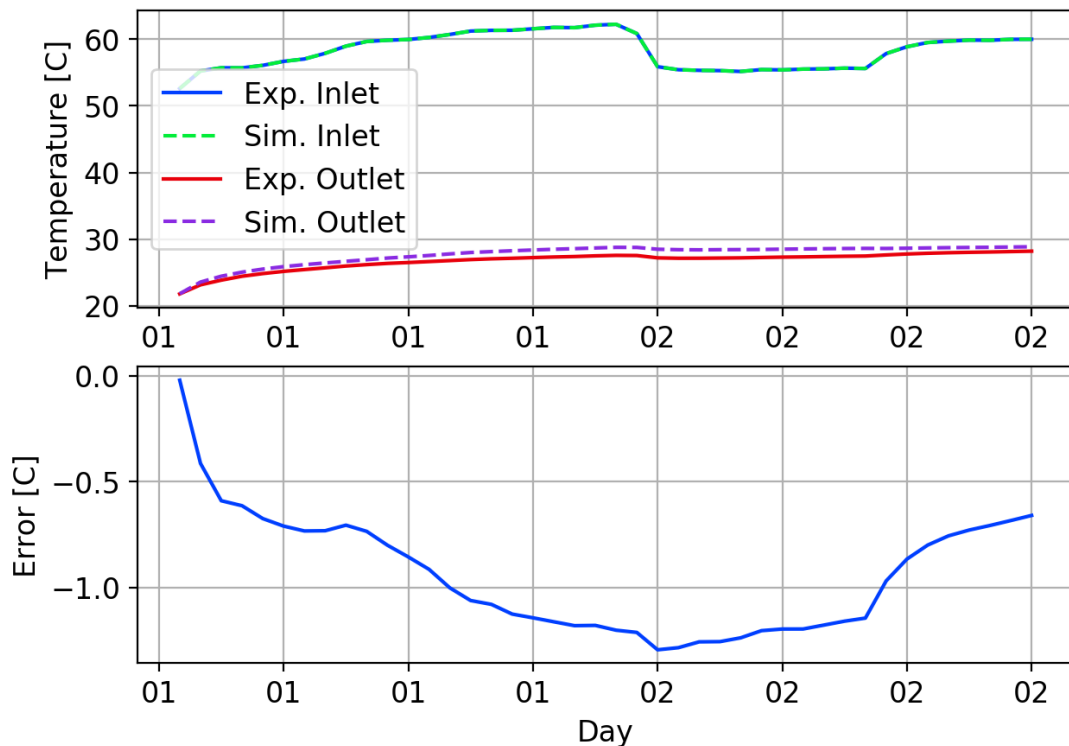


Figure 3.31: Enhanced model temperature results for low-flow MFRTRT. Full data set. 1 hr time step.

Figure 3.32 shows the heat transfer results for the low-flow test compared to the simulation. As before, the experimental heat transfer rate errors are not plotted, but for this particular flow rate they are around $\pm 3\%$. Variations in soil properties will also affect the results.

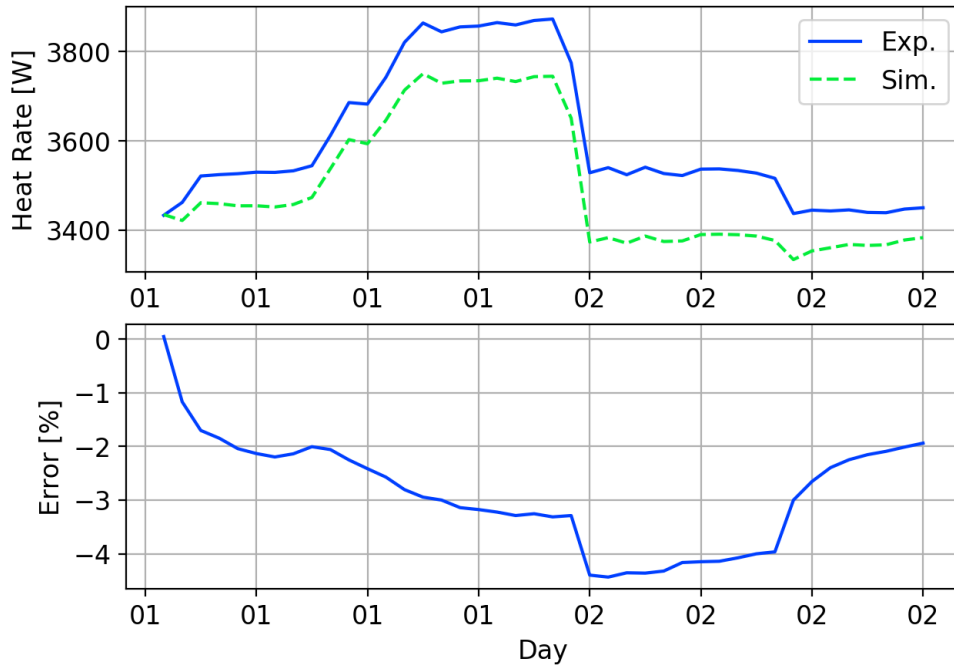


Figure 3.32: Enhanced model heat transfer results for low-flow MFRTRT. Full data set. 1 hr time step.

Table 3.4 shows the RMSE and MBE error simulations where the ExFT g-functions were interpolated within a flow range, or given directly for the current flow rate. As with the high-flow test, the error increases slightly for the non-interpolated case. Again, due to the already-known errors in the dynamic borehole model, these differences are not significant.

Table 3.4: RMSE/MBE for Low-Flow MFRTRT

| Time Step [s] | 60 | | 3600 | |
|---------------|---------|--------|---------|--------|
| Scheme | Interp. | Direct | Interp. | Direct |
| RMSE [C] | 0.9240 | 0.9278 | 0.9507 | 0.9540 |
| MBE [C] | 0.8761 | 0.8809 | 0.8561 | 0.8606 |

3.5 Conclusions and Recommendations

This work describes an enhanced response factor model for use in whole-building energy simulation environments. Using the new model, the work has shown that accurate dynamic behavior can be simulated for GHE using response factor calcula-

tions. The results are shown to be accurate for time steps which are shorter than the GHE transit time, as well as long time steps.

A simplified dynamic borehole model was also developed which is used to generate exiting fluid temperature g-functions. Inaccuracies in the enhanced response factor model were shown to be directly related to inaccuracies in the simplified dynamic borehole model, though, the methods generally compare well against experimental multi-flow rate.

This work has as shown good results in the performance of the proposed method; however, a number inaccuracies were identified and improvements can be recommended.

1. The pipe model currently used does not account for laminar flow, therefore, pipe model should be enhanced to accurately account for these conditions.
2. The dynamic borehole model currently has some counter-intuitive behavior, such as the accuracy decreasing with an increased number of segments. The issues underlying this behavior should be determined and corrected.
3. Any dynamic borehole model could be used to generate ExFT g-functions. Therefore, a study should be performed to assess this model along with other existing models for accuracy and performance.

CHAPTER IV

CROSS-g-FUNCTION RESPONSE FACTORS FOR THE SIMULATION OF INTERFERENCE BETWEEN GROUND HEAT EXCHANGERS

4.1 Introduction

Response function methods for analysis of ground heat exchangers used in ground-source heat pump systems were originally developed by Prof. Johan Claesson and his PhD student, Per Eskilson. (Claesson and Dunand, 1983; Eskilson, 1987; Claesson and Eskilson, 1988). These methods rely on spatial superposition to develop a response function for specific geometric arrangements of boreholes. The response function, known as a g-function, gives the borehole wall temperature due to a constant heat input rate, as shown in Equation 4.1.

$$T_b = T_s + \frac{q}{2\pi k^*} \cdot g(t/t_s, r_b/H, B/H, D/H) \quad (4.1)$$

Time is non-dimensionalized against the time scale, t_s , as shown in Equation 4.2.

$$t_s = \frac{H^2}{9\alpha_s} \quad (4.2)$$

For design purposes, g-functions are often computed and compiled in libraries. Methods for computing g-functions are reviewed by Spitler and Bernier (2016); for recent improvements, see Cimmino (2018a). Once the g-function has been calculated, temporal superposition is used to account for the present and past loads on the ground

heat exchanger, as shown in Equation 4.3.

$$T_b = T_s + \sum_{i=1}^n \frac{q_i - q_{i-1}}{2\pi k^*} \cdot g\left(\frac{t_n - t_{i-1}}{t_s}, r_b/H, B/H, D/H\right) \quad (4.3)$$

This elegant and computationally efficient solution has served well for design tools (Spitler, 2000; BLOCON, 2017) and simulation models (Yavuzturk and Spitler, 1999; Fisher et al., 2006) In all cases, the ground heat exchanger¹ is assumed to operate without thermal interference from other ground heat exchangers. The ground heat exchanger (GHE) is assumed to be made up of a fixed number of boreholes, all of which serve the same heating and cooling loads.

However, as ground-source heat pump systems have become increasingly more popular, situations arise where it would be useful to be able to analyze the impact of one GHE upon other nearby GHE. Examples include:

- Determining the effect of nearby ground heat exchangers in densely packed urban environments. How will your neighbor’s GHE affect your GHE? Witte (2018) has developed a graphical method for use in The Netherlands based on line-source theory. (Thomson, 1884; Ingersoll et al., 1954) This method has been used since 2014 for assisting GHE design. The author acknowledges that the method is simplified and that the simplifications introduce error, however, the error is shown to be conservative. Fasci et al. (2018) investigates the effects of load averaging and temporal resolution of thermal loads for interfering GHE systems.
- When an existing GHE is insufficient to meet the building loads, whether due to a poor initial design or changes in the building loads, adding additional

¹To be clear, the term “ground heat exchanger” here means one or more borehole heat exchangers that all serve the same load. There is, of course, thermal interference between the individual borehole heat exchangers within the ground heat exchanger. The fact that the borehole heat exchangers all serve the same load does not mean that the heat rejected or extracted is uniformly applied over the entire ground heat exchanger. See Malayappan and Spitler (2013) for the impact of assuming uniform heat flux over the ground heat exchanger.

boreholes may be the best solution. In this case, the borehole configuration changes with time and a practical analysis approach is to treat the old GHE and the new portion of the GHE as separate GHEs serving the same load, but with different start dates.

- Yu et al. (2017) have proposed zoning of the ground heat exchanger for cooling-dominated buildings that have a high ratio of heat rejected to heat extracted. By only operating the perimeter boreholes in the cooling season, the excess heat rejected to the ground is more effectively dissipated. The ability to model the two separate zones of the GHE as separate GHEs with different load schedules would facilitate design of such systems.

Therefore, the objectives of this paper include definition of a “cross” g-function that gives the temperature response of one GHE to another GHE, presentation of a method for calculating the cross-g-function, validation of the method, and application of the methodology to examine the densely-packed residential GHE problem.

4.2 Definition

First, where confusion may arise, we will call the original g-functions defined in Equation 4.1, the “self-g-function” and may use the conventional nomenclature (a “ g ” without subscripts). For sake of clarity, since it is possible that there will be more than two GHE, self-g-functions may be notated as $g_{A \rightarrow A}$ for the effect of GHE A on GHE A . The cross-g-function giving the temperature impact of GHE B on GHE A will be designated $g_{B \rightarrow A}$. The original definition of the self-g-function utilizes a non-dimensional time as shown in Equation 4.2 – using the average, active depth of the self-boreholes and the soil’s thermal diffusivity. We will assume here that the soil diffusivity is the same for all GHE being analyzed, but the active depth of the two GHE may well be different. The original definition of the self-g-function is implicitly a non-dimensional temperature change. Rearranging Equation 4.1:

$$g(t/t_s, r_b/H, B/H, D/H) = \frac{(T_b - T_s) 2\pi k^*}{q} \quad (4.4)$$

This form requires the heat pulse, q , to represent the heat input per unit length of ground heat exchanger. Non-dimensionalization of the temperature rise and time when two different ground heat exchangers are involved may no longer be as useful as it was for self-g-functions. At present, we do not anticipate creating libraries of cross g-functions, though it might be useful for the residential interference problem. In such a case, the cross g-function might become a function of the depth ratio of the two heat exchangers. Furthermore, for the cross g-function, we do not anticipate the r_b/H of the nearby GHE to be important. Nevertheless, for computational convenience, we retain the non-dimensionalization as follows:

$$g_{B \rightarrow A} \left(\frac{t_n - t_{i-1}}{t_{s,A}} \right) = \frac{(T_{b,A} - T_s) 2\pi k^*}{q_B} \quad (4.5)$$

It should be understood that $g_{B \rightarrow A}$ is computed for the specific geometries of GHEs A and B , and no attempt is being made to generalize them to other geometry/size combinations. As can be seen in Equation 4.5, the time scale is for the GHE A and the heat input pulse is applied to GHE B . Then, for a case where there are two GHEs, A and B , the borehole wall temperature for GHE A can be computed as:

$$\begin{aligned} T_{b,A} = T_s + \sum_{i=1}^n \frac{(q_{A,i} - q_{A,i-1})}{2\pi k^*} \cdot g_{A \rightarrow A} \left(\frac{t_n - t_{i-1}}{t_{s,A}}, r_b/H, B/H, D/H \right) \\ + \sum_{i=1}^n \frac{(q_{B,i} - q_{B,i-1})}{2\pi k^*} \cdot g_{B \rightarrow A} \left(\frac{t_n - t_{i-1}}{t_{s,A}} \right) \end{aligned} \quad (4.6)$$

If there are more GHE, the second row of Equation 5 could be placed in a summation covering GHEs C , D , E , etc.

4.3 Methodology for Calculating Cross-g-functions

Several methods have been developed for calculating self-g-functions. These methods have evolved to be able to use different mathematical modeling techniques for better accuracy and computation speed. The methods have also evolved to be able to handle different boundary conditions.

The original method developed by Eskilson (1987) developed what is termed the superposition borehole model which is a 2D radial-axial numerical model of a single borehole to the surrounding soil. From this, the temporal response of the temperature field is established, which when spatial and temporal superposition is applied can be used to determine the average temperature response of the GHE. Calculation of g-functions with this method is computationally intensive and is therefore not well-suited for implementation within design applications. As a result, libraries of pre-computed g-functions are commonly used for design applications.

Libraries of g-functions contain g-functions curves for different configurations, such as GHE arranged in linear, rectangular, or square arrangements. Additionally, for each configuration g-functions for discrete B/H ratios are stored. At runtime, a g-function for a specific configuration and B/H ratio is determined by interpolation. This process can lead to errors (Malayappan and Spitler, 2013) . These libraries of g-functions are also not suitable for simulations with short time steps and are thus commonly referred to as long time step g-functions. As a result, Yavuzturk and Spitler (1999), and later Xu and Spitler (2006), developed simplified radial-numerical models of the borehole to determine short time step g-functions.

Zeng et al. (2002), Lamarche and Beauchamp (2007), and Claesson and Javed (2011), among others have investigated and developed methods using finite line source techniques to determine g-functions. These methods have been applied for different applications, such as determining the g-functions for inhomogeneous soils, inclined boreholes, and flowing ground water. These methods will not be reviewed here,

except by referring the reader to Cimmino (2018a) where the interested reader can readily find many references to other works on the subject.

Often references about methods on the subject of g-function generation discuss the possible boundary conditions which have been, or which should be applied. Specifically, what is the boundary condition at the borehole wall? Cimmino and Bernier (2014) discuss three potential boundary conditions, which are: uniform heat flux, uniform average borehole wall temperature, and uniform borehole wall temperature. The authors show that the uniform borehole wall temperature boundary condition is what was used by Eskilson (1987). Cimmino (2018b) also discusses applying uniform or non-uniform inlet fluid conditions to determine the temperature response of boreholes in mixed parallel or series connections.

Given that this work presents the first such study treatment of the subject, the uniform heat flux boundary condition will be applied and used. The uniform heat flux assumption combined with the finite line source method has been shown Malayappan and Spitler (2013) to give reasonable accuracy when the GHE is not too densely packed. In this case, the authors showed an error of 5% when the boreholes were spaced at 5 m. Additionally, the uniform heat flux method is comparatively easy to implement, and so we have selected it to calculate the cross g-functions.

The method used here is the method outlined by Marcotte and Pasquier (2009), which discretizes each borehole into a series of point-sources based on the model by Ingersoll et al. (Ingersoll and Plass, 1948; Ingersoll et al., 1951, 1954). An implementation of this model is also given in Grundmann (2016). The model assumes that the heat flux is uniform along the length of the borehole and that the ground temperature is constant with depth and time. The point-to-point response from each point to all other points is then determined, which gives the average borehole wall temperature response of the GHE. The average borehole wall temperature is computed as shown in Equation 4.7.

$$\Delta T_W(t) = \sum_{i=1}^N \frac{H_i}{H_{tot}} \sum_{j=1}^N \Delta T_{j \rightarrow i}(t) \quad (4.7)$$

$\Delta T_W(t)$ represents the mean variation in the temperature of borehole i due to interaction with borehole j . This is computed as shown in Equation 4.8.

$$\Delta T_{j \rightarrow i}(t) = \frac{q_j}{4\pi k H_i} \left(\int_{u_1^i}^{u_2^i} \int_{u_1^j}^{u_2^j} \frac{\operatorname{erfc}\left(\frac{d(u_i, u_j)}{2\sqrt{\alpha t}}\right)}{d(u_i, u_j)} - \frac{\operatorname{erfc}\left(\frac{d(u_i, u'_j)}{2\sqrt{\alpha t}}\right)}{d(u_i, u'_j)} du du' \right) \quad (4.8)$$

Where:

$$u_n = (x_n, y_n, z_n) \quad (4.9)$$

$$u'_n = (x'_n, y'_n, z'_n) \quad (4.10)$$

$$d(u_i, u_j) = \sqrt{(x_i - x_j)^2 + (y_i - y_j)^2 + (z_i - z_j)^2} \quad (4.11)$$

$$d(u_i, u'_j) = \sqrt{(x_i - x'_j)^2 + (y_i - y'_j)^2 + (z_i - z'_j)^2} \quad (4.12)$$

In order to account for the semi-infinite ground, each borehole is also mirrored about the ground surface to generate an imaginary borehole which has the opposite heat flux. Combining Equations 4.4, 4.7, and 4.8, g-functions can be computed as shown in Equation 4.13.

$$g = \frac{1}{2H_{tot}} \sum_{i=1}^N \sum_{j=1}^N \left(\int_{u_1^i}^{u_2^i} \int_{u_1^j}^{u_2^j} \frac{\operatorname{erfc}\left(\frac{d(u_i, u_j)}{2\sqrt{\alpha t}}\right)}{d(u_i, u_j)} - \frac{\operatorname{erfc}\left(\frac{d(u_i, u'_j)}{2\sqrt{\alpha t}}\right)}{d(u_i, u'_j)} du du' \right) \quad (4.13)$$

As applied to the computation of self- and cross-g-functions, this can be seen in Equations 4.14 and 4.15, respectively. $N_{bh,A}$ represents the number of boreholes in GHE A , and $N_{bh,B}$ represents the number of boreholes in GHE B .

$$g_{A \rightarrow A} = \frac{1}{2H_{A,tot}} \sum_{i=1}^{N_{bh,A}} \sum_{j=1}^{N_{bh,A}} \left(\int_{u_1^i}^{u_2^i} \int_{u_1^j}^{u_2^j} \frac{\operatorname{erfc}\left(\frac{d(u_i, u_j)}{2\sqrt{\alpha t}}\right)}{d(u_i, u_j)} - \frac{\operatorname{erfc}\left(\frac{d(u_i, u'_j)}{2\sqrt{\alpha t}}\right)}{d(u_i, u'_j)} du du' \right) \quad (4.14)$$

$$g_{B \rightarrow A} = \frac{1}{2H_{A,tot}} \sum_{i=1}^{N_{bh,A}} \sum_{j=1}^{N_{bh,B}} \left(\int_{u_1^i}^{u_2^i} \int_{u_1^j}^{u_2^j} \frac{\operatorname{erfc}\left(\frac{d(u_i, u_j)}{2\sqrt{\alpha t}}\right)}{d(u_i, u_j)} - \frac{\operatorname{erfc}\left(\frac{d(u_i, u'_j)}{2\sqrt{\alpha t}}\right)}{d(u_i, u'_j)} du du' \right) \quad (4.15)$$

Numerical integration has been performed using Simpson's formula (Moin, 2010). Also, keep in mind that the time scale for the self- and cross-g-functions are based on the average length of boreholes in GHE A as is shown in Equation 4.16.

$$t_{s,A} = \frac{H_{A,ave}^2}{9\alpha_s} \quad (4.16)$$

4.4 Validation

The self- and cross-g-functions described here will have some key properties which should be present in order to determine whether the methods outlined previously are valid. These properties are first given, then demonstrated by example.

Key Properties

1. *Intermodel Equivalence:* Self-g-functions computed using this method should be equivalent to self-g-functions computed using other methods.
2. *Combined Effect:* The combined effect of any number of GHE which are operated together using self- and cross-g-function methods must be equivalent to the effect of a single GHE which is operated alone that has a configuration equal to the separate GHE.
3. *Reciprocal Effect:* For any two GHE, A and B , the effect of A on B must be symmetrical to the effect of B on A for the same total heat load.

The first property is simply an intermodel comparison between this method and other, validated methods for computing g-functions. To perform this validation, the methods outlined in Cimmino (2018a) will be used. These methods have already been validated against the Eskilson (1987) g-functions, and the code has already been made available by Cimmino (2018c). The code used for computing the self- and cross-g-functions has been implemented in a C++ library and is published here: <https://github.com/mitchute/gfunction>.

To validate the second and third properties, several GHE will be considered as individual GHE and as a combined GHE. First, we will take a 2×2 rectangular GHE and decompose it into two, 1×2 GHE as is shown in Figure 4.1. The 1×2 GHEs are labeled A and B , and the original 2×2 borehole rectangular GHE is labeled GHE C .

The self- and cross-g-functions for the 1×2 borehole GHE A and the reference g-functions as computed by the pygfunction library can be seen in Figure 4.2. The self-g-functions for GHE A compares well against the 1×2 borehole g-functions generated using the pygfunction library. This demonstrates the first key property. The cross-g-functions showing the effect of GHE B on GHE A are also shown for reference.

Validation of the second property can be seen in Figure 4.3. To demonstrate this

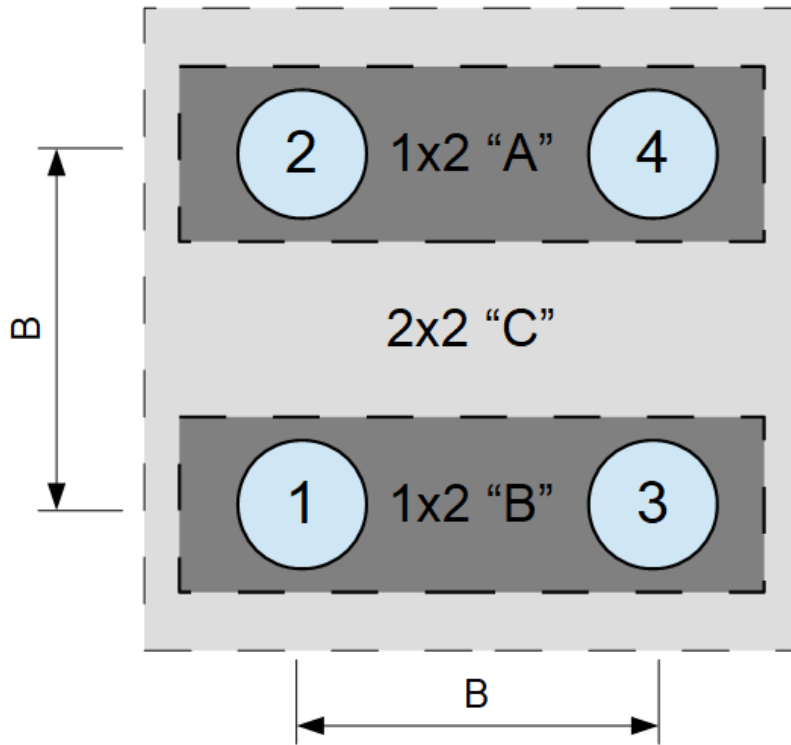


Figure 4.1: Fields, A , B , and C used for validation purposes

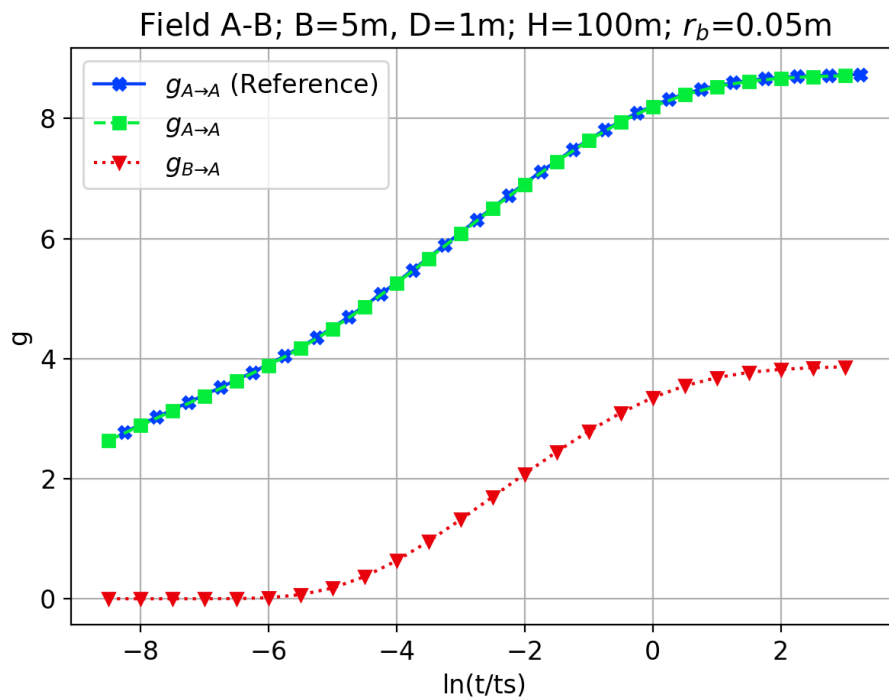


Figure 4.2: GHE A and B self- and cross-g-functions validated against the pyfunction library.

property, we need to show that the combined effect of both GHE A and B when operated together is equivalent to the effect of GHE C when operated alone. In other words, the temperature response computed by Equations 4.3 and 4.6 should be equivalent if the same heat loads were applied to both GHE simultaneously. Looking at Equation 4.6, if the heat loads are equivalent we can easily show that Equation 4.3 can be recreated by simply summing the self- and cross-g-function values within the summation convolution. As a result of this, we expect the self- and cross-g-functions to sum to the value of self-g-functions for the combined GHE. This is shown for GHE A , B , and C in Figure 4.3.

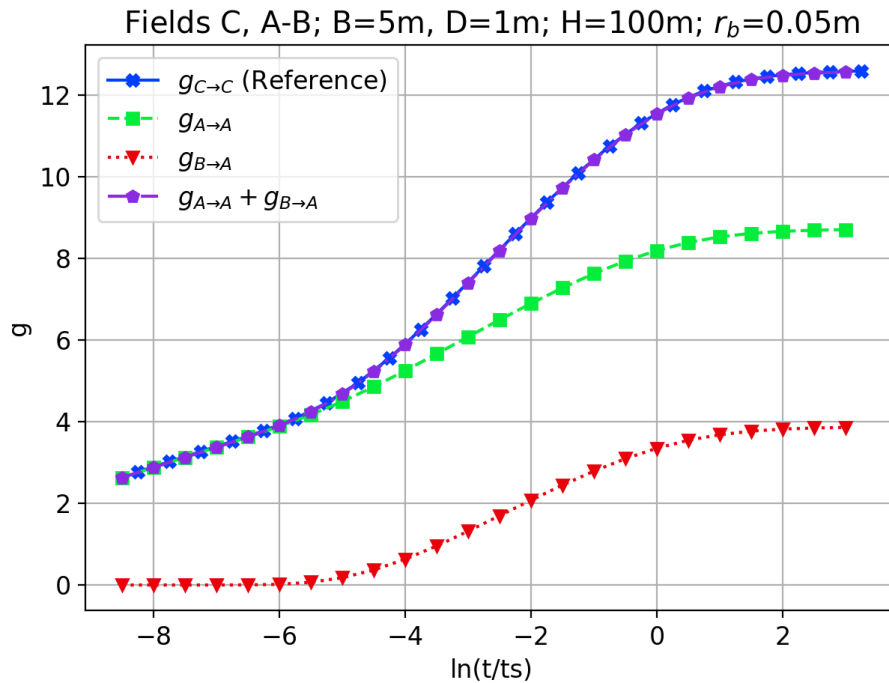


Figure 4.3: Self- and cross-g-functions for GHE A and B , and self-g-functions for GHE C

The third property, which is the reciprocal property, relates back to fundamental thermodynamic theory. Formally, the reasoning for this relates back to Onsager's Noble Prize winning works (Onsager, 1931a,b) on the subject where reciprocal relations for irreversible thermodynamics are described. More recently, though, Mazur (1997) gives a more tractable discussion of the topic where the author describes the previous

works by Duhamel, Stokes, Thomson (Lord Kelvin), Helmholtz, and others who all attempted to prove, either by theory or experimentation, that the heat conduction tensor should have symmetric properties.

From an energy balance perspective, the energy transferred from one GHE to another must be conserved and symmetrical, regardless of which GHE is the “self” GHE and which is the “cross” GHE (Equation 4.17).

$$E_{A \rightarrow B} = E_{B \rightarrow A} \quad (4.17)$$

In order to validate the third property, the 2×2 GHE C is decomposed in a different manner to form a single-borehole GHE and a 2×2 L-shaped GHE, labeled D and E , respectively. This is shown in Figure 4.4.

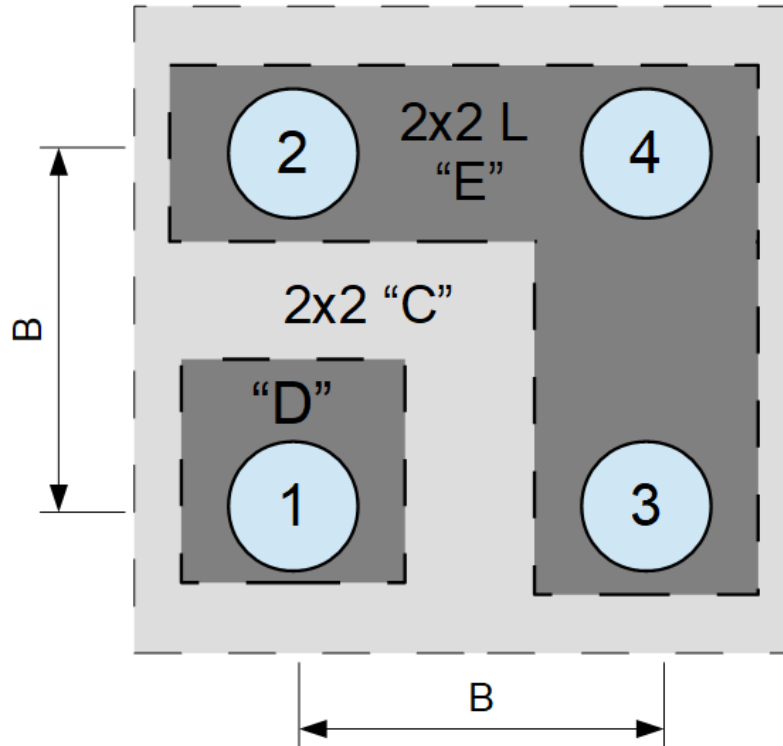


Figure 4.4: Single borehole GHE D and 2×2 L-shaped borehole GHE E

The resulting self- and cross-g-functions for the case when GHE D is considered the self-GHE is given in Figure 4.5. Self- and cross-g-functions for when GHE E is

considered the self-GHE is given in Figure 4.6. In both figures, the reference data for the combined GHE C are given. Again, in both figures we see that the second property is satisfied by the sum of the self- and cross-g-function values being equivalent to the g-function value for GHE C .

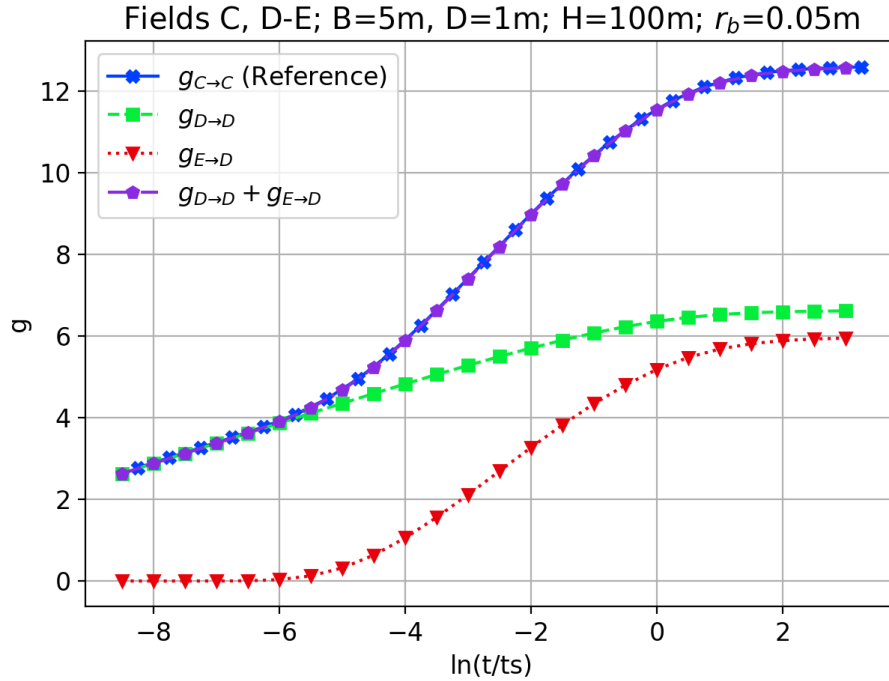


Figure 4.5: GHE D self- and cross-g-functions

In order to validate the energy balance effects for the third property, we will setup a simple example. Table 4.1 shows some example calculations to show the effect of GHE E on GHE D . Lets assume a total heat input rate of 1 kW to GHE E , which has three 100 m boreholes. This gives the normalized heat input rate as $3.3\bar{3}$ W/m. For the sake of this example, let us take an example cross-g-function value, $g_{E \rightarrow D}$, at $\ln t/t_s = 3$, which is ≈ 6 . And lets also assume that the effective soil thermal conductivity, $k^* = 2.5$ W/(mK). The result is that the temperature rise of the self-GHE from the cross-GHE is about 1.27°C for a constant heat pulse taken at $\ln t/t_s = 3$ after applying Equation 4.1.

A similar example computation can be made for the effect of GHE D on E . These

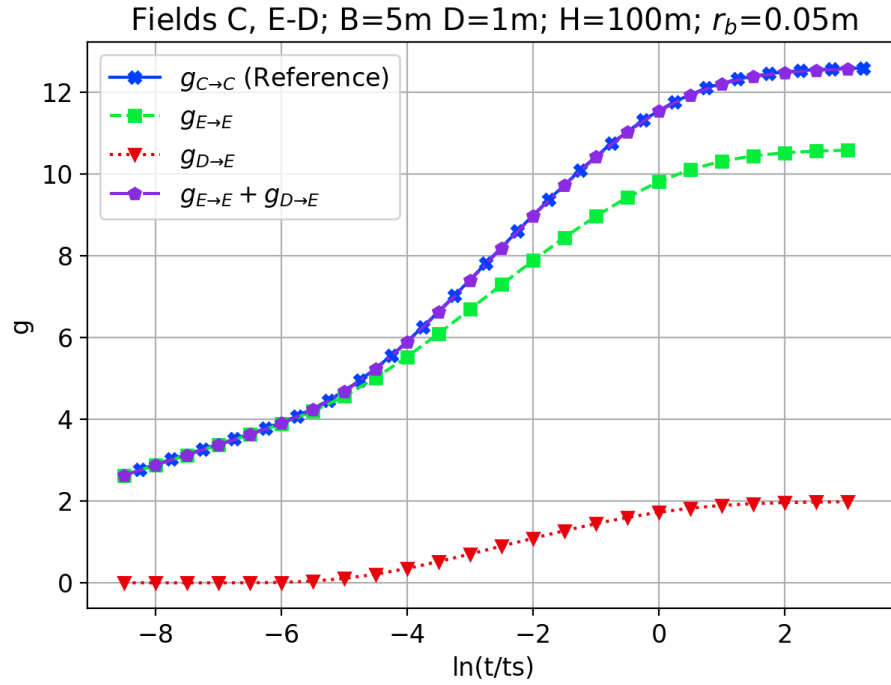


Figure 4.6: GHE E self- and cross-g-functions

Table 4.1: Calculations for the effect of GHE E on GHE D

| Q_E | $H_{E,tot}$ | q_E | $g_{E \rightarrow D}$ | $\Delta T_D = q_E \cdot g_{E \rightarrow D} / 2\pi k^*$ |
|-------|-------------|----------|-----------------------|---|
| 1 kW | 300 m | 3.33 W/m | ≈ 6 | 1.27 °C |

computations are shown in Table 4.2. Again, the GHE D has a total heat input rate of 1 kW. This GHE has a single, 100 m borehole. The normalized heat input rate is 10 W/m, and the example cross-g-function value, $g_{D \rightarrow E}$, at $\ln t/t_s = 3$, is ≈ 2 . Again, the temperature rise of the self GHE from the cross GHE is about 1.27 °C for a constant heat pulse taken at $\ln t/t_s = 3$.

Table 4.2: Calculations for the effect of GHE D on GHE E

| Q_D | $H_{D,tot}$ | q_D | $g_{D \rightarrow E}$ | $\Delta T_E = q_D \cdot g_{D \rightarrow E}$ |
|-------|-------------|--------|-----------------------|--|
| 1 kW | 100 m | 10 W/m | ≈ 2 | 1.27 °C |

In both examples, the effect of the cross-GHE on the self-GHE have been shown to have the same effect for the same *total* energy input rate. For clarity, this is not the heat input rate normalized by total borehole length.

Because of this reciprocal property, the following reciprocal relation must apply, which occurs due to the way in which the cross-g-functions were derived which normalizes them by the total length the self-GHE. Note that this is similar to the view factor relations which are used for radiation heat transfer.

$$g_{A \rightarrow B} H_{B,tot} = g_{B \rightarrow A} H_{A,tot} \quad (4.18)$$

4.5 Application Methods

In order to test the application of the cross-g-function methodology for computing the effects of GHE interactions, we will first set up some test cases then analyze the results. These test cases will involve a simulating a ground source heat pump system (GSHP) for a typical Swedish home which uses one or more boreholes to provide heating and for domestic hot water generation. The individual systems, loads, and systems models are all described here. Specific test cases showing the estimated long-term effects of neighboring GHE will be given in the next section.

4.5.1 Borehole

Scandinavian countries typically use water-filled boreholes due to the hard rock geology found in the region. These boreholes also generally use a single-loop U-tube which is suspended within the borehole. Juhlin and Gehlin (2017) have shown from a survey of the Swedish well database that average GHE depth is increasing, but boreholes with an active length of 150 m are common. Due to this, the borehole used in this study has an active length of 150 m.

Generally, the top of water-filled boreholes do not exchange energy with the soil because it is above the water table. This distance can fluctuate for various reasons, but will be set at 5 m for this study. Water-filled boreholes typically have a thermal resistance of $0.07 \text{ K}/(\text{W}/\text{m})$ (Gustafsson and Gehlin, 2008); however the borehole model used for this study was developed for grouted-boreholes. In order to emulate the performance of a water-filled borehole, the following borehole and soil parameters were used as shown in Table 4.3.

Table 4.3: Borehole configuration parameters

| | |
|------------------|-----------------------------|
| k_s | 3.5 W/(m K) |
| $\rho_s c_{p,s}$ | 2.678 MJ/(m ³ K) |
| k_g | 3.5 W/(m K) |
| $\rho_g c_{p,g}$ | 4.2 MJ/(m ³ K) |
| d_b | 114 mm |
| $d_{p,o}$ | 40 mm |
| $d_{p,i}$ | 34.91 mm |
| k_p | 0.39 W/(m K) |
| $\rho_p c_{p,p}$ | 1.8 MJ/(m ³ K) |
| s | 51.33 mm |

Soil parameters are taken from Spitler et al. (2014). U-tube pipe shank-spacing, s , was set so the pipes were evenly spaced between each other and the borehole wall. The mass flow rate was set to $0.466 \text{ kg}/\text{s}$. At 20°C using 25% by mass ethanol-water antifreeze mixture, the borehole resistance was computed to be approximately $0.07 \text{ K}/(\text{W}/\text{m})$.

4.5.2 Building Loads

The building used in this study is a typical Swedish single family house, which is a renovated 1940s-era house in Stockholm. The building is a 125 m² building which uses a hydronic radiator panel heating system. The building data is taken from the TABULA database (www.building-typology.eu) and the hourly building heating loads are estimated with the building simulation program EnergyPlus (Gehlin and Spitler, 2014a). The Stockholm outdoor environment conditions were taken from the Stockholm, Arlanda IWEC weather file (DOE, 2018). The annual building heating loads and the outdoor air temperature are plotted in Figure 4.7. The domestic hot water (DHW) loads were taken from measured data measured from a Swedish home (Nordman, 2014). The DHW loads data are plotted in Figure 4.8.

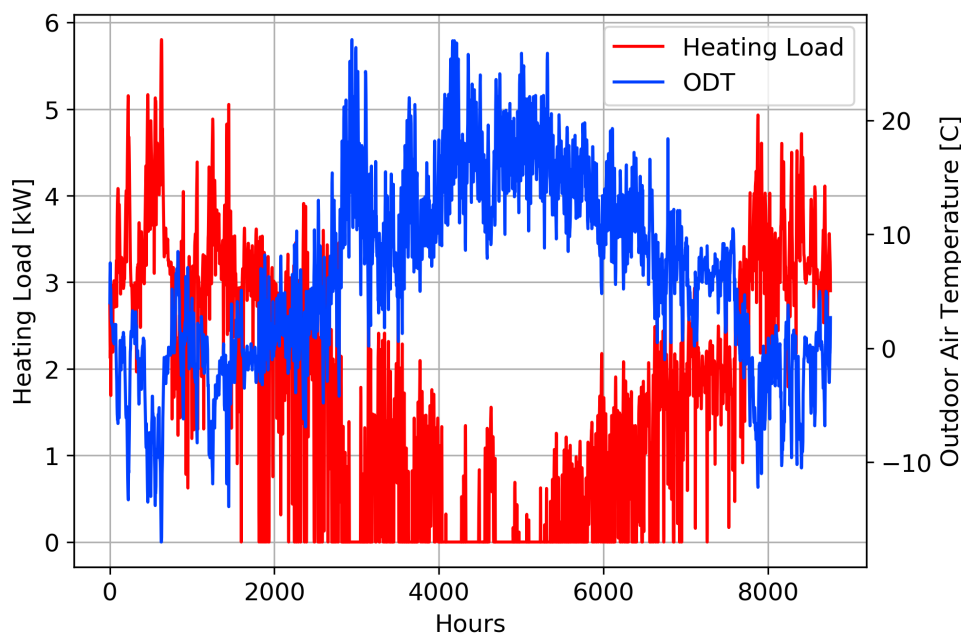


Figure 4.7: Space heating load profile and outdoor air temperature

4.5.3 Heat Pump Model

The heat pump model used is the same heat pump model developed and described by Gehlin and Spitler (2014b), which was also used by Gehlin and Spitler (2015). The

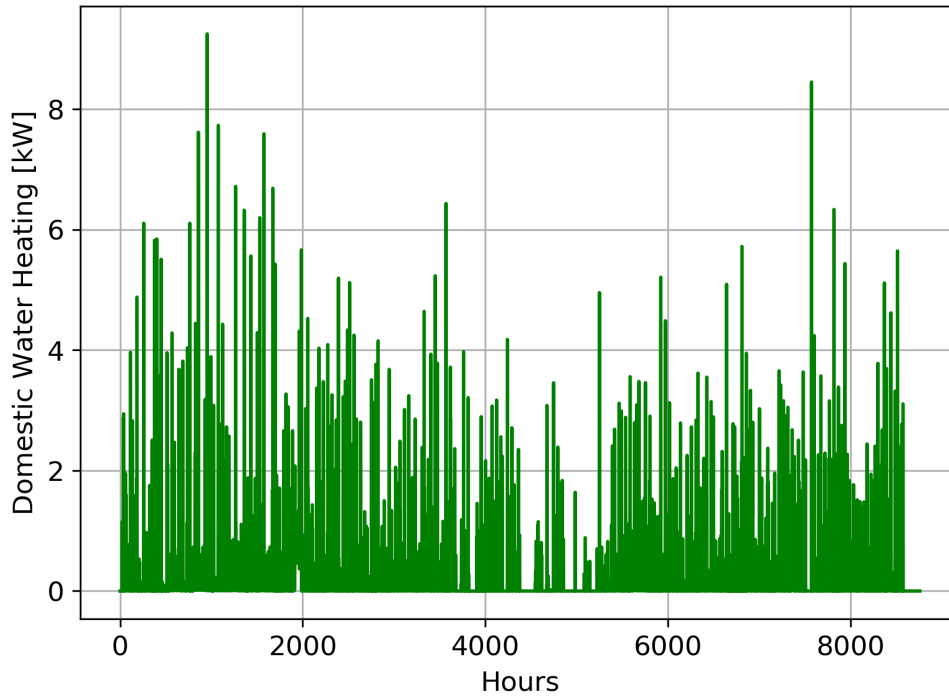


Figure 4.8: Domestic hot water loads

heat pump and model descriptions are given again here for clarity.

The heat pump model used is typical for a Scandinavian single family home, and different from typical North American heat pumps. These differences are outlined below:

- Not reversible — the heat pump is used to provide heating only.
- Water-to-water — typical Scandinavian homes distribute heat through radiators which are distributed throughout the building, or with a hydronic heating system.
- Integrated domestic hot water generation and storage — a double wall water storage tank is integrated into the heat pump to provide for domestic hot water usage. The tank stores around 160-200 liters of hot water, which is heated by the hot water generated by the heat pump. A three-way valve directs the hot water generated by the heat pump either to the radiators for space heating or to the hot water tank. Desuperheaters are not typically used.

- Electric resistance backup heater — an electric resistance heater is used to provide supplemental heating capacity when the heating load exceeds the heat pump heating capacity.
- Heat pump set point partially based on outdoor air temperature — the heat pump controls are proprietary, but it does have a control curve which sets the fluid temperature going to the radiators based on the outdoor air temperature. The effect of this is that the heating set point is lowered when the outdoor air temperature is higher, which results in an increased heat pump COP. The hot water tank set point is user-defined, and domestic water heating is given priority over space heating.
- Quasi-stead-state model — the model neglect dynamics and assumes that that domestic hot water loads that occur in any given hour are met.

A schematic of how the heat pump and heating systems are configured is seen in Figure 4.9.

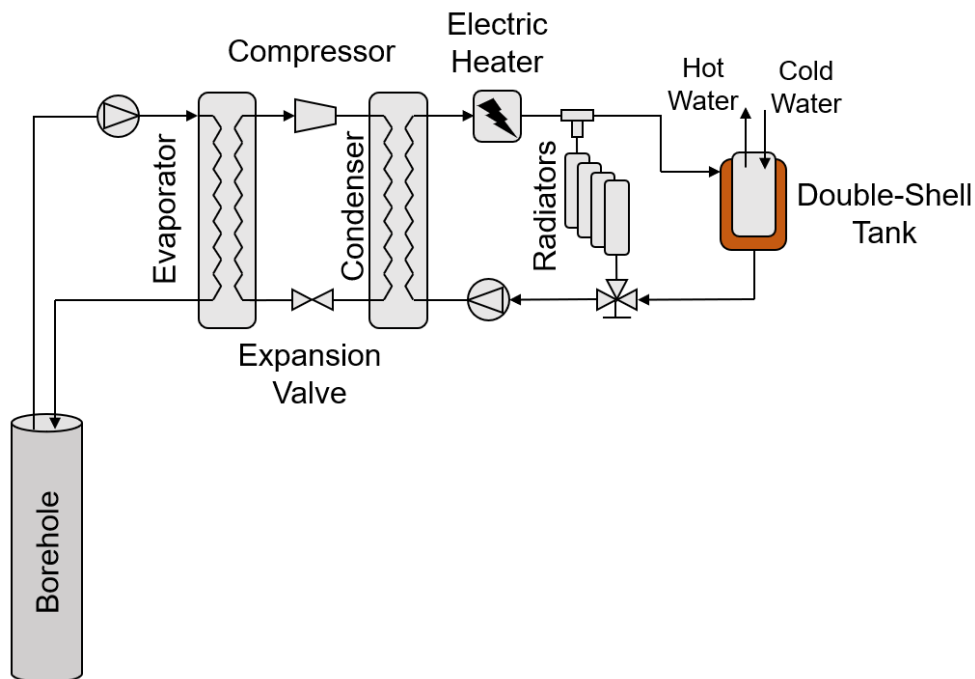


Figure 4.9: Heat pump schematic, recreated after Gehlin and Spitler (2014b)

The heat pump has a nominal heating capacity of 7 kW and the electrical immersion heater has a heating capacity of 7 kW. Heat pump heating capacity and COP are computed based on polynomial equations fit to manufacturer operation data using generalized least squares approach. The generalized polynomial is given in Equation 4.19, and coefficients are given in Table 4.4. $T_{f,out,load}$ is the circulating fluid temperature exiting the condenser; i.e. the load-side exiting fluid temperature, which is the fluid supplied to the hot water tank or the radiators. $T_{f,in,src}$ is the fluid temperature entering the evaporator from the GHE; i.e. the source-side entering fluid temperature.

$$\text{COP or } Q_{HP} = c_1 + c_2 \cdot T_{f,out,load} + c_3 \cdot T_{f,out,load}^2 + c_4 \cdot T_{f,in,src} \quad (4.19)$$

Table 4.4: Capacity and COP heat pump polynomial coefficients

| | c_1 | c_2 | c_3 | c_4 |
|----------|--------|--------------------------|--------------------------|-------------------------|
| Q_{HP} | 8.5367 | -7.2667×10^{-3} | -8.4×10^{-4} | 2.6367×10^{-1} |
| COP | 7.6418 | -7.5098×10^{-2} | -2.0844×10^{-4} | 1.0942×10^{-1} |

4.5.4 Pumping

No pumping model is utilized since the heat gain due do pumping energy losses in heating-dominated applications will not be as important an issue as it would be for a cooling-dominated application. Therefore, it is neglected.

The circulation fluid flow rate through the borehole and heat pump source side is set at a constant value of 0.466 kg/s. The study performed by Gehlin and Spitler (2015) discusses significant energy savings being associated with systems which have a significant number operation of hours with laminar flow. At 20 °C with 25% by mass ethanol-water antifreeze mixture, this flow rate resulted in a Reynolds number of approximately 6,000. However, since heat is being extracted from the system the temperatures be lower. This will result in flows with lower Reynolds numbers. Reynolds numbers for this study typically varied from about 3,000–4,000.

4.5.5 Ground Heat Exchanger Model

The ground heat exchanger used is described in Chapter 3. To apply this model, the second row of Equation 4.6 is included in the Equation 3.1 to compute the cross-effects. A start time parameter is also included in this term so that the cross-effects can be started at a time after the simulation begins. For simulation times less than this start time, the effect will be 0. For times after the start time, the cross effects will be computed as described previously.

4.6 Case Study

This case study will focus on determining the effects of neighboring GSHP systems installed at the same time or after original (self-) system has been installed and operated. The results will be compared against the simulation where no neighboring GHE effects are accounted for.

For this study, we will assume that an identical neighboring system has been installed at various distances, B , away from our system. Each system has one borehole identical to the one described previously as is shown in Figure 4.10. This distance will be set to 10 m, 15 m and 20 m.

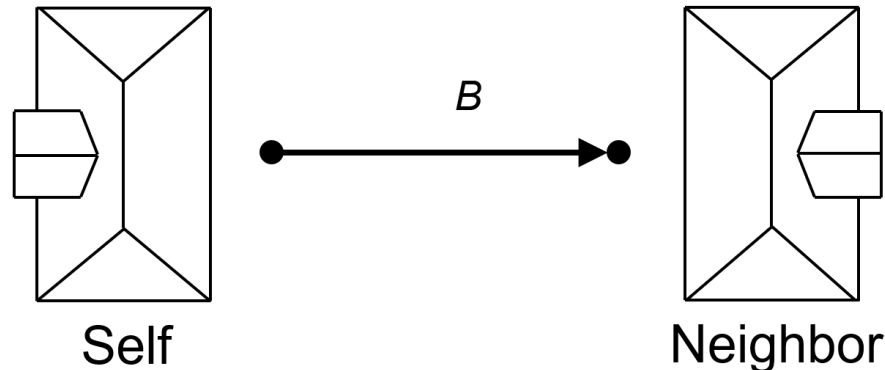


Figure 4.10: Neighborhood arrangement

The GHE loads for the neighbor systems were determined from performing an annual simulation of the self-system using the GHE and heat pump models with the

given heating and domestic hot water loads given previously. The resulting ground heat exchanger load determined was then applied each year for which the cross-system is operating. Effects of the self-system on the cross-system are not considered in this study. Multiple cross systems are also not simulated, however for the simplest case where the effects of multiple systems on each other are not considered, the effect can be easily determined since superposition can be applied.

This study represents an extreme, worst-case scenario. This is due to the relatively small borehole spacing which is applied and by not considering the effects of the self-system on the cross-systems or the effects of the cross-systems on each other. As the soil becomes colder, the heat pump is expected to operate with a lower COP, which results in less energy being extracted from the ground and more energy being used from the supplemental heater. Future studies should consider all of these variables together simultaneously. Additionally, the system operates with a highly imbalanced load. No space cooling is provided, so no heat is rejected to the soil during summer months. This also have a worsening effect on the problem.

Figure 4.11 shows the g-function values computed for this case. Some dimensional time values have also been given which help with understanding the time scale and how it relates to the current study. For this study, the cross-system effects are started at the same time as the self-system. Another set of simulations were run with the cross-system effects being delayed by 5 years, and then beginning normal operation.

In Figure 4.11, the dimensional time values are given when the cross-effects begin to be non-zero, and at the end of the simulation. The self-system simulation was operated for 20 years, with the cross-systems being started as 0 and 5 year delays. Surprisingly, the cross effects begin to affect the self-system after as little as 0.5 yr, as indicated in the figure.

Figure 4.12 shows two days of operation during February 1–2 for the first year of operation for the self-system. Shown in the figure are the heat pump source side

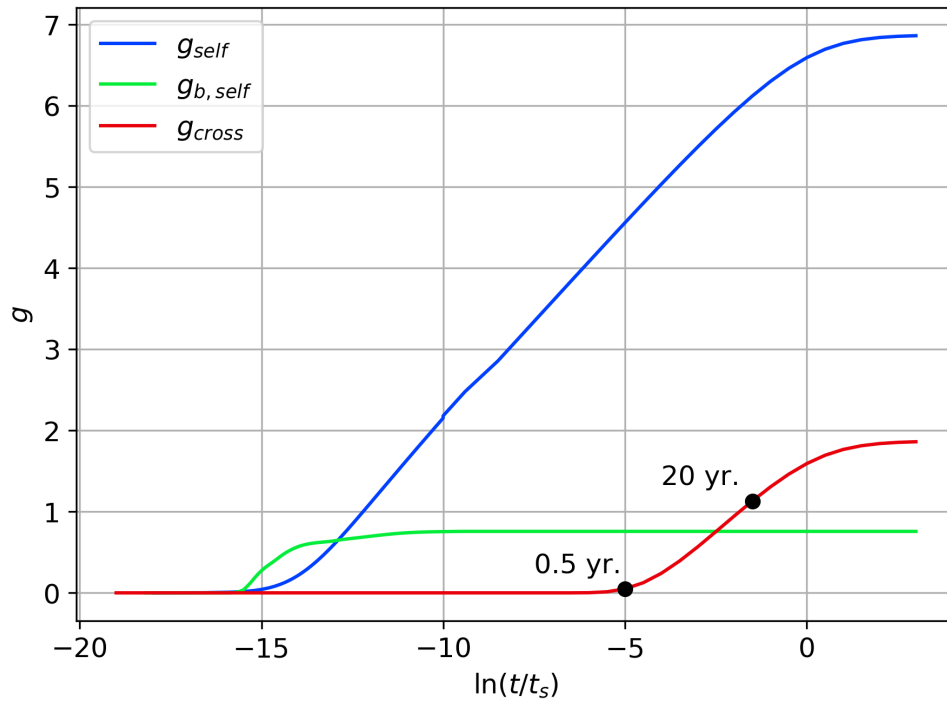


Figure 4.11: g-function values

entering and exiting fluid temperatures, the outdoor air temperature, as well as the space heating and water heating loads. As expected, the space heating loads decrease as the outdoor air temperature increases. Figure 4.13 shows the same variables, but plotted for July 1-2 for the self-system during the first simulation year.

Figure 4.14 shows the heat pump inlet temperature plotted for 20 years with no cross-system effects. Plotted are the hourly, monthly average, and annual average temperatures.

From the figure, we can see that as the system operates, the average temperatures tend to decrease. This decrease is more steep initially, but levels off after a few years of operation. This behavior is typical of a system with an imbalanced load profile. This system provides no space cooling so this is an extreme case. Nevertheless, the average reduction in temperature is still acceptable for the system to continue to operate, with an average temperature drop of about 0.8°C . Figure 4.15 shows the annual average heat pump entering fluid temperature again; however, the cross-effects

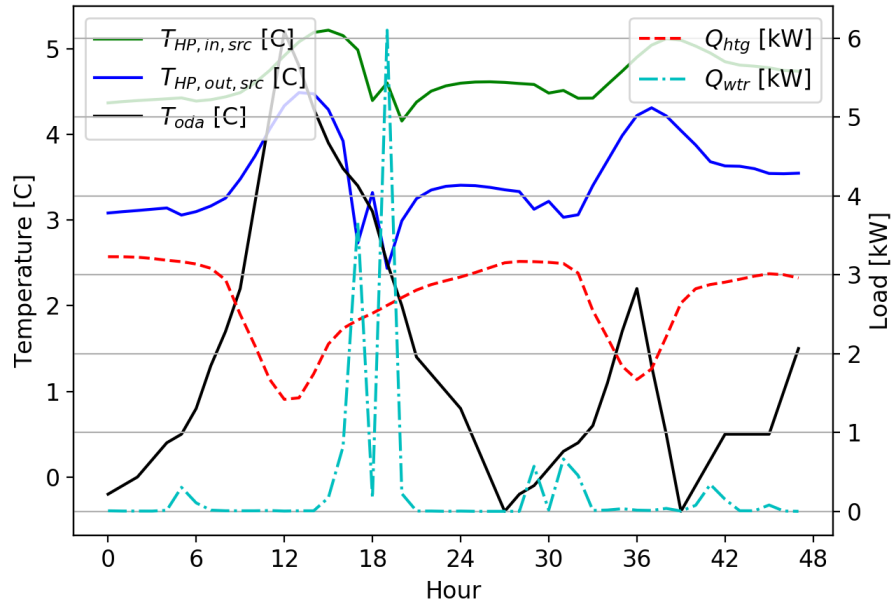


Figure 4.12: Temperatures and loads from February 1–2, year 1

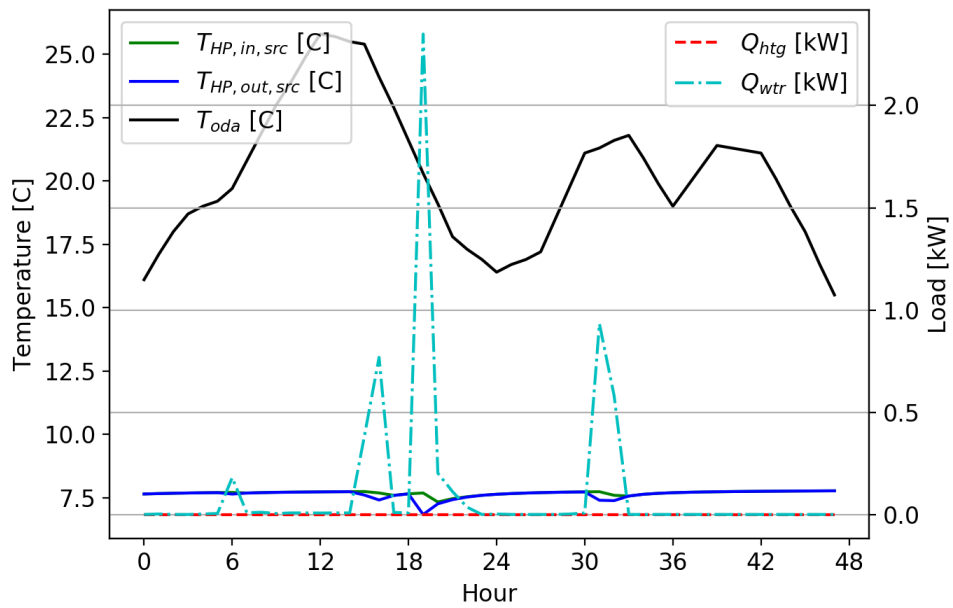


Figure 4.13: Temperatures and loads from July 1–2, year 1

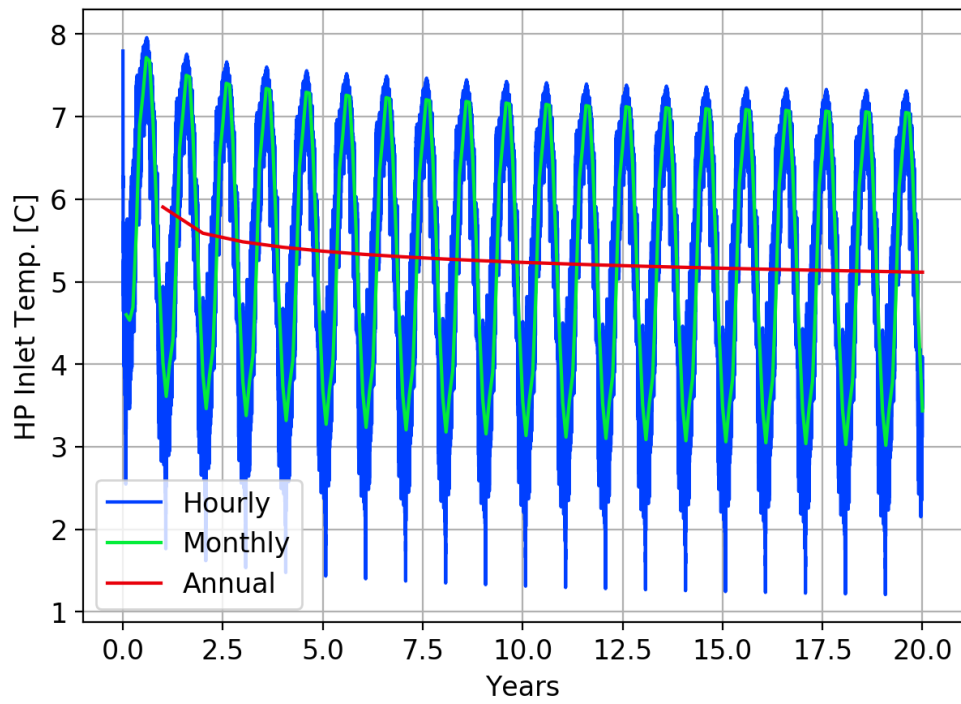


Figure 4.14: Hourly, monthly, and annual self-system heat pump inlet temperature from adding neighboring systems at 10, 15, and 20 m are also plotted.

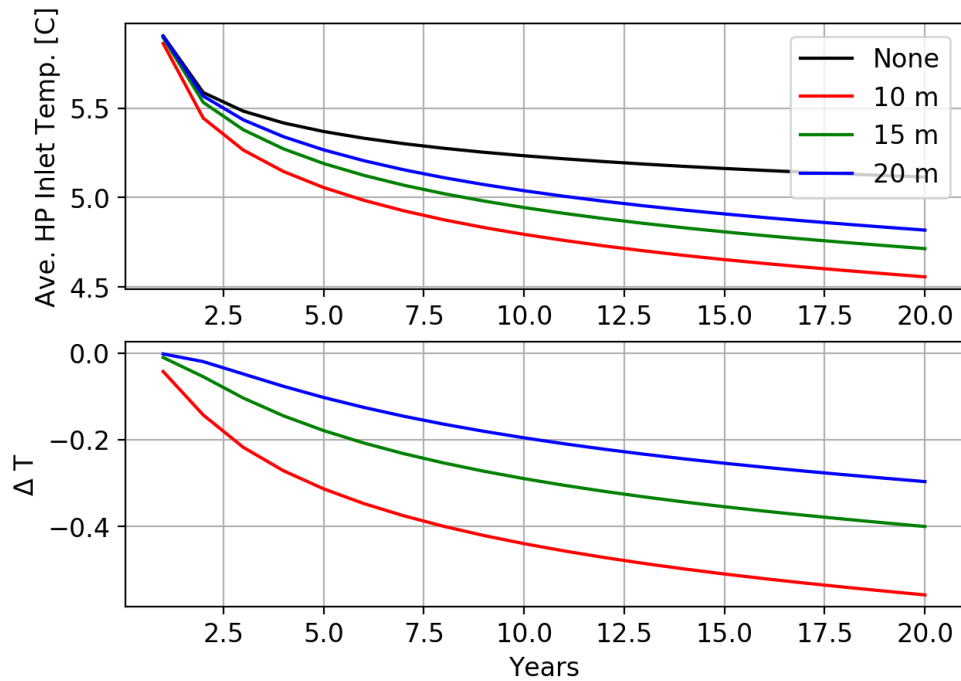


Figure 4.15: Annual self-system heat pump inlet temperature with cross-system effects

From the figure, we can see that instead of dropping approximately 0.8°C on average after 20 yr of operation, the heat pump inlet temperature drops by about 1.3°C when the effects of a system at a distance of 10 m are also considered. For neighboring systems spaced at 15 and 20 m, the 20-year average annual heat pump inlet temperature decreases by 1.2 and 1.1°C , respectively. For this simple worst-case scenario, the effects of adding additional systems could be determined by superposition of the results.

Figure 4.16 shows the annual heat pump coefficient of performance (COP), including the energy used to for the supplemental heating. Nordman et al. (2012) attempts to categorize the types of annual COP or seasonal performance factors (SPF). This could be categorized as SPF_{H3} however, the energy from the source-side circulation pump is not included. For this case study, the effects of a neighboring system at a spacing of 10 m results in an average annual decrease in COP by about 1.5% over the 20 yr. study. Note that this value is computed by summing the annual energy provided for heating and the energy used to operate the heat pump, and then computing COP by dividing the two. It is not the average of the hourly COP values. Some description of this procedure is given by Spitler and Gehlin (2019).

Figure 4.17 shows the heat pump's annual energy usage for the study. As expected, the heat pump uses more energy due to the decrease in performance. This increase in energy usage results in about 1.6% additional energy used when considering the effects of a neighboring system spaced at 10 m.

Figure 4.18 shows the annual energy extracted from the soil by the heat pump. Because the heat pump is performing more poorly, this value is also decreasing due to the cross-system effects. Since the heat pump is operating less efficiently, it is extracting less heat from the soil, and therefore more of the heating energy is being provided by the heat pump compressor work. We should note that for heating dominated systems, this may have a self-balancing effect. However, for cooling dominated

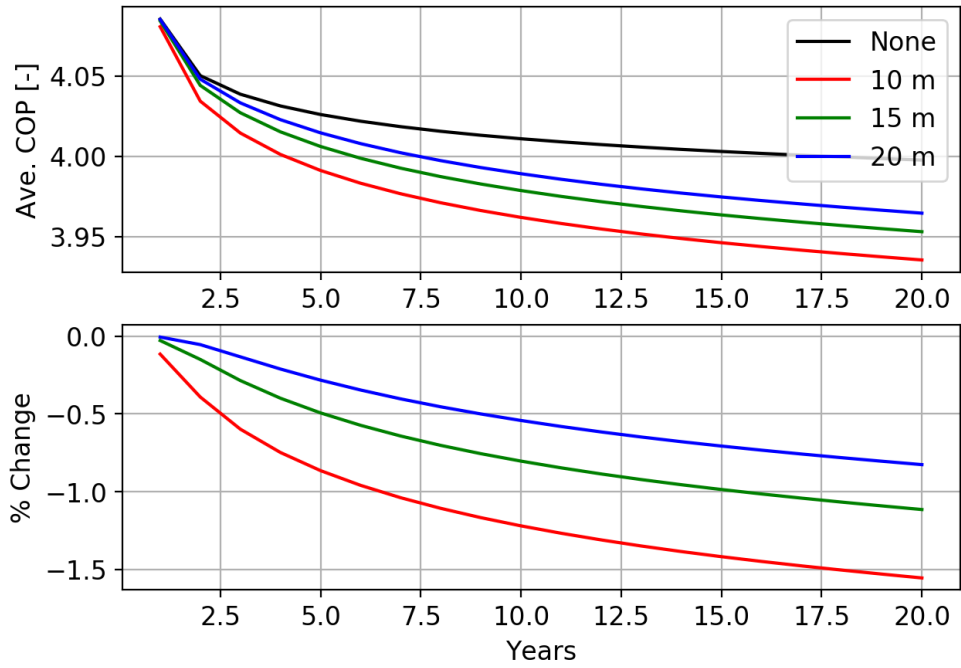


Figure 4.16: Annual average COP. Includes electric resistance heating.

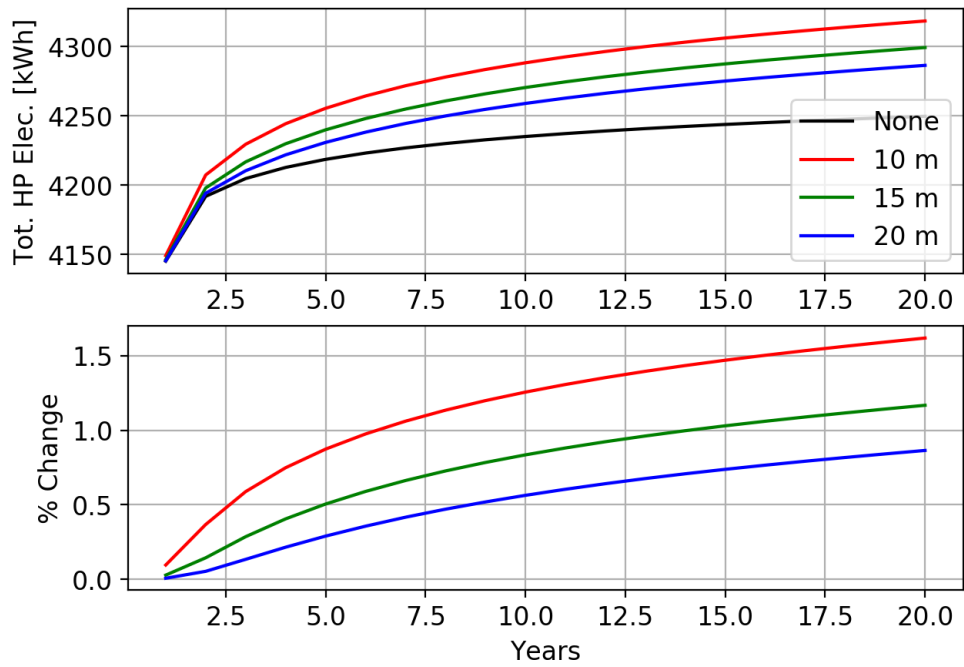


Figure 4.17: Annual heat pump energy usage

systems the opposite result will occur. Decreasing heat pump efficiency results in more energy be rejected to the soil, which in turn further results in poorer heat pump performance. This feedback loop is not self-balancing.

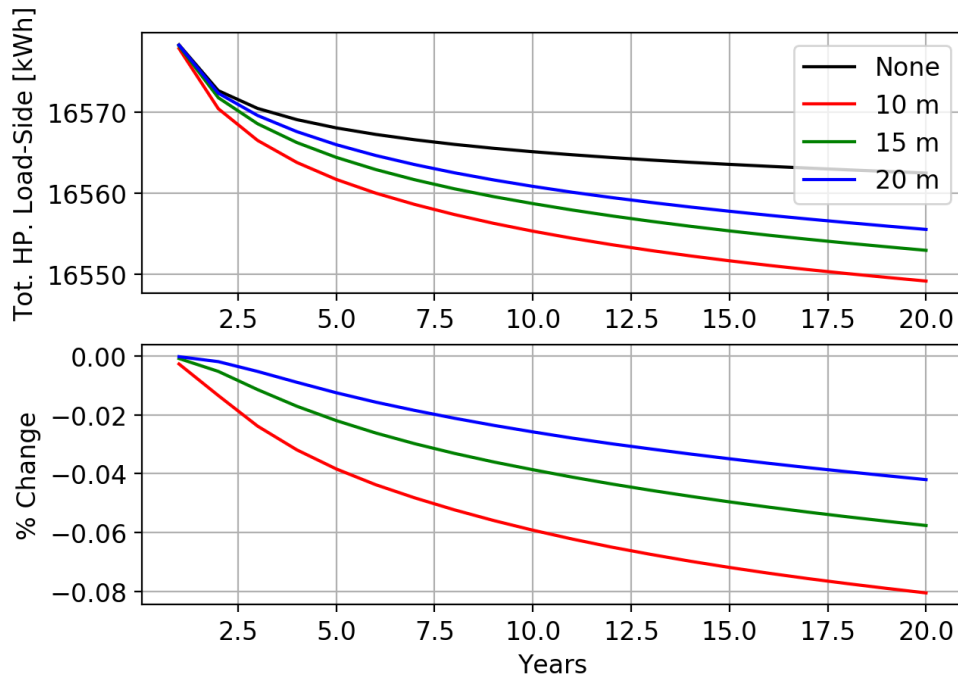


Figure 4.18: Annual heat pump energy extracted from the soil

Finally, the result of the decreasing heat pump inlet temperatures and declining heat pump performance results in an increase in the energy usage required from the supplemental heater. This is shown in Figure 4.19 where the supplemental heating increases by about 12%. However, when all of the total electrical energy usage is considered, the energy required to meet the heating loads increases by about 1.8% after 20 years. This can be seen plotted in Figure 4.20.

Figure 4.21 shows the total energy usage for the cross system effects starting at 5 years of operation. As expected, there is no change in energy usage for the first 5 years, after which the system performance begins to decrease as occurred when the systems started operation simultaneously. This behavior is typical of the other variables plotted and shown previously.

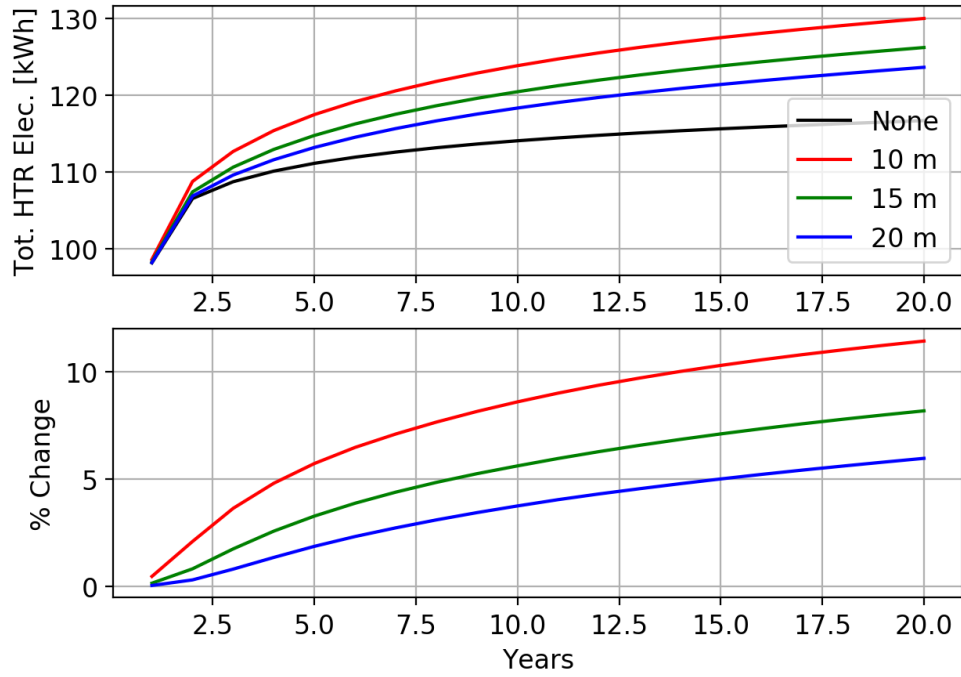


Figure 4.19: Annual resistance heating energy usage

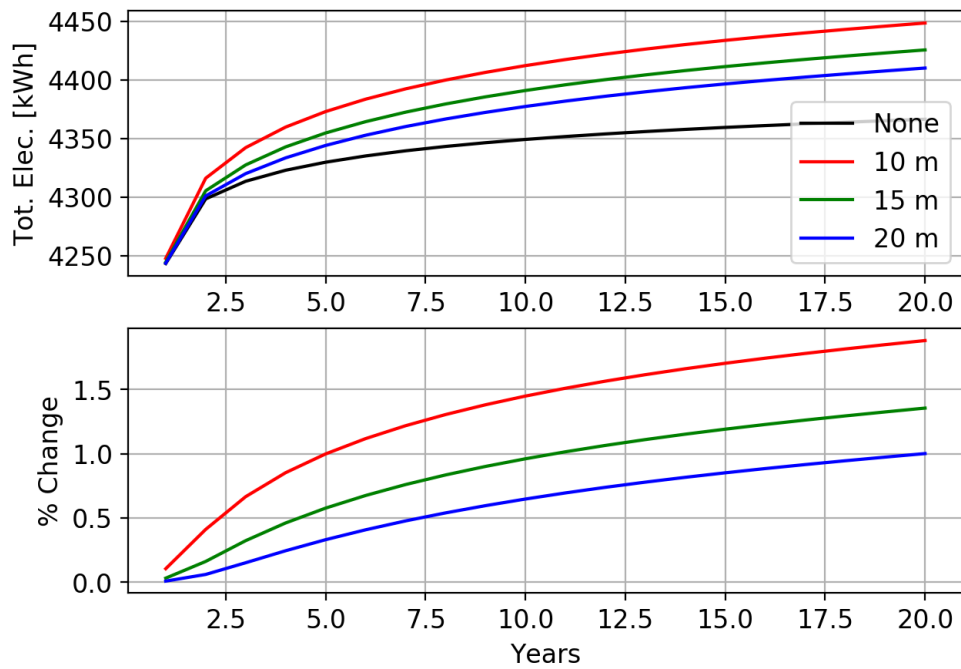


Figure 4.20: Annual heat pump and immersion heater electrical energy usage

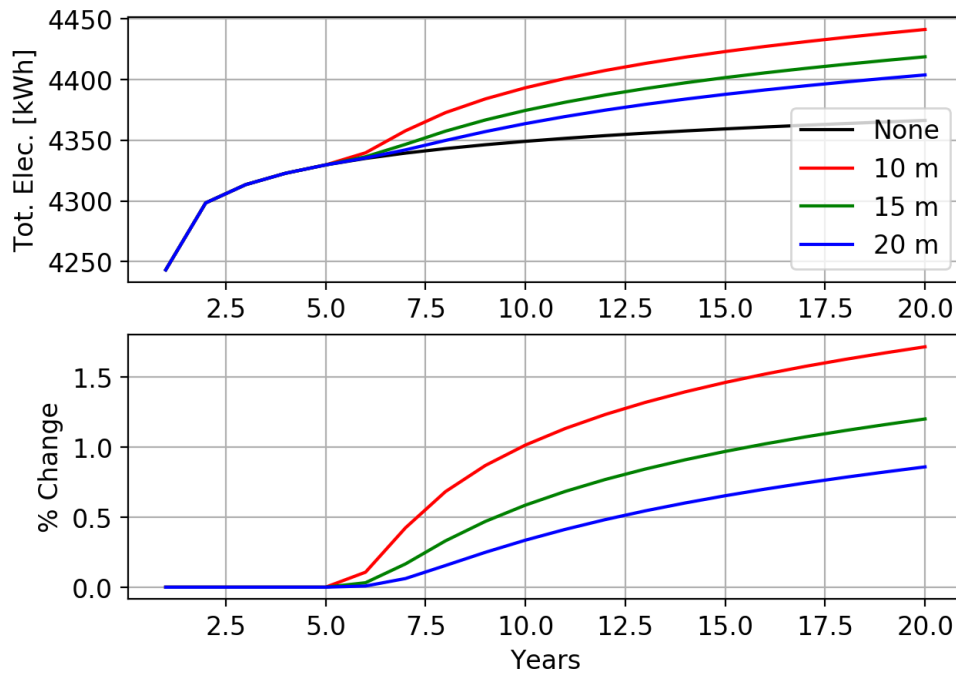


Figure 4.21: Annual heat pump and immersion heater electrical energy usage for cross-system effects starting at 5 years

4.7 Conclusions and Recommendations

This work has defined the concept of cross-g-functions and described how they are computed. The cross-g-function approach is validated and some expected properties are identified which the cross g-functions must possess. The method for computing cross-g-functions is then given, along with some examples demonstrating validation.

Next a case study is performed describing how the method is applied and used to examine the densely-packed residential GHE problem. System loads, a heat pump model, and the GHE are described. Finally, the study is performed by comparing the energy usage for a stand-alone system with no GHE interference from neighboring systems. The effects of neighboring systems are then considered and shown to increase annual energy usage by as much as 1.8% for a single system located 10 m away after 20 years of operation. For a system located at a distance of 20 m, the neighboring system effects cause an increase of about 1% after 20 years of operation.

The work described here presents some useful information regarding the application and methods, however, some key improvements should be made and additional case studies run to demonstrate the method's applicability. These are identified here.

- Pumping energy should be included in the computations since this is a significant factor in determining the overall system performance.
- Subsequent studies should include the effects of all systems on each other. The study presented represents an extreme, worst case scenario. However, the other systems will also have ground loads which decrease with time due to the thermal interaction of the systems. This may have a self-balancing effect when all systems are considered together.
- Further studies should consider some of the other test cases described in the introduction, especially with regard to changing the GHE design after a period of operation.

CHAPTER V

CONCLUSIONS

5.1 Summary

The primary focus of this work has been to develop an enhanced ground heat exchanger model (GHE) for use in whole building energy simulation (WBES). In Chapter 1, a thorough literature review was performed with regard to the all current and past GHE modeling methods and techniques. Next, modeling deficiencies were identified. Finally, objectives were defined discussing the desired GHE enhancements this work intended to make. These desired enhancements are summarized here.

1. First, the GHE models developed in this work were developed for use in WBES environments which prioritize low simulation runtime. Therefore, much of the focus of this work has been done with that in mind.
2. Second, the models developed were intended to improve the accuracy of GHE simulation in WBES. Current GHE WBES models produce non-physical behavior under certain conditions, and this was identified as a key deficiency that needed to be addressed.
3. Third, the models developed were intended to extend GHE modeling capabilities to non-standard configurations, which are common in practice. Some of these include modeling GHE with parallel flow paths, flow imbalances, GHE zoning, and GHE-to-GHE interactions.

Chapter 2 discusses load aggregation procedures which are used to reduce the number of computations required for response factor models. This work primarily

focuses on objective 1 and 2, as listed above. A large parametric study was run where the load aggregation methods were compared, and simulations run to characterize method performance. This primarily focused on objectives 1 and 2 as outlined above.

Chapter 3 discusses an enhanced response factor model for WBES. Using the new model, it was shown that accurate dynamic behavior can be simulated for GHE using response factor calculations. The results are shown to be accurate for time steps which are shorter than the GHE transit time, as well as long time steps. This primarily focused on objectives 2 and 3 as outlined above.

Chapter 4 defines and discusses the concept of cross-g-functions and described how they are computed and used to simulate thermal interaction between neighboring GHE. A case study was then performed describing how the method is applied and used to examine the densely-packed residential GHE problem. This primarily focused on objective 3 as outlined above.

5.2 Conclusions

A number of conclusions have been made from this work:

1. The dynamic load aggregation method proved to be better than the static load aggregation method. This is despite the dynamic method's dispersive and diffusive errors. Regardless, the method produces the best simulation results when the expansion rate is kept low and a reasonable number of bins were kept at each aggregation level. This study found a Pareto front of recommended configurations, but the recommended configuration has an expansion rate of 1.62 with the number of bins kept at each aggregation level at 9. It is not necessary to change the number of bins for each aggregation level.
2. GHE simulations which have short and long time steps can be performed by modifying the original WBES GHE model by including exiting fluid temperature g-functions. These ExFT g-functions account for the transit delays and

unequal heat transfer rate between the fluid and the borehole wall at short times steps.

3. ExFT g-functions can be generated with a relatively simple dynamic borehole model which includes a TRCM and two dynamic pipe models. The dynamic borehole model which was used was able to simulate the dynamic response including the transit delay effects for a multi-flow rate thermal response test. However, the pipe models used were not able to account for laminar flow, and thus the transit delay was over predicted. The simplified TRCM which was used was also shown to produce higher errors during low flow rates where short-circuiting effects are expected to be higher.
4. Simulation of GHE-to-GHE thermal interactions can be achieved with a new cross-g-function method. As expected, the effects of neighboring systems will effect the performance of other surrounding systems.

5.3 Future Work

5.3.1 Load Aggregation

- This work characterized the load aggregation method using the Python coding language. However, a mixture of efficient numerical library objects and native Python objects were used. This type of approach can result extra simulation time due to type-conversions between objects. Another followup study should be performed taking care to only use computationally efficient objects which minimize type-conversions. Though this may affect the final simulation time fraction of the recommended methods, the accuracy is not expected change, and therefore, the methods recommended are still expected to result in very good performance.

5.3.2 Enhanced GHE Model

- The current pipe model should be limited to turbulent-only flows. However, it is also applied for laminar flows. An appropriate model for laminar flow should be investigated and incorporated.
- A study should be performed to compare different TRCM for the objective of generating ExFT g-function values. Because computational speed is a high priority, other models and solution methods should be compared to determine which method and model gives the best balance of performance and accuracy.
- The dynamic borehole model should be extended for use with double U-tube and water filled boreholes.
- The model used to generate the short time step g-functions should be tested to see if an expanding time step could be used.

5.3.3 Cross-g-functions

- Pumping energy should be included in the computations since this is a significant factor in determining the overall system performance.
- Subsequent studies should include the effects of all systems on each other. The study presented represents an extreme, worst case scenario. However, the other systems will also have ground loads which decrease with time due to the thermal interaction of the systems. This may have a self-balancing effect when all systems are considered together.
- Further studies should be run to consider cooling load dominated situations.
- Future studies should consider some of the other test cases described in the introduction, especially with regard to changing the GHE design after a period of operation.

REFERENCES

- Acuña, J., Fossa, M., Monzó, P., and Palm, B. (2012). Numerically generated g-functions for ground-coupled heat pump applications. In *Proceedings of the COM-SOL Conference*, page 6, Milan, Milan.
- Al-Chalabi, R. (2013). Thermal resistance of u-tube borehole heat exchanger system: numerical study. Master’s thesis, University of Manchester, Manchester, UK.
- Al-Khoury, R. (2010). Spectral framework for geothermal borehole heat exchangers. *International Journal of Numerical Methods for Heat & Fluid Flow*, 20(7):773–793.
- Al-Khoury, R. and Bonnier, P. G. (2006). Efficient finite element formulation for geothermal heating systems—Part II: transient. *International Journal for Numerical Methods in Engineering*, 67(5):725–745.
- Al-Khoury, R., Bonnier, P. G., and Brinkgreve, R. B. J. (2005). Efficient finite element formulation for geothermal heating systems—Part I: steady state. *International Journal for Numerical Methods in Engineering*, 63(7):988–1013.
- Alberdi-Pagola, M. (2018). *Design and performance of energy pile foundations*. PhD thesis, Aalborg University, Aalborg, Denmark.
- Alberdi-Pagola, M., Jensen, R. L., Poulsen, S., and Erbs, S. (2018). Method to obtain g-functions for multiple precast quadratic pile heat exchangers. Technical Report 243, Aalborg University.
- Bauer, D., Heidemann, W., Müller-Steinhagen, H., and Diersch, H.-J. G. (2011).

- Thermal resistance and capacity models for borehole heat exchangers. *International Journal of Energy Research*, 35:312–320.
- Beier, R. A., Mitchell, M. S., Spitler, J. D., and Javed, S. (2018). Validation of borehole heat exchanger models against multi-flow rate thermal response tests. *Geothermics*, 71:55–68.
- Beier, R. A. and Spitler, J. D. (2016). Weighted average of inlet and outlet temperatures in borehole heat exchangers. *Applied Energy*, 174:118–129.
- Bell, I. H., Wronski, J., Quoilin, S., and Lemort, V. (2014). Pure and pseudo-pure fluid thermophysical property evaluation and the open-source thermophysical property library CoolProp. *Industrial & Engineering Chemistry Research*, 53(6):2498–2508.
- Bennet, J., Claesson, J., and Helström, G. (1987). Multipole method to compute the conductive heat flow to and between pipes in a composite cylinder. Technical report, University of Lund, Department of Building and Mathematical Physics, Lund, Sweden.
- Bernier, M. and Cauret, O. (2014). Modeling of short geothermal boreholes in series with experimental validation. In *11th IEA Heat Pump Conference*, Montréal, QC, Canada. International Energy Agency. May 12–16.
- Bernier, M. A. (2001). Ground-coupled heat pump system simulation. *ASHRAE Transactions*, 107(1):605–616.
- Bernier, M. A., Pinel, P., Labib, R., and Paillot, R. (2004). A multiple load aggregation algorithm for annual hourly simulations of GCHP systems. *HVAC&R Research*, 10(4):471–487.
- Bischoff, K. B. and Levenspiel, O. (1962). Fluid dispersion—generalization and com-

- parison of mathematical models—II comparison of models. *Chemical Engineering Science*, 17(4):257–264.
- BLOCON (2017). Earth Energy Designer (EED) Version 4 Update Manual. Online. Retrieved February 13, 2019 from <https://buildingphysics.com/eed-2/>.
- Brussieux, Y. and Bernier, M. (2018). A hybrid model for generating short-time g-functions. In *IGSHPA Research Conference Proceedings*, pages 48–57, Stockholm, Sweden. IGSHPA. September 18–19.
- Carslaw, H. S. and Jaeger, J. C. (1959). *Conduction of Heat in Solids*. Clarendon Press, Oxford, 2nd edition.
- Cazorla-Marín, A., Montagud, C., Corberán, J. M., Tinti, F., and Focaccia, S. (2018). Upgrade of the B2G dynamic geothermal heat exchanger model: optimal location of the ground nodes. In *IGSHPA Research Conference Proceedings*, pages 20–28, Stockholm, Sweden. IGSHPA. September 18–19.
- Cazorla-Marín, A., Montagud, C., Montero, Á., Martos, J., and Corberán, J. M. (2017). Influence of different ground thermal properties in a borehole heat exchanger’s performance using the B2G dynamic model. In *IGSHPA Research Conference Proceedings*, pages 192–200, Denver, CO. IGSHPA. March 14–16.
- Cimmino, M. (2018a). Fast calculation of the g-functions of geothermal borehole fields using similarities in the evaluation of the finite line source solution. *Journal of Building Performance Simulation*, 11(6):655–668.
- Cimmino, M. (2018b). g-Functions for bore fields with mixed parallel and series connections considering axial fluid temperature variations. In *IGSHPA Research Conference Proceedings*, pages 262–271, Stockholm, Sweden. IGSHPA. September 18–19.

- Cimmino, M. (2018c). pygfunction: an open-source toolbox for the evaluation of thermal response factors for geothermal borehole fields. In *Proceedings of eSim 2018, the 10th conference of IBPSA-Canada*, pages 492–501, Montréal, QC, Canada. International Building Performance Simulation Association. 10.5281/zenodo.1195040.
- Cimmino, M. and Bernier, M. (2014). A semi-analytical method to generate g-functions for geothermal bore fields. *International Journal of Heat and Mass Transfer*, 70:641–650.
- Claesson, J. (2011). Multipole method to calculate borehole thermal resistances: mathematical report. Technical Report 2012-06-20, Chalmers Technical University, Gothenburg, Sweden.
- Claesson, J. (2013). Performance evaluation of combined heat sources for innovative heat pumps – ground source combined with an air coil. In *CLIMA 2013*, Prague, Czech Republic. RHEVA. June 16–19.
- Claesson, J. and Dunand, A. (1983). Heat extraction from the ground by horizontal pipes – a mathematical analysis. Technical report, Swedish Council for Building Research, Stockholm, Sweden.
- Claesson, J. and Eskilson, P. (1985). Thermal analysis of heat extraction boreholes. In *3rd International Conference on Energy Storage for Building Heating and Cooling—Enerstock 85*, pages 222–227, Toronto, Canada. Public Works and Government Services Canada.
- Claesson, J. and Eskilson, P. (1988). Conductive heat extraction to a deep borehole – thermal analysis and dimensioning rules. *Energy*, 13:509–527.
- Claesson, J. and Hellström, G. (2011). Multipole method to calculate borehole thermal resistances in a borehole heat exchanger. *HVAC&R Research*, 17(6):895–911.

- Claesson, J. and Javed, S. (2011). An analytical method to compute borehole fluid temperatures for timescales from minutes to decades. *ASHRAE Transactions*, 117(2):279–288.
- Claesson, J. and Javed, S. (2012). A load-aggregation method to calculate extraction temperatures of borehole heat exchangers. In *ASHRAE Winter Conference*, Chicago, IL. January 21–25.
- Crawley, D. B., Lawrie, L. K., Winkelmann, F. C., Buhl, W. F., Huang, Y. J., Pedersen, C. O., Strand, R. K., Liesen, R. J., Fisher, D. E., Witte, M. J., and Glazer, J. (2001). EnergyPlus: creating a new-generation building energy simulation program. *Energy and Buildings*, 33(4):319–331.
- De Carli, M., Tonon, M., Zarrella, A., and Zecchin, R. (2010). A computational capacity resistance model (CaRM) for vertical ground-coupled heat exchangers. *Renewable Energy*, 35(7):1537–1550. Special Section: IST National Conference 2009.
- Deb, K., Pratap, A., Agarwal, S., and Meyarivan, T. (2002). A fast and elitist multiobjective genetic algorithm: NSGA-II. *IEEE Transactions on Evolutionary Computation*, 6(2):182–197.
- Deru, M., Field, K., Studer, D., Benne, K., Griffith, B., Torcellini, P., Liu, B., Halverson, M., Winiarski, D., Rosenberg, M., Yazdanian, M., Huang, J., and Crawley, D. (2011). U.S. Department of Energy commercial reference building models of the national building stock. Technical Report TP-5500-46861, National Renewable Energy Laboratory, Golden, CO.
- Diao, N. R., Li, Q. Y., and Fang, Z. (2004). Heat transfer in ground heat exchangers with ground water advection. *International Journal of Thermal Sciences*, 43:1203–1211.

- DOE (2018). Weather Data. <https://energyplus.net/weather>.
- Doyle, J. F. (1988). Spectral analysis of coupled thermoelastic waves. *Journal of Thermal Stress*, 11:175–185.
- Doyle, J. F. (1997). *Wave Propagation in Structures: Spectral Analysis Using Fast Discrete Fourier Transforms*. Springer-Verlag, New York, NY.
- Duhamel, M. J.-M.-C. (1828). Sur les equations générales de la propagation de la chaleur dan les corps solides dont la conductibilité n’est pas la même dan tous les sens. *Journal de l’Ecole Polytechnique*, 21:356–399.
- Dusseault, B. and Pasquier, P. (2018). Near-instant g-function construction with artificial neural networks. In *IGSHPA Research Conference Proceedings*, pages 450–458, Stockholm, Sweden. IGSHPA. September 18–19.
- Dusseault, B., Pasquier, P., and Marcotte, D. (2018). A block matrix formulation for efficient g-function construction. *Renewable Energy*, 121:249–260.
- EnergyPlus (2017). *EnergyPlusTM version 8.8.0 documentation: engineering reference*. U.S. Department of Energy.
- Eskilson, P. (1987). *Thermal analysis of heat extraction boreholes*. PhD thesis, University of Lund, Lund, Sweden.
- Eskilson, P. and Claesson, J. (1988). Simulation model for thermally interacting heat extraction boreholes. *Numerical Heat Transfer*, 13:149–165.
- Fascì, M. L., Lazzarotto, A., Acuña, J., and Claesson, J. (2018). Thermal influence of neighboring GSHP installations: relevance of heat load temporal resolution. In *IGSHPA Research Conference Proceedings*, pages 440–448, Stockholm, Sweden. IGSHPA. September 18–20.

- Fisher, D. E., Rees, S. J., Padhmanabhan, S. K., and Murugappan, A. (2006). Implementation and validation of ground-source heat pump system models in an integrated building and system simulation environment. *HVAC&R Research*, 12(3a):693–710.
- Fossa, M. and Minchio, F. (2013). The effect of borefield geometry and ground thermal load profile on hourly thermal response of geothermal heat pump systems. *Energy*, 51:323–329.
- Gautschi, W. and Cahill, W. F. (1964). *Handbook of Mathematical Functions with Formulas, Graphs, and Mathematical Tables*, chapter Exponential integral and related functions, page 229. National Bureau of Standards, Washington, DC.
- Gehlin, S. and Spitler, J. D. (2014a). A thermo-economic analysis of a residential ground-source heat pump system: one deeper vs. two shallower boreholes. In *Proceedings of IEA Heat Pump Conference*, Montréal, QC, Canada. May 12–16.
- Gehlin, S. E. A. and Spitler, J. D. (2014b). Design of residential ground source heat pump systems for heating dominated climates – trade-offs between ground heat exchanger design and supplementary electric resistance heating. In *ASHRAE Winter Conference*, New York, NY. January 18–22.
- Gehlin, S. E. A. and Spitler, J. D. (2015). Effects of ground heat exchanger design flow velocities on system performance of ground source heat pump systems in cold climates. In *ASHRAE Winter Conference*, Chicago, IL. January 23–27.
- Gehlin, S. E. A., Spitler, J. D., and Hellström, G. (2016). Deep boreholes for ground source heat pump systems—Scandinavian experience and future prospects. In *ASHRAE Winter Conference*, Chicago, IL. January 23–27.
- Gnielinski, V. (1976). New equations for heat and mass transfer in turbulent pipe and channel flow. *International Chemical Engineering*, 16(2):359–368.

- Go, G. H., Lee, S. R., Yoon, S., Park, H., and Park, S. (2014). Estimation and experimental validation of borehole thermal resistance. *KSCE Journal of Civil Engineering*, 18(4):992–1000.
- Godefroy, V., Lecomte, C., Bernier, M., Douglas, M., and Armstrong, M. (2016). Experimental validation of a thermal resistance and capacity model for geothermal boreholes. In *ASHRAE Winter Conference*, Orlando. January 23–27.
- Google (2018). Google Books Ngrams Viewer. <http://books.google.com/ngrams>.
- Grundmann, R. M. (2016). Improved design methods for ground heat exchangers. Master’s thesis, Oklahoma State University, Stillwater, OK.
- Gustafsson, A.-M. and Gehlin, S. (2008). Influence of natural convection in water-filled boreholes for GCHP. *ASHRAE Transactions*, 114(1):416–423.
- Hammock, C. W. and Sullens, S. (2017). Coupling geothermal heat pumps with underground seasonal thermal energy storage. Technical Report EW-201135, Environmental Security Technology Certification Program, Alexandria, VA.
- He, M. (2012). *Numerical modeling of geothermal borehole heat exchanger systems*. PhD thesis, De Montfort University, Leicester, UK.
- He, M., Rees, S., and Shao, L. (2011). Simulation of a domestic ground source heat pump system using a three-dimensional numerical borehole heat exchanger model. *Journal of Building Performance Simulation*, 4(2):141–155.
- Hellström, G. (1991). *Ground heat storage: thermal analysis of duct storage systems*. PhD thesis, University of Lund, Lund, Sweden.
- Holmberg, H. (2016). *Transient heat transfer in boreholes with application to non-grouted borehole heat exchangers and closed loop engineered geothermal systems*. PhD thesis, Norwegian University of Science and Technology, Trondheim, Norway.

- Holmberg, H., Acuña, J., Næss, E., and Sønju, O. K. (2016). Numerical model for non-grouted borehole heat exchangers, Part 2—Evaluation. *Geothermics*, 59:134–144.
- Honderich, T. (2005). *The oxford companion to philosophy*. Oxford University Press, Oxford, UK, 2nd edition.
- Ingersoll, L. R. and Plass, H. J. (1948). Theory of ground pipe heat source for the heat pump. *Piping and Air Conditioning*, 20:119–122.
- Ingersoll, L. R., Plass, H. J., and Ingersoll, H. (1951). Theory of earth heat exchangers for the heat pump. *ASHVE Transactions*, 57:167–188.
- Ingersoll, L. R., Zobel, O. J., and Ingersoll, A. C. (1954). *Heat Conduction: with Engineering and Geological Applications*. McGraw-Hill, 2nd edition.
- Javed, S. and Claesson, J. (2011). New analytical and numerical solutions for the short-term analysis of vertical ground heat exchangers. *ASHRAE Transactions*, 117(1):3–12.
- Javed, S. and Spitler, J. D. (2016). *Advances in Ground-Source Heat Pump Systems*, chapter Calculation of Borehole Thermal Resistance, pages 63–95. Woodhead Publishing, Duxford, UK.
- Javed, S. and Spitler, J. D. (2017). Accuracy of borehole thermal resistance calculation methods for grouted single u-tube ground heat exchangers. *Applied Energy*, 187:790–806.
- Juhlin, K. and Gehlin, S. E. A. (2017). Vertical GSHP systems in Sweden 1978–2015: a survey based on the Swedish well database. In *IGSHPA Research Conference Proceedings*, pages 18–25, Denver, CO. IGSHPA. March 14–16.

- Kerme, E. D. and Fung, A. S. (2019). Heat transfer simulation, analysis and performance study of single U-tube borehole heat exchanger. *Renewable Energy*, In press.
- Klein, S. A., Beckman, W. A., Mitchell, J. W., Duffie, J. A., Duffie, N. A., Freeman, T., Mitchell, J. C., Braun, J. E., Evans, B. L., Kummer, J. P., Urban, R. E., Fiksel, A., Thornton, J. W., Blair, N. J., Williams, P. M., Bradley, D. E., McDowell, T. P., Kummert, M., Arias, D. A., and Duffy, M. J. (2016). *TRNSYS manual: a transient simulation program*. Solar Engineering Laboratory. University of Wisconsin-Madison, Madison, WI.
- Kruis, N. and Krarti, M. (2015). KivaTM: a numerical framework for improving foundation heat transfer calculations. *Journal of Building Performance Simulation*, 8(6):449–468.
- Lamarche, L. (2009). A fast algorithm for the hourly simulations of ground-source heat pumps using arbitrary response factors. *Renewable Energy*, 34(10):2252–2258.
- Lamarche, L. and Beauchamp, B. (2007). A new contribution to the finite line-source model for geothermal boreholes. *Energy and Buildings*, 39(2):188–198.
- Lamarche, L., Kaji, K., and Beauchamp, B. (2010). A review of methods to evaluate borehole thermal resistances in geothermal heat exchangers. *Geothermics*, 39(2):187–200.
- Lax, P. and Wendroff, B. (1960). Systems of conservation laws. *Communications on Pure and Applied Mathematics*, 13(2):217–237.
- Lee, E. S. (2013). *An improved hydronic loop system solution algorithm with a zone-coupled horizontal ground heat exchanger model for whole building energy simulation*. PhD thesis, Oklahoma State University, Stillwater, OK.

- Li, M. and Lai, L. C. K. (2012). Heat-source solutions to heat conduction in anisotropic media with applications to pile and borehole ground heat exchangers. *Applied Energy*, 96:451–458.
- Li, M., Zhu, K., and Fang, Z. (2016). *Advances in Ground-Source Heat Pump Systems*, chapter Analytical methods for thermal analysis of vertical ground heat exchangers, pages 157–185. Woodhead Publishing, Duxford, UK.
- Liao, Q., Zhou, C., Cui, W., and Jen, T. C. (2012). New correlations for thermal resistances of vertical single u-tube ground heat exchanger. *Journal of Thermal Science and Engineering Applications*, 4(3):031010–031010–7.
- Liu, X. (2005). *Development and experimental validation of simulation of hydronic snow melting systems for bridges*. PhD thesis, Oklahoma State University, Stillwater, OK.
- Loveridge, F. (2012). *The thermal performance of foundation piles used as heat exchangers in ground energy systems*. PhD thesis, University of Southampton, Southampton, UK.
- Loveridge, F. and Powrie, W. (2013). Temperature response functions (G-functions) for single pile heat exchangers. *Energy*, 57:554–564.
- Malayappan, V. and Spitler, J. D. (2013). Limitation of using uniform heat flux assumptions in sizing vertical borehole heat exchanger fields. In *Proceedings of CLIMA 2013*, Prague, Czech Republic. June 16–19.
- Man, Y., Yang, H., Diao, N. R., Liu, J., and Fang, Z. H. (2010). A new model and analytical solutions for borehole and pile ground heat exchangers. *International Journal of Heat and Mass Transfer*, 53:2593–2601.

- Marcotte, D. and Pasquier, P. (2008). Fast fluid and ground temperature computation for geothermal ground-loop heat exchanger systems. *Geothermics*, 37(6):651–665.
- Marcotte, D. and Pasquier, P. (2009). The effect of borehole inclination on fluid and ground temperature for GLHE systems. *Geothermics*, 38(4):392–398.
- Marcotte, D. and Pasquier, P. (2014). Unit-response function for ground heat exchanger with parallel, series or mixed borehole arrangement. *Renewable Energy*, 68:14–24.
- Mazur, P. (1997). Onsanger’s reciprocal relations and thermodynamics of irreversible processes. *Periodica Polytechnica Ser. Chem. Eng.*, 41(2):197–207.
- Mitchell, M. (2019). Load profiles. <https://doi.org/10.6084/m9.figshare.8984243.v1>.
- Mitchell, M. S. and Spitler, J. D. (2013). Open-loop direct surface water cooling and surface water heat pump systems—A review. *HVAC&R Research*, 19(2):125–140.
- Mogensen, P. (1983). Fluid to duct wall heat transfer in dust system heat storages. In *International Conference on Subsurface Heat Storage in Theory and Practice*, Stockholm, Sweden. Swedish Council for Building Research.
- Moin, P. (2010). *Fundamentals of engineering numerical analysis*. Cambridge University Press, New York, NY.
- Monzó, P., Acuña, J., Fossa, M., and Palm, B. (2013). Numerical generation of the temperature response factors for a borehole heat exchanger field. In *Proceedings of European Geothermal Congress*, pages 1–8, Pisa, Italy. June 3–7.
- Murugappan, A. (2002). Implementing ground source heat pump and ground loop heat exchanger models in the EnergyPlus simulation environment. Master’s thesis, Oklahoma State University, Stillwater, OK.

- Nabi, M. and Al-Khoury, R. (2012a). An efficient finite volume model for shallow geothermal systems—Part I: model formulation. *Computers & Geosciences*, 49:290–296.
- Nabi, M. and Al-Khoury, R. (2012b). An efficient finite volume model for shallow geothermal systems—Part II: verification, validation and grid convergence. *Computers & Geosciences*, 49:297–307.
- Nordman, R. (2014). Research Institutes of Sweden. Email to S. Gehlin. September 1, 2014.
- Nordman, R., Kleefkens, O., Riviere, P., Nowak, T., Zottl, A., Arzano-Daurelle, C., Lehmann, A., Polyzou, O., Karytsas, K., Riederer, P., Miara, M., Lindahl, M., Andersson, K., and Olsson, M. (2012). Seasonal performance factor and monitoring for heat pump systems in the building sector. SEPEMO-Build final report. Report IEE/08/776/SI2.529222, Intelligent Energy Europe.
- Onsager, L. (1931a). Reciprocal relations in irreversible processes. I. *Physical Review*, 37:405–426.
- Onsager, L. (1931b). Reciprocal relations in irreversible processes. II. *Physical Review*, 38:2265–2279.
- Özişik, M. N. (2002). *Boundary Value Problems of Heat Conduction*. Dover Publications, New York, NY.
- Pasquier, P. and Marcotte, D. (2012). Short-term simulation of ground heat exchanger with an improved TRCM. *Renewable Energy*, 46:92–99.
- Pasquier, P. and Marcotte, D. (2014). Joint use of quasi-3D response model and spectral method to simulate borehole heat exchanger. *Geothermics*, 51:281–299.

- Pasquier, P., Zarrella, A., and Labib, R. (2018). Application of artificial neural networks to near-instant construction of short-term g-functions. *Applied Thermal Engineering*, 143:910–921.
- Patankar, S. V. (1991). *Computation of conduction and duct flow heat transfer*. Innovative Research, Inc., Maple Grove, MN.
- Petukhov, B. S. (1970). *Advances in Heat Transfer*, volume 6, chapter Heat transfer and friction in turbulent pipe flow with variable physical properties, pages 503–564. Academic Press, Inc., New York, NY.
- Rees, S. J. (2015). An extended two-dimensional borehole heat exchanger model for simulation of short and medium timescale thermal response. *Renewable Energy*, 83:518–526.
- Rees, S. J., Spitler, J. D., Deng, Z., Orio, C. D., and Johnson, C. N. (2004). A study of geothermal heat pump and standing column well performance. *ASHRAE Transactions*, 109(1):3–13.
- Ruiz-Calvo, F., De Rosa, M., Acuña, J., Corberán, J. M., and Montagud, C. (2015). Experimental validation of a short-term borehole-to-ground (B2G) dynamic model. *Applied Energy*, 140:210–223.
- Ruiz-Calvo, F., De Rosa, M., Monzó, P., Montagud, C., and Corberán, J. M. (2016). Coupling short-term (B2G model) and long-term (g-function) models for ground source heat exchanger simulation in TRNSYS. Application in a real installation. *Applied Thermal Engineering*, 102:720–732.
- Shao, H., Hein, P., Sachse, A., and Kolditz, O. (2016). *Geoenergy Modeling II: Shallow Geothermal Systems*. Springer, Cham, Switzerland.

- Skoglund, T. and Dejmek, P. (2007). A dynamic object-oriented model for efficient simulation of fluid dispersion in turbulent flow with varying fluid properties. *Chemical Engineering Science*, 62(8):2168–2178.
- Spitler, J. D. (2000). GLHEPro – a design tool for commercial building ground loop heat exchangers. In *4th International Heat Pump in Cold Climates Conference*, Aylmer, Québec. August 17–18.
- Spitler, J. D. and Bernier, M. A. (2016). *Advances in Ground-Source Heat Pump Systems*, chapter Vertical borehole ground heat exchanger design methods, pages 29–61. Woodhead Publishing, Duxford, UK.
- Spitler, J. D. and Gehlin, S. (2019). Measured performance of a mixed-use commercial-building ground source heat pump system in Sweden. *Energies*, 12(10):34.
- Spitler, J. D. and Gehlin, S. E. A. (2015). Thermal response testing for ground source heat pump systems—An historical review. *Renewable and Sustainable Energy Reviews*, 50:1125–1137.
- Spitler, J. D., Javed, S., and Ramstad, R. K. (2016). Natural convection in groundwater-filled boreholes used as ground heat exchangers. *Applied Energy*, 164:352–365.
- Spitler, J. D., Southard, L. E., and Liu, X. (2017). Ground-source and air-source heat pump system performance at the ASHRAE headquarters building. In *Proceedings of the 12th IEA Heat Pump Conference*, Rotterdam, Netherlands. International Energy Agency. May 11–14.
- Spitler, J. D., Wong, M. D., and Gehlin, S. E. A. (2014). Effect of residential ground source heat pump system design on CO₂ emissions in Sweden. In *Proceedings of ASHRAE Annual Conference*, Seattle, WA. June 28–July 2.

- Thomson, W. (1884). Compendium of the Fourier Mathematics for the Conduction of Heat in Solids, and the Mathematically Allied Physical Subjects of Diffusion of Fluids, and Transmission of Electrical Signals Through Submarine Cables. In *Article 72. Mathematical and Physical Papers*, pages 41–60. University Press, Cambridge, UK.
- Wentzel, E.-L. (2005). *Thermal modeling of walls foundations and whole buildings using dynamic thermal networks*. PhD thesis, Chalmers University of Technology, Gothenburg, Sweden.
- Witte, H. J. L. (2018). A novel tool for assessing negative temperature interactions between neighboring borehole heat exchanger systems. In *14th International Conference on Energy Storage-EnerSTOCK2018*, pages 1–14, Adana, Turkey. April 25–28.
- Woodruff, M. J. and Herman, J. (2018). Pareto. <https://github.com/matthewjwoodruff/pareto.py>.
- Xu, X. (2007). *Simulation and optimal control of hybrid ground source heat pump systems*. PhD thesis, Oklahoma State University, Stillwater, OK.
- Xu, X. and Spitler, J. D. (2006). Modeling of vertical ground loop heat exchangers with variable convective resistance and thermal mass of the fluid. In *Proceedings of the 10th International Conference on Thermal Energy Storage-EcoStock 2006*, Pomona, NJ, USA. May 31–June 2.
- Yavuzturk, C. and Spitler, J. D. (1999). A short time step response factor model for vertical ground loop heat exchangers. *ASHRAE Transactions*, 105(2):475–485.
- Yu, M., Rang, H., Zhao, J., Zhang, K., and Fang, Z. (2017). Influence of ground heat exchanger zoning operation on the GSHP system long-term operation perfor-

mance. In *IGSHPA Research Conference Proceedings*, pages 144–151, Denver, CO. IGSHPA. March 14–16.

Zarrella, A., Scarpa, M., and De Carli, M. (2011). Short time step analysis of vertical ground-coupled heat exchangers: the approach of CaRM. *Renewable Energy*, 36(9):2357–2367.

Zeng, H. Y., Diao, N. R., and Fang, Z. H. (2002). A finite line-source model for boreholes in geothermal heat exchangers. *Heat Transfer - Asian Research*, 31(7):558–567.

APPENDIX A

HISTORICAL RESPONSE FACTOR MODEL

1.1 Derivation

Historically, the method which has been used to apply g-function models to WBES environments has been to reformulate Equation 3.1 to be a function of the inlet temperature and the circulating fluid mass flow rate. One way to do this is by deconvolving the current heat load, q_n , then substituting in relationships to relate the borehole wall heat transfer rate, q_b , to the fluid heat transfer rate, q_f . And by relating the mean fluid temperature, T_f , to the inlet and outlet temperatures, T_{in} and T_{out} , respectively. The following derivation was given by Liu (2005), but is recast here for clarity and extended to incorporate better estimates of the mean fluid temperature.

Beginning with Equation 3.1, we will simplify the notation so the equations can be written more easily. First we will let Equations 1.1 and 1.2 apply, which assumes that the g-function values are being computed for the appropriate GHE configuration. For clarity, the subscript, n , indicates the current time step, and by extension, $n - 1$ indicates the previous time step. As a result, Equation 3.1 is recast as shown in Equation 1.4.

$$g_i = g\left(\frac{t_n - t_{i-1}}{t_s}, r_b/H, B/H, D/H\right) \quad (1.1)$$

$$g_n = g\left(\frac{t_n - t_{n-1}}{t_s}, r_b/H, B/H, D/H\right) \quad (1.2)$$

$$c_0 = \frac{1}{2\pi k_s} \quad (1.3)$$

$$T_b = T_s + c_0 \sum_{i=1}^n (q_i - q_{i-1}) \cdot g_i \quad (1.4)$$

In this equation, the current heat transfer rate and borehole wall temperatures are unknown values. Our goal is to compute the heat transfer rate from the circulating fluid and the exiting fluid temperature given GHE inlet fluid temperature and flow rate. Since the borehole wall temperature is not needed directly, it can be related to the mean fluid temperature and eliminated. This can be done through Equation 1.5 by assuming steady conduction through the borehole, which implies that $q_b = q_f$.

$$T_f = T_b + q_n R_b \quad (1.5)$$

Substituting Equation 1.5 into 1.4 yields the following equation.

$$T_f = T_s + c_0 \sum_{i=1}^n (q_i - q_{i-1}) \cdot g_i + q_n R_b \quad (1.6)$$

For steady-state, constant flux situations the simple mean of the GHE inlet and outlet temperatures is valid and given in Equation 1.7.

$$T_f = \frac{T_{out} + T_{in}}{2} \quad (1.7)$$

Equation 1.7 could be substituted into Equation 1.6, but we would still have added an unknown, T_{out} , since this is not known beforehand; rather it is a quantity we wish to solve for. The steady-state energy equation can now be introduced to help achieve the final solution.

$$q_n = \frac{\dot{m}c_p (T_{in} - T_{out})}{H} \quad (1.8)$$

Solving both Equations 1.7 and 1.8 for T_{out} and substituting together then solving for T_f , we can generate another relationship for the mean fluid temperature inside of the borehole.

$$T_f = T_{in} - \frac{1}{2} \frac{q_n H}{\dot{m}c_p} \quad (1.9)$$

Now, taking Equation 1.6 and deconvolving q_n yields the following:

$$T_f = T_s + c_0 \left((q_n - q_{n-1}) \cdot g_n + \sum_{i=1}^{n-1} (q_i - q_{i-1}) \cdot g_i \right) + q_n R_b \quad (1.10)$$

Again for simplification, let the following apply, so that Equation 1.10, becomes Equation 1.12, after the history terms have been combined, as shown in Equation 1.11.

$$c_1 = \sum_{i=1}^{n-1} (q_i - q_{i-1}) \cdot g_i \quad (1.11)$$

$$T_f = T_s + c_0 ((q_n - q_{n-1}) \cdot g_n + c_1) + q_n R_b \quad (1.12)$$

Finally, we combine Equations 1.9 and 1.12 and solve for q_n , which gives the final equation 1.13 that relates GHE inlet temperature and mass flow rate to GHE heat transfer rate. Other terms are history terms, or parameters related to the GHE geometry.

$$q_n = \frac{T_{in} - T_s + \frac{q_{n-1}g_n}{c_0} - \frac{c_1}{c_0}}{\frac{1}{2} \frac{H}{\dot{m}c_p} + \frac{g_n}{c_0} + R_b} \quad (1.13)$$

The final solution is achieved by solving Equation 1.13 for the current heat transfer

rate, q_n . This is then used to solve for the mean fluid temperature using Equation 1.6, which is then used with Equation 1.14 to solve for the GHE exiting fluid temperature, T_{out} .

$$T_{out} = T_f - \frac{1}{2} \frac{q_n H}{\dot{m} c_p} \quad (1.14)$$

1.2 Extension of Historical Model for Improved Mean Fluid Temperature

One of the problems with the above model is that it uses a steady-state, simple mean of the GHE fluid temperature, which is an approximation. Thermal short-circuiting within the borehole will cause energy to be transferred between the U-tube pipes within the borehole. As a result, the mean fluid temperature along the length of the borehole is often not equal to the simple mean of the inlet and outlet temperatures. The problem is worsened for systems with deep boreholes, or for systems with low flow rates. One potential way to correct this is by incorporating the model developed by Beier and Spitler (2016). This model weights the fluid temperature based on correlations related to the fluid transit time and the time required for steady-flux heat transfer to occur. The transit time is defined as the time required for the fluid to pass from the GHE inlet to outlet, The model is given in Equation 1.15.

$$T_f = f T_{in} + (1 - f) T_{out} \quad (1.15)$$

Specific details regarding calculation of the fluid temperature correction factor can be found in Beier and Spitler (2016) and Beier et al. (2018). As was done before, solving Equation 1.15 for T_{out} and substituting back into Equation 1.8, we can determine a new relationship for computing the mean fluid temperature. This is given in Equation 1.16.

$$T_f = T_{in} - (1 - f) \frac{q_n H}{\dot{m} c_p} \quad (1.16)$$

In the steady-state condition, f approaches 0.5. As a result, the relation given with the updated equation yields the same results as the simple mean fluid temperature approximation under steady-state conditions.

$$q_n = \frac{T_{in} - T_s + \frac{q_n - 1 g_n}{c_0} - \frac{c_1}{c_0}}{(1 - f) \frac{H}{\dot{m} c_p} + \frac{g_n}{c_0} + R_b} \quad (1.17)$$

The final solution is then given by applying Equation 1.17 to solve for the heat transfer rate. Equation 1.6 is again used to compute the mean fluid temperature. Finally, the exiting fluid temperature can be computed with Equation 1.18.

$$T_{out} = T_f - f \frac{q_n H}{\dot{m} \cdot c_p} \quad (1.18)$$

VITA

Matt Sandy Mitchell

Candidate for the Degree of

Doctor of Philosophy

Dissertation: AN ENHANCED VERTICAL GROUND HEAT EXCHANGER
MODEL FOR WHOLE BUILDING ENERGY SIMULATION

Major Field: Mechanical Engineering

Biographical:

Education:

Completed the requirements for the Doctor of Philosophy in Mechanical Engineering at Oklahoma State University, Stillwater, Oklahoma in July, 2019.

Completed the requirements for the Master of Science in Mechanical Engineering at Oklahoma State University, Stillwater, Oklahoma in 2014.

Completed the requirements for the Bachelor of Science in Mechanical Engineering at Brigham Young University—Idaho, Rexburg, Idaho in 2010.

Experience:

Intern at Forsgren Associates in Rexburg, Idaho during the summers of 2008 and 2009. Designer at Applied Engineering Services in Idaho Falls, Idaho from Sept. 2010–Apr. 2011. Research Assistant at Oklahoma State University from Jun. 2011–Jun. 2013, and as a Lecturer from Jan. 2016–May 2019, and as a Research Engineer from Jun. 2013–August 2019.

Professional Affiliations:

American Society of Heating, Refrigerating, and Air-conditioning Engineers.